Influence of Discrete Double Inclined Ribs on Performance of Ground Heat Exchanger for Ground Source Heat Pump

September 2020

Department of Science and Advanced Technology
Graduate School of Science and Engineering
Saga University

Teguh Hady Ariwibowo

Influence of Discrete Double Inclined Ribs on Performance of Ground Heat Exchanger for Ground Source Heat Pump

By

Teguh Hady Ariwibowo

A dissertation submitted in partial fulfillment of the
requirements for the degree of

Doctor of Engineering (Dr.Eng.)
in
Mechanical Engineering

Department of Science and Advanced Technology
Graduate School of Science and Engineering
Saga University
Japan

September 2020

Acknowledgment

At first, I would like to express my praise and gratitude to Allah, the Almighty, who makes me capable of successfully completing this study.

With great pleasure, I am profoundly indebted to my supervisors Professor Akio MIYARA and Associate Professor Keishi KARIYA of Saga University, Japan, for their expert guidance, extraordinary kindness, inspiration, and all kinds of supports throughout my present study. Their sufficient cooperation made me confidential enough in each step of my research work.

Sincere thanks to my entire Thermal Energy Engineering Laboratory members who have extended their kind help to me during my study. Special thanks to group mates in Ground Source Heat Pump Research Group: Md. Hasan Ali, Ryo Shibata, Tran Xuan Duc, Gouichi Kuriyama, Ryoma Tabata, Yasunari Takatsuka, and Kei Kano for the stimulating discussions, and we were working together.

My sincere thanks also go to the Japanese Ministry of Education, Culture, Sports, Science, and Technology for granting three years 'Monbukagakusho Scholarship'.

I thank my colleagues in Power Plant Engineering Study Program at Politeknik Elektronika Negeri Surabaya (PENS) for their kindness and support during my study. I am grateful to Dr. Zainal Arief as Director of PENS for allowing me to study in Japan. Also, I would like to thank the English Language Ability Improvement program (PKBI) DIKTI, especially D Class members, for encouraging me on my study journey. I hope all of you can reach your dreams.

I would like to thank Professor Shigeru MATSUO and Professor Yuichi MITSUTAKE as thesis examination committee for using their valuable time to judge my thesis and helpful suggestions.

My family, especially my beloved wife, who has always encouraged me; my lovely son whose unconditional love to me.

Finally, I am very grateful to my parents for their patience, moral support, and endless love in the long journey of my life. May God bless and appreciate them all.

ABSTRACT

Ground source heat pumps (GSHP) are widely utilized in various commercial and residential buildings as heating and air-conditioning. The GSHP is an attractive option besides using conventional air source heat pumps (ASHP). The GSHP system has a higher efficiency than that of the ASHP. Furthermore, GSHP is environmentally friendly. In the GSHP system, the geothermal energy of the ground is transferred to the GSHP using a closed-loop system connected to the Ground Heat Exchanger (GHE), which is buried in a horizontal orientation in the trench or vertical orientation in the borehole. Although the GSHP system can save energy, the large installation costs hinder the spread of utilizing this technology. High installation costs can be reduced by designing the right GHE in terms of material and the right size.

This research focuses on horizontal slinky-coil GHE. Slinky-coil is a GHE that has a low curvature coil. Thus, centrifugal force produces weak thermal mixing, especially at low flowrate. Meanwhile, discrete double inclined ribs is an alternative way to increase heat exchanger performance by generating longitudinal vortex, which is effective in increasing thermal mixing in a straight tube. The slinky coil has heat transfer and fluid flow characters similar to straight tubes. Therefore, this study aims to improve the performance of the slinky coil by using double discrete inclined ribs on the coil wall.

In this study, the analysis of GHE slinky coil performance has been studied through numerical simulation studies. The slinky coil performance analysis is performed on two conditions, first the ideal conditions and steady-state. The first method only analyzes the phenomenon of flow inside the coil in various modifications of ribs geometry. In this condition, the heat exchanger is assumed to have a constant temperature wall, and there is no heat loss from the heat exchanger. All performance in this condition is calculated based on the axial length of the coil. In the second condition, the slinky coil GHE is simulated with a real-scale condition by adding land and transient domains. Thus, this condition simulation can represent real conditions. The performance

in this condition is calculated in trench length; meanwhile, some local parameters analysis is conducted on several locations at axial length. Detailed simulation settings and validation refer to previous research conducted at Saga University, Japan. All numerical simulations use commercial computational fluid dynamics software ANSYS Fluent 17.2.

The performance of heat transfer and water flow from ribs coil is done in turbulent flow with variations in ribs height. In general, the fluid has reached fully developed when in the 90^{o} cross-section for ribs coil and plain coil. Plain coil has a wall heat flux with a sinusoidally distributed value of low heat flux at 10^{o} and high heat flux at 180^{o}. The influence of the centrifugal force is very dominant on this coil. Meanwhile, on the ribs coil, the heat flux distribution is randomly distributed. At 1 mm ribs height, the lowest heat flux values occur at an angle of 280^{o} and highest at 350^{o}. The flow generated by ribs is strong enough to affect secondary flow due to curvature. In ribs coil, strong thermal mixing produces temperatures on the downstream side hotter than plain coil. This phenomenon indicates that to reach the same temperature at the axial length of the ribs coil is shorter than the plain coil ribs coil. Secondary flow in the ribs coil is distorted at a greater angle than the plain coil. To understand the relationship between heat transfer and pressure drop on both coils using absolute vorticity flux. Based on this method, it is revealed that the ribs height 0.45 mm tends to have a vortex strength that is almost the same as the plain coil. Thus, the 0.45 mm ribs performance is similar to plain coil.

The similar geometry is also tested at the laminar regime. The result shows that there is no significant performance improvement at 1 L/min. The heat transfer trend shows almost linear, and pressure drop shows quadratic relation to flowrate. The highest pressure drop and heat transfer in this regime are obtained about 799 Pa/m and 873 W/m, respectively, at 5 L/min. The strange COP Improvement factor behaviors are shown at 2 L/min for all of the ribs height. This phenomenon happens because calculation refers to the performance of a straight tube. For the coil, the critical Reynolds number is higher than that of a straight tube. According to Ito's critical Reynolds number, our research critical Reynolds number is 5322. In flowrate 2L/min, the Reynolds number flow is 2057, which is still laminar in the coil, but it's near to critical Reynolds number in a straight tube. In the coil, the flow is obtained secondary flow, which leads to higher performance than that of in straight tube. Furthermore, some flow is on the transition regime of a straight tube. Hence, the calculation of COP

Improvement factors for this regime needs adjustment of heat transfer and pressure drop by using a new modified Nusselt number and friction factor.

Heat transfer and fluid flow are also studied at several variations on the influence of angle of ribs, pitch ribs, and curvature coil. Generally, in the ribs coil, the heat transfer rate increases from 7.7 to 29.11% compared to the plain coil while the pressure drop increases from 12.7 to 89.5% higher than that of the plain coil. COP Improvement factors also vary between 0.25 and 5.29. In all ribs coil, multiple longitudinal vortices do not appear in the downstream coil. However, local observations on the flow around the ribs show the longitudinal vortex is visible. The shape and strength of the local vortex are similar to the shape and strength of vortex in straight ribs. This finding is supported by the streamlined flow of ribs coil, which tends to deviate several times due to the flow generated by this local vortex. Increasing the length of the particle path makes the fluid has an excellent thermal mixing between the fluid near the wall and the fluid in the core flow. The performance of ribs increases with decreasing the axial distance between ribs. The best ribs performance also occurs at the ribs angle is 20^{o} and at a curvature of 2.66 m^{-1}.

Real scale and transient simulations aim to predict the performance of ribs coil if they are fabricated and installed in the field. This simulation is done in cooing mode. In this simulation, the flow structure is also observed to see its correlation with the improved heat transfer performance. As a preliminary study, ribs were tested under laminar and turbulent conditions. In both regimes, ribs coil shows ribs coil has better thermal performance than plain coil. However, in turbulent flow, the superiority of the ribs coil only lasts until 149 minutes of initial operation. Meanwhile, in laminar flow, ribs coil excels at all operating times. This finding indicated that, in turbulent flow, the ribs coil tends to absorb more heat than turbulent flow at the beginning of operation. In this period, the ground around GHE suffers rapid cooling. An analysis of the initial 60 minutes of operation. Several parameters were observed at several coil locations. In laminar flow, the average heat transfer coefficient on plain coil and ribs coil is 892 $W/m^2.K$ and 958 $W/m^2.K$, respectively. In turbulent flow, the average heat transfer coefficient on plain coil and ribs coil is 1459 $W/m^2.K$ and 1598 $W/m^2.K$, respectively. COP Improvement factors of plain coil and DDIR-coil in laminar flow are 1.96 and 1.98, respectively. However, COP Improvement Factor on plain coil and DDIR-coil in turbulent flow are 1.89 and 1.88, respectively. In this study, a comparison of continuous and intermittent operating modes was performed. The use of intermittent mode can

increase the heat transfer rate by 17.3% higher than the continuous mode. In intermittent mode, the ground has sufficient time to do thermal recovery. This finding is supported by the oscillation of ground temperature around GHE. At this temperature oscillation, the maximum and minimum amplitudes are 1.5 C and 0.9 C, respectively. Ribs coil and plain coil are also tested using different types of pipe material, namely copper, composite, and HDPE. Generally, copper coil performance produces significant thermal performance especially in the initial 60 minutes of operation. However, this advantage is significantly reduced in the remaining operating time. It is also found no significant performance improvement between ribs coil and plain coil on the same coil material. Referring to the structure of the flow in the pipe, it is apparent that the performance of the ribs coil is superior to that of the plain coil. However, GHE performance is strongly influenced by ground thermal conductivity. So, in this study, the superiority of ribs coil is very small. This phenomenon is contrary to the simulation results in ideal and steady-state conditions. Three types of soil, namely sand, sandy clay, and clay with different thermal conductivity on DDIR-coil and plain-coil. Sandy clay, which has the highest thermal conductivity than any other soil, has the highest heat transfer rate. However, DDIR-coil performance does not indicate any notable discrepancy from plain-coil. These discoveries signify that the flow behavior in the coil does not make a substantial improvement compared to soil conductivity. Therefore, GHE performance mostly rely on the phenomenon on the ground side rather than that of waterside.

Table of Contents

List of Figures

List of Tables

Nomenclature

Parameter	Definition	Unit
A	Surface area	m^2
C_p	Specific heat	J/(kg·K)
COP	Coefficient of performance	–
f	Friction factor	–
k	Thermal conductivity	W/(m·K)
L	Length	m
$\dot{m}$	Mass flow rate	L/min
Q	Heat exchange rate	W
$\bar{Q}$	Heat exchange rate per unit length	W/m
T	Temperature	°C or K
ΔT	Temperature difference	°C or K
ΔT_{LM}	Logarithmic mean temperature difference	°C
T_i	Inlet water temperature	°C or K
T_o	Outlet water temperature	°C or K
T_g	Ground temperature	°C or K
$Q^{"}$	Surface Heat Flux	W/m^2
λ	heat transfer coefficient	$W/(m^2 \cdot °C)$
ΔP	Pressure drop	Pa
ρ	Density	kg/m^3

CHAPTER

1

INTRODUCTION

1.1 Background

The extensive use of the world's energy has caused many concerns about supply difficulties, running out of energy resources, and adverse impacts on the environment. The International Energy Agency has obtained scary data on trends in energy use. Over the past two decades, primary energy has grown by 49% and CO_2 emissions by 43% with an average annual increase of 2% and 1.8%, respectively. Figure 1.1 shows global energy consumption and its projection until 2050.

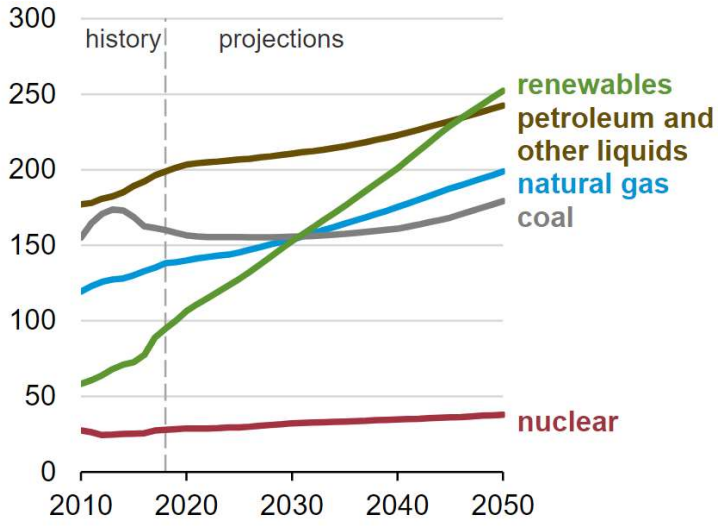

Figure 1.1 Global primary energy consumption by energy source (2010-2050) quadrillion British thermal units (US Energy Information Administration, 2019)

Electricity is at the core of the modern economy, which results in increased use of energy. Electricity demand increased as a result of increased household income, electrification of vehicles and heat, as well as growth in demand for digital electronic devices and air conditioning. The increase in electrical energy is one of the primary triggers of why global CO_2 emissions from the electricity sector reach record highs in 2018. However, the availability of technologies that produce low emissions is the frontline in the effort to minimize climate change and pollution. Decarbonized electricity can produce a framework for reducing CO_2 emissions in other sectors through synthetic fuels such as hydrogen. Renewable energy also has a significant role in providing access to the use of electricity in various regions.

Recently, Ground Source Heat Pump (GSHP) system has become an attractive option for heating and cooling buildings based on energy conservation and increasing energy prices (Self et al., 2013; Urchueguía et al., 2008; Yuan et al., 2012). The high thermal performance of the GSHP system is due to the stability of temperatures in a certain depth of the grounds throughout the year (Beier, 2014; Kavanaugh and Rafferty, 1997; Yeung, 1996). The use of low geothermal energy capable cut operating costs from 25% to 50% compared to conventional Air source Heat Pump (ASHP) (Sarbu and Sebarchievici, 2014). So, the GSHP system becomes far more efficient than conventional ASHP (Chiasson and Yavuzturk, 2009; Sanner et al., 2003; Sarbu and Sebarchievici, 2014; Urchueguía et al., 2008).

Geothermal energy does not produce pollution like fossil fuels, so this energy is safe for the environment for decades. Genchi et al. (2002) investigated the effect of the use of the GSHP system on the environment in Tokyo. They concluded that this system was able to produce 54% or 39,519 tons of CO_2 emissions reductions annually. From an economic point of view, GSHP is a promising option in large buildings because the GSHP system does not require complicated equipment and produces high efficiency (Kavanaugh and Rafferty, 1997). Based on ASHRAE, (2009), thermal energy is divided into three groups, namely high temperatures (> 150 C) typically used for electricity generation, direct use of medium and low temperatures (<150 C), and the use of GSHP (<32 C). High installation costs and weather fluctuations are a weakness of the GSHP system. However, the initial investment can reach a break-even point with energy savings from 5 to 10 years of use (Atam and Helsen, 2016). Besides, GHE design and optimization make this tool more efficient, thereby reducing the cost of energy use.

In a GSHP system, heat is extracted from or rejected to the ground via a series of buried pipes, i.e., Ground Heat Exchanger (GHE), through which a working fluid circulates. Figure 1.2 shows heat exchange between working fluid (water, anti-freeze liquid solution) and ground occurs in GHE. The heat pump delivers this exchanged heat to the building via a heat distribution subsystem. For the optimum performance of a GSHP system, proper selection and appropriate design of different components are necessary. During the winter season, the working fluid is pumped through the GHE, and it extracts heat from high temperature surrounding ground. As the heated working fluid (heat gained from the ground) enters the heat exchanger (evaporator) of the heat pump and exchanges heat between working fluid and refrigerant, which then transfers the energy indoors in order to heat the building. The working fluid, which is cooled at this point, makes its way back underground to gain heat once again from the ground, and the cycle repeats.

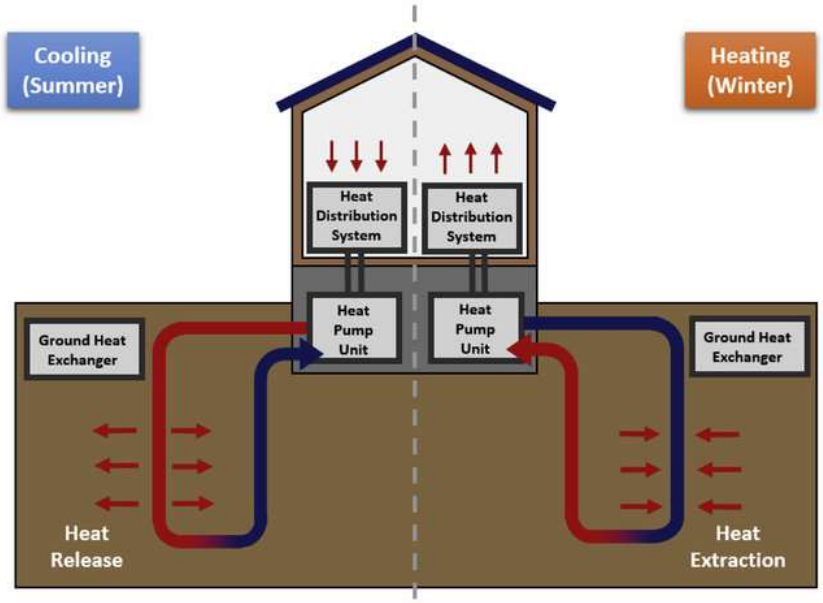

Figure 1.2 Ground source heat pump foundation for heating and cooling the room.

Two types of configurations are often used in the installation, namely horizontal trenches or vertical boreholes (Yuan et al., 2016). GHE functions as a facilitator of heat transfer between the soil and the working fluid so that GHE does not generate electricity and heat. This thermal energy is distributed to the building by connecting the GHE and Heat pump. Horizontal GHE is a common choice because it is an easy and inexpensive installation, but this GHE has lower performance than vertical GHE (Banks, 2008). In general, vertical GHE is often installed between 30 and 120 meters

(Fisher et al., 2006; Zhang et al., 2017); therefore, and installation costs are more expensive than horizontal GHE. Horizontal GHE is often installed in trenches with a depth of 1 to 2 meters above ground level (Chiasson, 2010; Florides and Kalogirou, 2007; Kavanaugh, S.P. and Rafferty, 2014), and ambient conditions strongly influence the GHE. So horizontal GHE results in transferring less amount of energy than vertical GHE. The weakness of horizontal GHE is an excellent opportunity to improve GHE performance with the option to modify a single pipe, multiple pipes, and coiled pipes. Single pipes and many pipes require a large amount of land so that the surface modification of the slinky or spiral GHE pipe so that the trench area is smaller than that of no modification GHE. Modified horizontal GHE design can reduce installation costs (Kavanaugh and Rafferty, 2014).

GHE heat transfer performance is an essential part of GSHP system planning. The three main factors for this performance are undisturbed ground temperature, thermal resistance of the ground and ground thermal conductivity (Eskilson, 1987). Observation of the GHE performance after installation is vital to understand the effect of GHE on the GSHP system. Much research on experimental approaches, analytic approaches, and numerical approaches has been carried out to improve the GSHP system. The design of Slinky-coil GHE have development in pitch coil configuration, reclined and standing configuration, and material configuration (Ali et al., 2017; Selamat et al., 2016; Wu et al., 2011; Wu, et al., 2010). There is no development in the surface of the coil since it's found. Tube Corrugations such as Discrete Double Inclined Ribs is a promising modification for heat exchanger performance improvement (Li et al., 2009; Li et al., 2007; Meng et al., 2005; Zheng et al., 2015).

1.2 Aim and Objective Present Research

First of all, to determine the effect of DDIR on slinky GHE, an ideal numerical analysis was performed on several variations of ribs height in the laminar and turbulent flow regimes. Observe several parameters such as speed and temperature and their relationship to heat transfer enhancement and pressure drop. The DDIR-coil performance is compared with plain coil performance.

Second, based on the consideration of the first study, the ideal DDIR analysis on slinky was done by various modifications of ribs such as angle ribs, pitch ribs, and curvature coil to determine the performance of heat transfer and pressure drop at low

flowrates. In this section, the structure of the flow around the ribs is examined more deeply to determine its correlation with improved performance.

Third, referring to the results of steady-state and ideal conditions, the effect of DDIR on the slinky coil is carried out with a numerical approach to transient conditions in continuous operation. Flow structure analysis is also carried out to determine parameters at several locations and their impact on global GHE performance. An intermittent operation study was conducted to determine its impact on thermal conditions on the ground and their relationship to GHE performance.

The main objectives of this study are as follows

- to investigate thermal behavior and fluid flow in DDIR Slinky GHE with variations in ribs height steady and ideal conditions.
- to observe the impact of axial ribs pitch, angle ribs and curvature coil on thermal performance and fluid flow under low flowrate conditions and investigate the flow structure and its correlation with GHE performance assuming steady and ideal conditions.
- to apply the results of steady and ideal observations to transients and real-scales of the thermal performance of slinky GHE DDIR and to conduct intermittent operation studies and their impact on GHE performance and soil thermal conditions. Influence of copper, composite, and HDPE is investigated to see their thermal behaviors on ribs coil.

1.3 Thesis structure

The results of this study are presented in several chapters. This chapter describes, in general, the background of geothermal energy, the GSHP and GHE systems. The aims and objectives of the study are also explained in this chapter. Chapter 2 sets out an overview of the GHE system based on a literature review of research developments on the GSHP and GHE systems. A description of GSHP and GHE is presented briefly. Then, a brief description of the basics of numerical computing using Computational Fluid Dynamics. Chapter 3 describes the thermohydraulic performance discrete double inclined ribs in turbulent flow at height variations. This chapter explains the effect of ribs on the distribution of the wall heat flux in the coil as well as the secondary flow distortion caused by ribs interference in the water flow. Chapter 4 illustrates the behavior of heat transfer and pressure drop on the ribs coil in laminar flow by using the same ribs geometry as the ribs geometry in

chapter 3. Improving the performance of COP Improvement factors in the transition flow also highlights. Chapter 5 describes the correlation of flow structure with the performance of heat transfer and pressure drop. In this chapter, in general, the effect of secondary flow ribs on the downstream side is not apparent. However, observations on the local flow around ribs show similarity and strength of shape to fluid flow around ribs in straight tubes. Whereas in chapter 6, ribs performance is tested on real-scale and transient conditions. In this chapter, the first 60 minute-operation analysis is carried out to find out the details of thermal phenomena in ribs and plain coil in a laminar and turbulent flow. Continuous operation and 120-minute intermittent mode are also performed to determine the increase in thermal performance in this condition. The effect of intermittent and continuous conditions on the soil side was also observed. The use of copper, composite, and HDPE is also carried out to determine its impact on the performance of thermal ribs and plain coil.

1.4 References

Administration, U. S. E. I. (2019). International Energy Outlook 2019 with projections to 2050. In *Choice Reviews Online*. https://doi.org/10.5860/CHOICE.44-3624

Ali, M. H., Kariya, K., & Miyara, A. (2017). Performance analysis of slinky horizontal ground heat exchangers for a ground source heat pump system. *Resources*, *6*(4), 1–18. https://doi.org/10.3390/resources6040056

ASHRAE. (2009). *ASHRAE handbook-Fundamentals (SI)*. ASHRAE Editor.

Atam, E., & Helsen, L. (2016). Ground-coupled heat pumps: Part 2 - Literature review and research challenges in optimal design. *Renewable and Sustainable Energy Reviews*, *54*, 1668–1684. https://doi.org/10.1016/j.rser.2015.07.009

Banks, D. (2008). *An introduction to thermo geology: ground source heating and cooling*. Wiley-Blackwell Publishing Ltd.

Beier, R. A. (2014). Transient heat transfer in a U-tube borehole heat exchanger. *Applied Thermal Engineering*, *62*(1), 256–266. https://doi.org/10.1016/j.applthermaleng.2013.09.014

Chiasson, A.D. and Yavuzturk, C. (2009). A design tool for hybrid geothermal heat pump systems in cooling-dominated buildings. *ASHRAE Transactions*, *115*, 75–87.

Chiasson, A. D. (2010). Modeling horizontal ground heat exchangers in geothermal

heat pump systems. *COMSOL Conference 2010*. Retrieved from https://www.comsol.jp/paper/download/114861/chiasson_paper.pdf

Eskilson, P. (1987). *Thermal analysis of heat extraction boreholes*. University of Lund.

Fisher, D.E., Rees, S. J. (2006). Implementation and validation of ground-source heat pump system models in an integrated building and system simulation environment. *HVAC&R Research*, *12*, 693-710.

Florides, G., & Kalogirou, S. (2007). Ground heat exchangers-A review of systems, models and applications. *Renewable Energy*, *32*(15), 2461–2478. https://doi.org/10.1016/j.renene.2006.12.014

Genchi, Y., Kikegawa, Y., & Inaba, A. (2002). CO2 payback-time assessment of a regional-scale heating and cooling system using a ground source heat-pump in a high energy-consumption area in Tokyo. *Applied Energy*, *71*(3), 147–160. https://doi.org/10.1016/S0306-2619(02)00010-7

Kavanaugh, S.P. and Rafferty, K. (1997). *Ground-Source Heat Pumps, Design of Geothermal Systems for Commercial and Institutional Buildings*. Atlanta: ASHRAE.

Kavanaugh, S.P. and Rafferty, K. (2014). *Geothermal heating and cooling, Design of ground source heat pump systems*. ASHRAE.

Li, X. wei, Meng, J. an, & Guo, Z. yuan. (2009). Turbulent flow and heat transfer in discrete double inclined ribs tube. *International Journal of Heat and Mass Transfer*, *52*(3–4), 962–970. https://doi.org/10.1016/j.ijheatmasstransfer.2008.07.027

Li, X. wei, Yan, H., Meng, J. an, & Li, Z. xin. (2007). Visualization of longitudinal vortex flow in an enhanced heat transfer tube. *Experimental Thermal and Fluid Science*, *31*(6), 601–608. https://doi.org/10.1016/j.expthermflusci.2006.06.007

Meng, J. A., Liang, X. G., & Li, Z. X. (2005). Field synergy optimization and enhanced heat transfer by multi-longitudinal vortexes flow in tube. *International Journal of Heat and Mass Transfer*, *48*(16), 3331–3337. https://doi.org/10.1016/j.ijheatmasstransfer.2005.02.035

Sanner, B., Karytsas, C., Mendrinos, D., & Rybach, L. (2003). Current status of ground source heat pumps and underground thermal energy storage in Europe. *Geothermics*, *32*(4), 579–588. https://doi.org/10.1016/S0375-6505(03)00060-9

Sarbu, I., & Sebarchievici, C. (2014). General review of ground-source heat pump systems for heating and cooling of buildings. *Energy and Buildings*, *70*, 441–454.

https://doi.org/10.1016/j.enbuild.2013.11.068

Selamat, S., Miyara, A., & Kariya, K. (2016). Numerical study of horizontal ground heat exchangers for design optimization. *Renewable Energy*, *95*, 561–573. https://doi.org/10.1016/j.renene.2016.04.042

Self, S. J., Reddy, B. V., & Rosen, M. A. (2013). Geothermal heat pump systems: Status review and comparison with other heating options. *Applied Energy*, *101*, 341–348. https://doi.org/10.1016/j.apenergy.2012.01.048

Urchueguía, J. F., Zacarés, M., Corberán, J. M., Montero, Á., Martos, J., & Witte, H. (2008). Comparison between the energy performance of a ground coupled water to water heat pump system and an air to water heat pump system for heating and cooling in typical conditions of the European Mediterranean coast. *Energy Conversion and Management*, *49*(10), 2917–2923. https://doi.org/10.1016/j.enconman.2008.03.001

Wu, Y., Gan, G., Gonzalez, R. G., Verhoef, A., & Vidale, P. L. (2011). Prediction of the thermal performance of horizontal-coupled ground-source heat exchangers. *International Journal of Low-Carbon Technologies*, *6*(4), 261–269. https://doi.org/10.1093/ijlct/ctr013

Wu, Y., Gan, G., Verhoef, A., Vidale, P. L., & Gonzalez, R. G. (2010). Experimental measurement and numerical simulation of horizontal-coupled slinky ground source heat exchangers. *Applied Thermal Engineering*, *30*(16), 2574–2583. https://doi.org/10.1016/j.applthermaleng.2010.07.008

Yeung, K.-W. (1996). *Enhancements to a ground loop heat exchanger design program*. Oklahoma State University.

Yuan, Y., Cao, X., Sun, L., Lei, B., & Yu, N. (2012). Ground source heat pump system: A review of simulation in China. *Renewable and Sustainable Energy Reviews*, *16*(9), 6814–6822. https://doi.org/10.1016/j.rser.2012.07.025

Yuan, Y., Cao, X., Wang, J., & Sun, L. (2016). Thermal interaction of multiple ground heat exchangers under different intermittent ratio and separation distance. *Applied Thermal Engineering*, *108*, 277–286. https://doi.org/10.1016/j.applthermaleng.2016.07.120

Zhang, C., Yang, W., Yang, J., Wu, S., & Chen, Y. (2017). Experimental investigations and numerical simulation of thermal performance of a horizontal slinky-coil ground heat exchanger. *Sustainability (Switzerland)*, *9*(8), 1–22. https://doi.org/10.3390/su9081362

Zheng, N., Liu, W., Liu, Z., Liu, P., & Shan, F. (2015). A numerical study on heat transfer enhancement and the flow structure in a heat exchanger tube with discrete double inclined ribs. *Applied Thermal Engineering*, *90*, 232–241. https://doi.org/10.1016/j.applthermaleng.2015.07.009

CHAPTER

2

GENERAL VIEW OF GROUND-SOURCE HEAT PUMP SYSTEM AND LITERATURE REVIEW

2.1 Ground Source Heat Pump

Sustainable development makes stakeholders promote efficiency in the use of energy as an economic strategy in several countries in the world. The right use of energy in buildings has excellent potential in cost savings. The right use of energy in buildings has excellent potential in cost savings. Some studies also show that energy savings are the easiest way to reduce greenhouse gas emissions. Energy requirements for heating and cooling in buildings contribute 80% of energy use in buildings, while energy use for heating and cooling of buildings continues to increase from year to year. The use of renewable energy as an alternative energy source for buildings must be taken seriously to realize the reduction of fossil energy and CO_2 emissions mentioned as the goal of the Kyoto protocol.

Several countries have established a framework for promoting energy from renewable sources. This framework opens opportunities for the use of renewable energy sources in the heat pump for cooling and heating in new and existing buildings. The GSHP system offers higher energy efficiency compared to conventional heat pumps. This high efficiency is because underground temperatures are hotter for heating and

lower for cooling the room, while conventional heat pumps have fluctuating performance depending on ambient air temperature.

The use of thermal energy from the ground for the first time recorded patented in Switzerland in 1912 (Ball and Fischer, 1983). GSHP technology began in demand in North America and Europe after the Second World War and lasted until the early 1950s when fossil fuels were widely used as heaters. At that time, the primary analytical theory for heat conduction from the GSHP system proposed by Ingersoll and Zobel (1954) was used as a foothold in developing the Ground Heat Exchanger design. In the next two decades, many attempts were made to standardize installation and development in designing vertical drill systems (Eskilson, 1987; Bose and Parker, 1985; Kavanaugh and Rafferty, 1997). Until now, the GSHP system has been widely used both in residential and commercial buildings. The utilization of GSHP is estimated to have been proliferating and continues to range from 10% to 30% each year lately.

The heat pump is a device that works based on the reversed Carnot cycle that uses energy as a driving force and produces thermal effects. Each heat pump works by pumping heat from a low-temperature reservoir to a high-temperature reservoir and consumes energy as a driving force. Sources of heat can be obtained from gas or air (outdoor air. Hot air produced by industry), liquids (surface water, groundwater or hot wastewater), and soil. Heat users take advantage of the thermal energy generated by the heat pump at higher temperatures. This use can be in the form of room heating, which includes wall heating, warm air or convective systems, and water heating, which includes swimming pools, bathwater, and hot-water technology. The use of heat can be recommended for cold use because the system can be done reversibly so that the cooling mode works similar to a heat pump such as a central air conditioner. Heat pumps can be produced using several methods, namely electrical energy (electro-compressor), mechanical energy (mechanical compressors with expansion turbines), thermo-mechanical energy (steam ejector system), thermal energy (absorption cycle), and thermo-electric energy (effects Peltier).

The GSHP system is an electro-compressor type heat pump. Increasing the low temperature to more than 38C and moving into the room involves the process of evaporation, compression, condensation, and expansion (Figure 2.1). Non-CFC refrigerant is used as a heat transfer fluid that circulates in the heat pump.

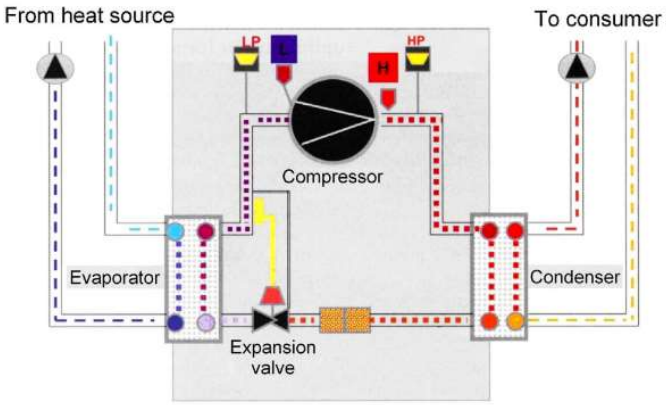

Figure 2.1 Principle of a heat pump (Sarbu & Sebarchievici, 2014)

At present, the GSHP system receives much attention because it has advantages in the form of high efficiency and environmental friendliness (Heinonen et al., 1996; Sarbu, 2010a, 2010b; Bose and Smith, 2002; Luo et al., 2013; Pahud and Matthey, 2001). The forms of wind, solar, biomass, hydro, and earth energy produce low greenhouse gas emissions.

Ground temperature has a constant temperature character compared to ambient temperature air. The soil is warmer in winter and cooler in summer than outdoor air. So, the ground is considered as an efficient source of heat. The GSHP system is divided into three components, namely the connected subsystem on the ground, the heat pump subsystem, and the heat distribution subsystem.

GSHP is the choice in saving energy rather than conventional systems in the following applications

- in terms of construction, this technology is relatively easy to implement or to replace an old system.
- in terms of climate where changes in daily temperatures are big or in subtropical countries and where electricity costs are higher than average.
- in areas where natural gas is not available, and electricity costs are high.

2.2 Type of Heat Pump

Heat pumps are divided based on absorption and heat dissipation, hot and cold fluid distribution systems, and thermodynamic cycles.

- The air pump uses air. This type of heat pump is the most widely used and the most widely produced by the company.

- Heat pump from water to air. This heat pump uses water as a heat transfer medium to absorb and dissipate heat and uses air to distribute heat to or from conditioned rooms. The division of this heat pump is divided as follows.

- Groundwater heat pumps that use groundwater from as a heat sink and heat source.
- surface water heat pumps that use surface water from lakes, ponds, and running water as sources of heat sinks and heat dissipation.
- Heat pump with the help of the sun that relies on solar energy as a source of heat.

- Water to water heat pump. This heat pump uses water as a source of heat and heat dissipation for permanence and cooling. Heating and cooling can be done with an adjustable refrigeration cycle.
- Ground source heat pump. This heat pump uses soil as a source of heat absorption and heat dissipation. The heat pump has a water heat exchanger to the refrigerant. The heat exchanger refrigerant to water use antifreeze solutions. The solutions are pumped using vertical, horizontal, or circular pipes that are installed under the ground.
- The hybrid ground source heat pump is a variant that utilizes an air-cooled cooling tower or condenser to reduce the total heat absorbed and discharged from the ground.

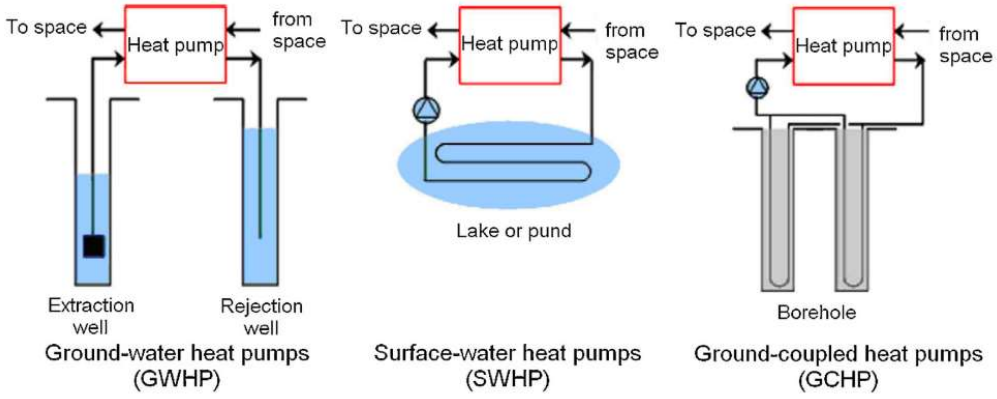

Figure 2.2 Schematics of different ground-source heat pumps (Sarbu & Sebarchievici, 2014)

2.3 Description of GSHP

GSHP is a closed-loop heat pump. The GSHP system is divided into reversible vapor compression connected to a Ground Heat Exchanger (GHE), which is buried in the soil. Based on its type, GSHP is divided into horizontal GHE and vertical GHE.

Horizontal GHE (Figure 2.3 a) is divided into three subgroups: single pipe, multiple pipe, and spiral. Horizontal GHE is buried in a trench as deep as 1-2 m from the ground surface. This pipe is connected in parallel with other pipes. Horizontal GHE was developed to save the area of land used. Several pipes are placed in a single trench so that it can reduce the area of land used. Trench collectors (Figure 2.3 b) are widely applied in North America and Europe.

The use of spiral coil (figure 2.4) is utilized to reduce the need for land area. The distance between the coil is 0.6, up to 1.2 m. The end of one parallel coil is connected with a manifold-collector that can collect several coils, which then the fluid is transported to several main pipes in the heat pump. The disadvantages of horizontal GHE are (1) ambient temperature fluctuations greatly influence the system, (2) the more land is needed to install this GHE is more than the vertical system.

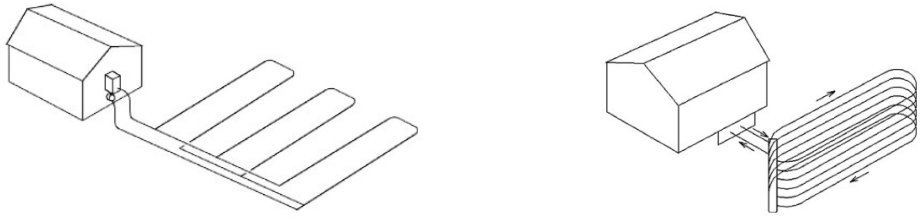

(a) (b)

Figure 2.3 a. Horizontal ground heat exchanger, b. Trench collector (Sarbu & Sebarchievici, 2014)

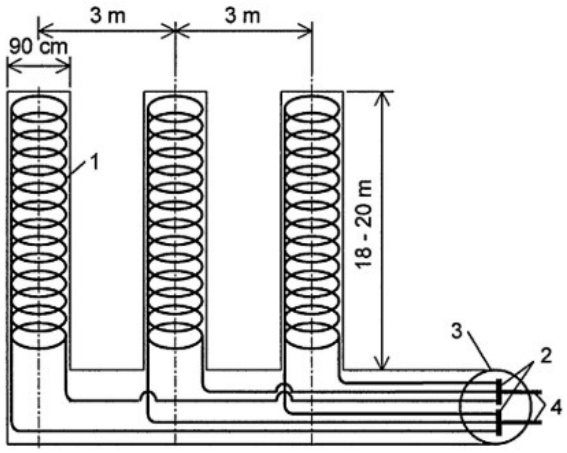

Figure 2.4 Spiral Ground Coil (Sarbu & Sebarchievici, 2014)

In a vertical GHE system, this type of GHE can be installed one, tens, or even hundreds in a borehole. Each borehole can contain one or two U-tubes where the heat-conducting fluid circulates. U-tube has a characteristic that is the tube diameter between

20-40 mm, and the borehole has a depth ranging from 20-200 m with a borehole diameter between 100 mm to 200 mm. Borehole annulus sides are usually filled with special material (grout) to prevent groundwater contamination. A vertical U-tube can be seen in Figure 2.5.

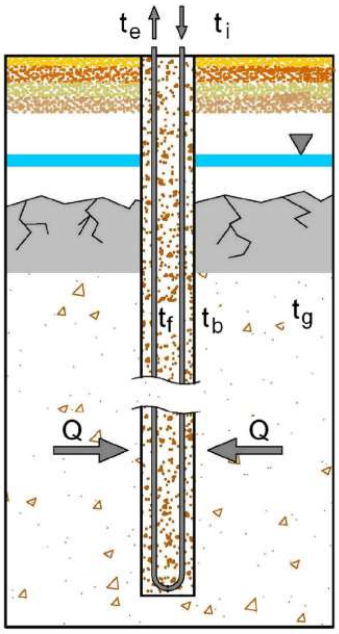

Figure 2.5 Schematics of a vertical grouted borehole (Sarbu & Sebarchievici, 2014)

Borehole length is calculated based on the assumption of steady-state heat transfer as follows:

$$L = \frac{qR_g}{t_g - t_f} \tag{2.1}$$

Where q is the heat transfer rate (kW), tg is the ground temperature (K), tf the working fluid temperature (K), Rg is the effective thermal resistance of the long unity ground (mK / kW).

GHE is generally designed in the worst conditions. This design is based on the consideration of thermal pulse fluctuations in various magnitudes and time frames. Qa average soil load for 20 years. The highest monthly qm load for one month, and the peak qh load for 6 hours. The length of the borehole required for heat transfer is calculated as follows

$$L = \frac{q_h R_b + q_a R_{20a} + q_m R_{1m} + q_h R_{6h}}{t_f - (t_g + \Delta t_p)} \tag{2.2}$$

Where, R_b is the effective thermal borehole resistance. R_{20a}, R_{1m}, R_{6h} are effective thermal ground resistance for 20 years, one month, and 6-hour thermal fluctuations,

respectively. t_g is an increase in temperature due to thermal disturbance between adjacent boreholes.

Effective thermal resistance is very dependent on the thermal conductivity of the soil. Another factor that contributes to the effective thermal resistance is the borehole diameter and the ground thermal diffusivity. The advantages of vertical GHE are (1) the area of land required is relatively small, (2) the slight influence of soil temperature variation on property, (3) the pipe, and pump energy required is relatively small, (4) able to produce more efficient GSHP performance. However, vertical GHE has a disadvantage, namely the use of expensive equipment for drilling.

2.4 Ground Heat Exchanger

In recent decades, many researchers have investigated GHE. This research includes numerical studies, analytic experiments, and optimization. Generally, research on GHE is divided into four categories, namely GHE geometry, pipe material, working fluid, and depth of installation on the ground.

Based on related research on GHE geometry, U pipe is the most studied geometry that covers the configuration of U pipe, double U pipe, triple u-pipe, and multi-tube. Double U type GHE has better performance than single u-pipe GHE shown by Adamovsky et al. (2015). The results of this study conclude that the u-pipe heat exchanger produces 7W/m higher than a single u-pipe. Florides and Kalogirou (2007) concluded that the double u-pipe has higher efficiency than a single u-pipe, while the construction costs are 22-29% greater than a single u-pipe. The highest performance rating is achieved by triple u-pipe, followed by double u-pipe and w-pipe. Although the thermal power of the double u-pipe length is 8-10% higher than the single u-pipe, when the depth of the borehole is kept constant, the thermal resistance of the first case is 70% greater than the second case.

The helical type GHE is the most widely used heat exchanger after the u-pipe. Based on Dehghan et al. (2016), The optimal values of coil and pitch coil diameter are 0.45 and 0.1 m. A 100% increase in coil and pitch coil diameter can result in a 10% increase in performance and drilling. Helix coil with a small pitch can save energy as well as a more even distribution of heat flux and temperature. In short and long term usage, the helix coil has better performance than W-pipe and single u-pipe. Yang et al. (2016) stated that helix pitch optimization efforts are needed to get the best heat transfer

rate per meter, installation costs, and the availability of boreholes. Jalaluddin and Miyara (2015) concluded that there was an increase in pressure drop per meter borehole on the helix coil. They also stated that the heat transfer rate and efficiency of the helix pipe system were higher than that of a single u-pipe. Zarrella et al. (2017) examined the superiority of helix pipe performance over coaxial pipes. Zarrella et al. (2017) concluded that heat transfer performance did not experience a significant change in helix pitch changes.

2.4.1 Simulation and Modelling of Ground Heat Exchanger

The goal of the GHE thermal analysis is to estimate the temperature of the working fluid, which circulates on the U-tube and heat pump under several operating conditions. The heat transfer process in GHE mainly involves many uncertain variables such as the thermal nature of the soil, groundwater flow, and the burden of GHSP use in a long time. So the heat transfer process becomes complicated and must be calculated based on transient conditions. For simplicity, the heat transfer process is analyzed from two aspects. The first aspect is solid soil and rock in a borehole, where conduction heat transfer occurs transiently while the second aspect is around the borehole, namely in the borehole, grout material, u-tube, and fluid circulation in the pipe.

Analysis of two spatial zones associated with borehole walls. The heat transfer model in two separate zones is carried out by the following method

- Conduction heat transfer outside the borehole

Several simulation models for heat transfer have been carried out lately. Most of these models are based on numerical and analytic methods.

- Kevin's line source. The first method for calculating heat transfers around a ground heat exchanger is Kevin's line source. This method is calculated using the infinite line source approach [3,25]. Based on this method, the response to soil temperature due to constant heat transfer is calculated as follows

$$t(r,\tau) - t_0 = \frac{q_1}{4\pi\lambda}\int_{\frac{r^2}{4a\tau}}^{\infty}\frac{e^{-u}}{u}\,du \qquad (2.3)$$

Where r is the distance from the line-source, and τ is the time since the beginning of the operation. t is the temperature at distance r and time τ. t_0 is the initial ground temperature. q_1 is the heating rate per source line length. λ and a are the thermal diffusivity conductivity of the soil. The Cylindrical source model was used to calculate

the constant heat transfer developed by Carslaw and Jaeger (1946), then this method was revised by Ingersoll and Zobel (1954) and then developed in several studies.

- Cylindrical source model. The distribution of soil temperature is given in cylindrical coordinates based on the transient heat transfer equation with the given boundary conditions and initial conditions as follows

$$\frac{\partial^2 t}{\partial r^2}+\frac{1}{r}\frac{\partial t}{\partial r}=\frac{1}{a}\frac{\partial t}{\partial \tau} \qquad r_b < r < \infty$$

$$-2\pi r_b \lambda \frac{\partial t}{\partial \tau}=q_1 \qquad r = r_b, \tau > 0$$

$$t - t_0 = 0 \qquad \tau = 0, r > r_b$$

  Where r_b is the radius of borehole

  The solution of a cylindrical source is given as follows

$$t - t_0 = \frac{q_1}{\lambda} G(z,p) \qquad (2.4)$$

  where $z = a\tau/r_b, p = r/r_b$

  Carslaw & Jaeger (1946) show the term G (z, p), which is a function of distance and time from the center of the borehole. Hellstrom (1991) found a method to estimate the value of G.

- Eskilson's model. the two models mentioned earlier ignore axial heat transfer along the borehole. Eskilson (1987) made improvements to explain the axial displacement of the borehole at a certain length. Basic calculations of soil temperature use the conduction heat transfer equation in cylindrical coordinates.

$$\frac{\partial^2 t}{\partial r^2}+\frac{1}{r}\frac{\partial t}{\partial r}+\frac{\partial^2 t}{\partial z^2} = \frac{1}{a}\frac{\partial t}{\partial \tau}$$

$$t(r,0,\tau) = t_0$$

$$t(r,z,0) = t_0$$

$$q_1(\tau) = \frac{1}{L}\int_D^{D+L} 2\pi r \lambda \frac{\partial t}{\partial r}$$

  Where the L value is the depth of the borehole, D is the top of the borehole and can be ignored in technical applications.

The final formula of the temperature response at the borehole to the step heat pulse unit is a function of τ/τ_s and r_b/L only:

$$t_b - t_0 = -\frac{q_1}{2\pi\lambda} f\left(\frac{\tau}{\tau_s}, \frac{r_b}{L}\right)$$

Where s $\tau_s = L^2/9a$ is a steady state condition. The f-function is basically a dimensionless temperature response inside a borehole wall that is calculated numerically.

- Finite line-source solution. An analytic solution was developed by several researchers based on Eskilson's model for finite length source. This model considers the influence of the depth of the borehole and the ground surface as a boundary.

The excess temperature solution was analyzed as follows

$$t(r,z,\tau) - t_0 = \frac{q_1}{4\pi\lambda}\int_0^L \left[\frac{erfc\left(\frac{\sqrt{r^2+(z-l)^2}}{2\sqrt{a\tau}}\right)}{\sqrt{r^2+(z-l)^2}} - \frac{erfc\left(\frac{\sqrt{r^2+(z+l)^2}}{2\sqrt{a\tau}}\right)}{\sqrt{r^2+(z+l)^2}} \right] \quad (2.5)$$

In equation 2.5, the temperature in the borehole wall, where r = rb, varies with the change in time and depth of the borehole. The temperature in the middle of the borehole (z = L / 2) is chosen based on its representative temperature. Alternative integral temperature averages along the borehole are calculated using numerical integration equation 2.5.

- Other common numerical models. Hellstrom (1991) and Thornton et al. (1997) examined a simulation model for ground heat storage. This method is used in heat exchangers with solid loops used for seasonal thermal energy storage. Muraya and O'Neal (1996) proposed a finite element transient model around the vertical borehole U-tube in the GSHP system to determine the thermal interference that occurs between the GHE u-tubes.

- Heat transfer inside the borehole. Thermal resistance in the borehole in the form of grouting material or flow regulation in the borehole has a significant effect on GHE performance. This analysis aims to determine the temperature of entry and exit from the working fluid flowing inside the borehole according to the temperature of the borehole wall, heat flow, and thermal resistance.

- One-dimensional model. This one-dimensional model has been suggested for GHE design with the assumption that the U-tube is a single "equivalent" pipe (Bose and Parker, 1985; Gu, 1998).
- Two-dimensional model. Thornton et al. (1997) produced a two-dimensional analytical solution of thermal resistance between pipes perpendicular to the borehole axis. This method is superior to empirical methods and One-dimensional models.
- Semi-three-dimensional model. Based on the two methods mentioned, the Quasi-three-dimensional model studied by Zeng and Diao (2003). This method considers variations in fluid temperature along the borehole.

2.5 Longitudinal Vortex Generator

2.5.1 Discrete Double Inclined Ribs

In general, the method of increasing heat transfer is divided into three groups, namely the active method, the passive method, and the compound method (Liu and Sakr, 2013). The application of the augmentation method can undoubtedly increase convection heat transfer, but this method increases pump power consumption to overcome energy losses due to pressure drop (Alam and Kim, 2018). The use of excessive pump power can be a dilemma in the performance of energy conservation and environmental conditioning, so the method of increasing heat transfer needs to be done carefully. Therefore, energy-saving from increasing heat transfer and energy-loss from pressure drop should be a significant consideration in the application of augmentation methods.

Vortex flow generation techniques are described in this section. This technique covers artificial roughness (ribs and grooves), specially shaped tubes, multiple longitudinal vortexes generating devices, and longitudinal vortex generators. By using these methods, flow can produce longitudinal vortices in both laminar and turbulent flow. The flow structure which is formed depends on the applied method, but the effect of the flow structure can vary on heat transfer, and the flow performance can vary with flow conditions.

Based on studies of optimizing heat transfer, Meng et al. (2005) recommends using a new tube called the discrete double inclined ribs (DDIR-tube) shown in Figure Figure 2.6. They examined the thermo-hydraulic performance of the tube with an

experimental approach and numerical simulation at Re 500≤Re≤15,000. Figure Figure 2.7 shows the flow structure of numerical simulation results on the cross-section in DDIR-tube at Re = 1000. The DDIR-tube wall induces three longitudinal pairs of the vortex. The study showed Nu increased 250-650% with f increasing 120–300% at 500 <Re <2300 while Nu increased 240-110% and f increasing 3–210% in for 2300 <Re <15000. This improvement shows that DDIR-tube can produce excellent thermal and hydraulic performance.

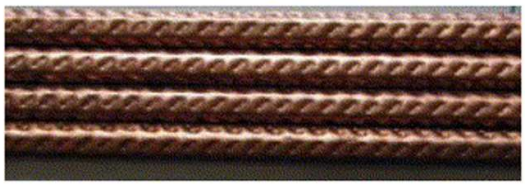

Figure 2.6 Photo of the DDIR-tube (Zheng, Yan, Zhang, Zhou, & Sun, 2020)

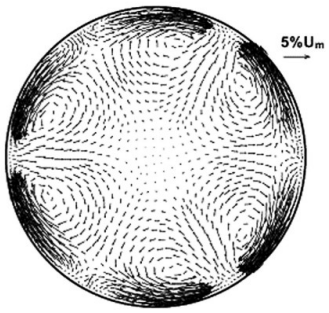

Figure 2.7 Cross-section flow field in the enhanced tube for Re =1000 (Zheng et al., 2020)

Li et al. (2007) conducted a visualization study in an enlarged DDIR-tube with dye injection to determine the structure of the vortex. They concluded that ribs raised the counter-rotating longitudinal pair of vortexes. Li et al. (2009) continued an investigation to examine the hydrodynamics and thermal performance of DDIR-tube at 15000 <Re <60000. They analyzed the flow structure and discovered the physical mechanism of heat transfer intensification and optimal DDIR-tube configuration through parametric studies.

Zheng et al. (2015) submitted a modified DDIR-tube where ribs were attached to the inner surface of the tube, as shown in figure 2.8. They investigated the performance of the tube on the turbulent flow structure at 3390 <Re <20,340. Six longitudinal vortices are induced in the tube, as shown in Figure 12. The Nusselt number of modified DDIR-tubes increased from 80 to 260%, while friction factors increased by

110-460% when compared to smooth tubes in specific Reynolds number ranges. Afterward, Zheng et al. (2016a) evaluates the performance of DDIR-tube thermo-hydraulic on V-type and P-type by using a numerical approach, as shown in Figure 2.10.

Figure 2.11 illustrates that a longitudinal vortex is in the entire tube region; however, three pairs of vortices in different directions were induced by a V-type DDIR-tube. These three pairs of the vortex have more significant turbulence kinetic energy than a single vortex. This research shows that the temperature difference between V-type and P-type at 6780 <Re <20340 is 35.7-36.7 K and 36.9-37.4 K, respectively. These results indicate that three small pairs of the vortex are more able to reduce temperature differences than a longitudinal vortex. Besides, Nu and f of V-type ribs are 57–76% and 86–94% greater than P-type.

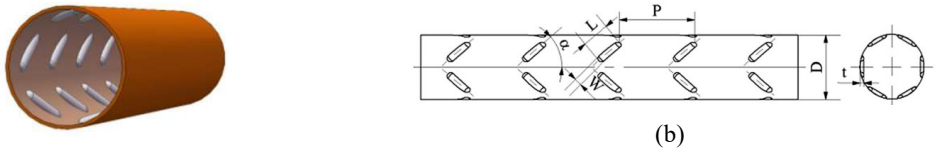

(a) (b)

Figure 2.8 Schematics of a modified DDIR-tube (a) 3D view (b) 2DView (Zheng et al., 2020)

(a) (b)

Figure 2.9 Cross-section flow structure in the modification of DDIR-tube (a) velocity vectors, (b) streamlines (Zheng et al., 2020)

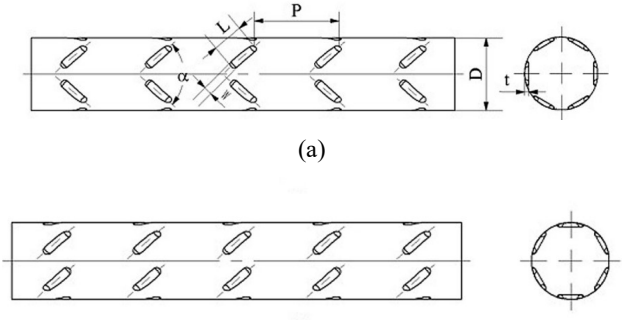

(a)

(b)

Figure 2.10 Schematics of the ribbed tubes (a) V-type tube; (b) P-type tube (Zheng et al., 2020)

(a) (b)

Figure 2.11 Cross-section flow structure in the P-type ribbed tube (Re = 10170)

(a) Velocity vectors (b) streamlines (Zheng et al., 2020)

2.5.2 Discrete Double Inclined Grooves

Groove is an artificial roughness that is often used, and they are similar to ribs. The difference between groove and ribs is convex ribs, while the concave groove is on the inner wall of the tube. Based on the structural similarity between grooves and ribs, Zheng et al. (2017) investigated discrete double inclined grooves to see heat transfer performance and pressure drop with minimal fluid power consumption. Geometry discrete double inclined grooves that look similar to ribs can be seen in figure 2.13 (Zheng et al., 2015).

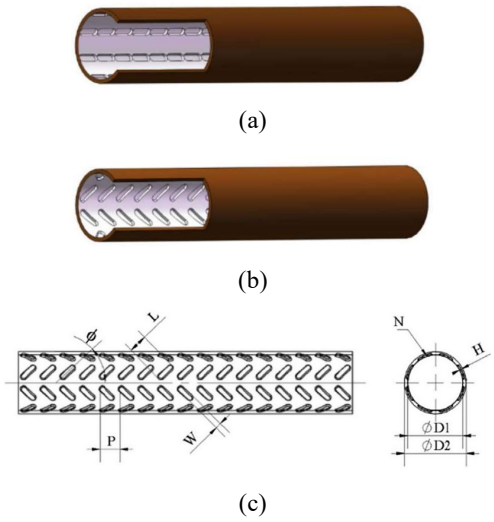

(a)

(b)

(c)

Figure 2.12 Schematics of a tube with discrete grooves (Zheng et al., 2020)

Numerical simulations were performed to observe the heat transfer and pressure drop characters in the grooved tube at 6780 <Re <20340. Figure 2.13 shows eight vortices induced to move cold fluid from the core flow to the tube wall, and the hot fluid near the wall moves to the core flow, which indicates an increase in fluid mixing.

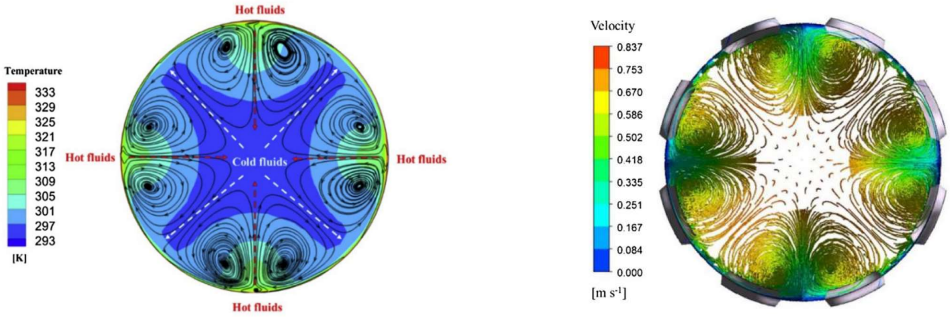

(a) (b)

Figure 2.13 (a) Cross-section temperature distributions and surface streamlines in the grooved tube at Re = 1017; (b) Three-dimensional streamlines in the enhanced tube at Re 10170 (Zheng et al., 2020)

Zheng et al. (2016b) also investigated the combination of the rib-grooved tube with a pattern of discrete double inclined ribs and grooves alternately on the tube wall to produce a longitudinal vortex that can increase heat transfer.

2.5.3 Special-shaped tubes

Straight tubes and circular tubes are widely used in industrial applications, but the tubes are shaped like non-circular tubes and twisted tubes made by changing the shape of circular tubes, capable of producing increased heat transfer because the resulting flow structure has a longitudinal vortex. This tube has the potential to produce a balance between energy loss due to pressure drop and energy saving due to heat energy.

Meng et al. (2005) investigated a new tube variation called alternating elliptical axis (AEA) tube. As shown in Figure 2.14 a, AEA tubes are made of segmented elliptical tubes with alternating axes and transition joints are used to connect alternative segments. Numerical simulations to see the performance of the AEA tube are carried out on the Reynolds number from 500 to 50000. The results of this study appear in figure 2.14 b, eight vortices are raised near the wall, and this vorticity causes the fluid in the center of the pipe to move toward the wall.

Compared to ribbed and grooved tubes, AEA tubes have the advantage of simple structure, and low manufacturing costs so that these tubes are more promising for increased heat transfer with a longitudinal vortex. However, the use of AEA tube is not too much compared to ribbed and grooved tubes. Deeper investigation is needed to look for special-shaped tubes that can generate longitudinal vortex.

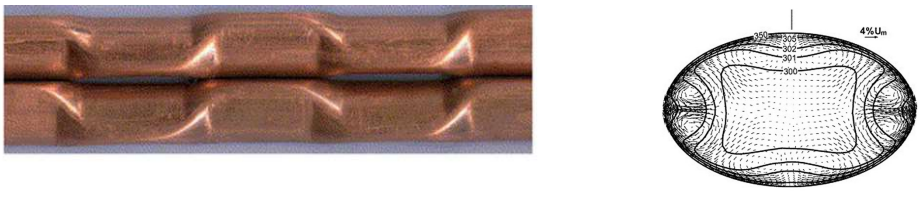

(a) (b)

Figure 2.14 (a) Alternating elliptical axis tube; (b) Flow structure and temperature fields in the AEA tube (Zheng et al., 2020)

2.5.4 Multiple swirl devices

The use of single swirl devices such as twisted tapes, wired coils, and helical screw-tapes is another way to produce longitudinal vortex flow in the tube. Thus, the combined use of a longitudinal vortex generator can build a flow structure that has a longitudinal vortex, as seen in Figure 2.15.

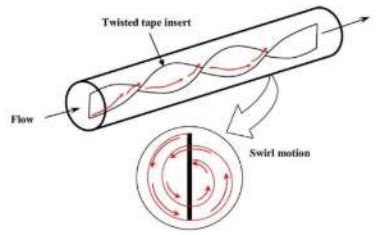

(a) Single Twisted tape insert

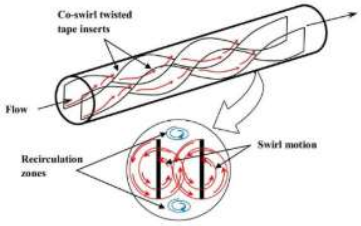

(b) Twin co-swirl twisted tape inserts

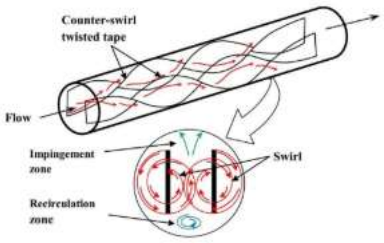

(c) Twin counter-swirl twisted tape inserts

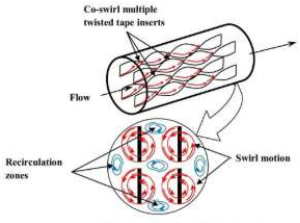

(d) Four co-swirl twisted tape inserts

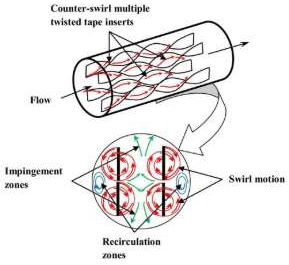

(e) Four counter-swirl twisted tape insert

Figure 2.15 Flow Mechanism in the tube fitted with multiple twisted tape (Zheng et al., 2020)

Eiamsa-ard et al. (2010) investigated the structure of flow and heat transfer in tubes using twin counter twisted tapes (CTs) or co-twisted tapes (CoTs) in the Reynolds number range from 3700 to 21000 by using water as a working fluid. In figure 21, single and double swirl streams are induced by single twisted tape and twin twisted tapes, respectively. It should be understood that the two recirculation areas are produced by CoTs and the clearance area of the twisted tape. On the other hand, there is no recirculation zone generated by CT. Two primary vortices converge between clearance of twisted tape, which can increase the intensity of the vortex.

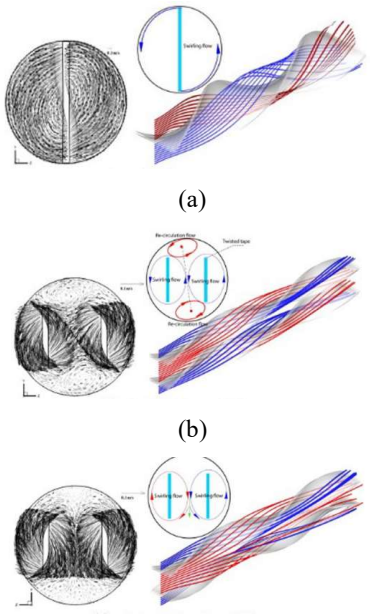

(a)

(b)

(c)

Figure 2.16 Flow structure in the tube fitted with twisted tape (a) single twisted tape; (b) twin co twisted tapes (CoTs); (c) Twin counter twisted tapes (CTs) (Zheng et al., 2020)

Chokphoemphun et al. (2015) observed the performance of heat transfer on tubes with multiple twisted tapes in the Reynolds number range between 5300 to 24000. Figure 22 shows that varied numbers of the tapes from 1 to 4 and both co-and counter-twist configurations are taken into consideration. This research resulted in an increase in Nusselt number and friction factors by increasing the number of twisted tapes in the same twist configuration.

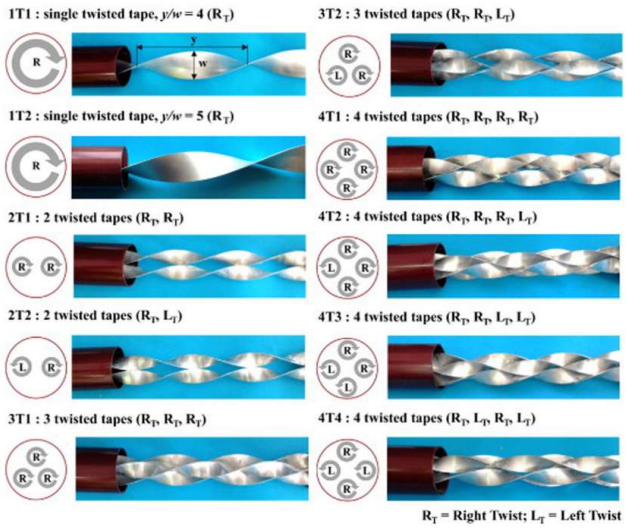

Figure 2.17 Different configurations of twisted tape (Zheng et al., 2020)

2.6 Heat Transfer and Flow in Coil

Heat transfer and fluid flow in coil pipes are widely applied in large quantities in piping systems, biofluid mechanics, industrial equipment such as heat exchangers, electric engine cooling systems, chemical mixing machines, ground source heat pump systems, and other process equipment. Because the use of coil is extensive, the character of heat transfer and fluid flow has been widely studied over the past few decades. The physical phenomenon of fluid flow in the coil pipe is very complicated because the presence of curvature produces centrifugal force and pressure in the curvature direction. Pressure force has a character that is far different from the centrifugal force. Pressure force decreases in curvature direction. The mutual effects of centrifugal force, pressure, inertia, and viscosity produce very complex flow patterns that are not yet fully understood. A general description of the qualitative physical description of the flow in the plain coil has been investigated by Yao (1975).

Many studies of fluid flow and heat transfer in coil pipes use analytical, numerical and experimental approaches. The first study of flow rates in the coil pipe was conducted by Dean (1927, 1928) by assumption the loosely curved pipe depends on a dean number $K = 2a/R(w_{max}\, a/\nu)^2$, a is the radius of the pipe and R is the radius of the curvature of the pipe, w_{max} is the maximum axial velocity based on in a straight pipe, and ν is the fluid kinematic viscosity. This research study is valid for K $\leq$ 576.

Furthermore, a lot of research on coil pipes is done with different Dean numbers. Conalogue (1968) added parameter $D = (Ga^2/\mu)(2a^3/\nu^2R)^2$, where G is the constant pressure gradient throughout the pipe. Another related parameter is K as $D =$

$4K^{1/2}$. Based on the definition of the Dean number, the upper limit of the number becomes 96. The use of the Fourier series can be used to solve numerical equations in the dean number ($96 \leq D \leq 600$). The approach using the finite difference method can solve the flow equation with a range of $96 \leq D \leq 5000$ done by Collins (1975), and Dennis and NG (1982).

The development of laminar flow research on coil pipes was carried out by Soh (1984) using an artificial compressibility method. They provide another definition for the Dean number for $108.2 \leq \kappa \leq 680.3$. $\kappa = 2\delta^{1/2}(W_m a/\nu)$ is another definition for the Dean number.

They concluded that the curvature ratio has a significant influence on the intensity of secondary flow and separation that occurs near the inner wall of the curved pipe. Flow studies in a similar stationary coil pipe were also carried out by Dennis and NG (1982), Ito (1987), and Kao (1992).

Nobari and Gharali (2006) observed the influence of internal fins on the heat transfer and fluid flow that occurs in rotational straight pipes and stationary curved pipes. Ishigaki (1993, 1996, 1999) investigated heat transfer and fluid flow in rotational curved pipes to determine the effect of Coriolis force on complex flows.

The effort to increase the heat in the helical coil refers to the fact that the fluid experiences centrifugal force, causing the core fluid to move towards the outer wall by producing thinning of the boundary layers. Moreover, this phenomenon generates counter-rotating vortices that carry fluid to the pipe cross-section of the pipe. This vorticity can increase heat transfer than straight tubes. Improved heat transfer performance on corrugated walls occurs due to periodic interruption in the development of boundary layers. This boundary layer disturbance increases the heat transfer area, generates swirling flows, and is capable of producing unstable flow regimes.

Rainieri et al. (2012, 2013) experimented on the effect of corrugation depth and pitch on low Dean numbers. The wall curvature effect shows the same increase in heat transfer in both the corrugated and the smooth helically coiled tubes. On the other hand, at higher Dean numbers, wall corrugation results in a greater increase in displacement, as shown in Figure 2.18. These results indicate that the wall corrugation coil has great potential to improve heat transfer performance in industrial applications.

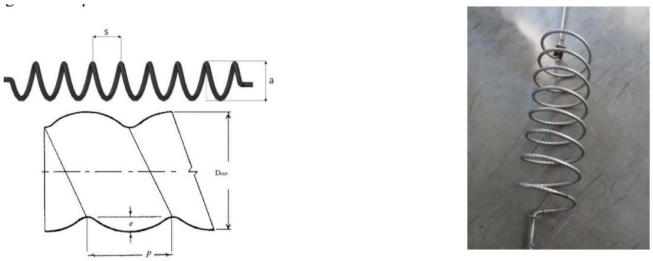

Figure 2.18 (a) Tube's geometry helical coil parameters (top) and wall corrugation profile (bottom); (b) coiled tube under test (Bozzoli, Cattani, & Rainieri, 2016)

2.7 Computational Fluid Dynamics

2.7.1 Basic of Computational Fluid Dynamics

Applying the fundamental laws of mechanics to fluids provides governing equations for fluids. Conservation of mass equation is

$$\frac{\partial \rho}{\partial t} + \nabla.(\rho \vec{V}) = 0$$

and the conservation of the momentum equation is

$$\rho \frac{\partial \vec{V}}{\partial t} + p(\vec{V}.\nabla)\vec{V} = -\nabla \mathrm{p} + \rho \vec{g} + \nabla.\tau_{ij}$$

These equations, together with the conservation of energy equations, form a set of partial differential equations coupled, nonlinear. It is not possible to solve this equation analytically for most technical problems. However, it is possible to obtain estimates of computer-based solutions to equations that govern various engineering problems. This is the subject of Computational Fluid Dynamics (CFD).

The CFD strategy is to replace the problem domain continuously with discrete domains using a grid. In a continuous domain, each flow variable is defined at each point in the domain. In the discrete domain, each flow variable is defined only at mesh points. In a CFD solution, someone will immediately solve the relevant flow variables only at grid points. Values at other locations are determined by interpolating the values at the grid points. Differential equations governing partial and boundary conditions are defined in terms of continuous variables. Someone can estimate this in the discrete domain in terms of discrete variables. A discrete system is a large set of algebraic equations in discrete variables. Setting up a discrete system, and solving it (which is a matrix inversion problem) involves a large number of repetitive calculations, tasks that we humans handle to digital computers.

2.7.2 Flow Boundary Layer

In simulating fluid flow and heat transfer in the pipe, the character of turbulent flow near the solid wall needs to be observed. Dimensional analysis needs to be done to connect the experimental data. In turbulent thin shear layer flows flow in pipes based on Reynolds number. Reynolds number calculation can be calculated based on the distance y away from the wall (Re). Inertia forces dominate the flow away from the wall. Because y is reduced to zero, the Reynolds number based on y will also be reduced to zero. Right before y reaches zero, the Reynolds number will be in the range of the value of y, which is Rey of the order of 1. The closer the wall, the viscous force will be equal or greater than the inertia force. Generally, flows along solid boundaries usually have a substantial region of inertia-dominated flow away from the wall and a thin layer within which viscous effects are significant. The approach to the flow wall is influenced by the viscous effect, which is not affected by the free stream parameter. Mean flow velocity depends only on the distance y from the wall, fluid density ρ and viscosity μ and the wall shear stress τ_w. Hence,

$$U = f(y, \rho, \mu, \tau_w)$$

The dimensional analysis shows that

$$u^+ = \frac{U}{u_\tau} = f\left(\frac{\rho u_\tau y}{\mu}\right) = f(y^+) \qquad 2.6$$

The formula above is called the law of the wall and consists of him dimensionless numbers u + and y. Note that the velocity scale is u_τ, $u_\tau = \sqrt{\tau_w/\rho}$, which is called frictional velocity. The farther away from the wall, the speed at one point will be influenced by the effect of wall slowing through the wall shear stress parameter. The length scale appropriate to this area depends on the thickness of the layer δ. In this region we have

$$U = g(y, \delta, \rho, \tau_w)$$

the use of dimensional analysis produces

$$u^+ = \frac{U}{u_\tau} = g\left(\frac{y}{\delta}\right)$$

This dimensional analysis is a useful parameter to see wall shear stress as a cause of a decrease in U-U speed, which is getting closer to boundary layer or pipe centerline. Hence,

$$\frac{U_{max} - U}{u_\tau} = g\left(\frac{y}{\delta}\right)$$

This formula is known as velocity-defect law

The stationary fluid is on a solid surface. The turbulent eddying motion also stops very close to the wall, and the fluid behavior near the wall is dominated by viscosity. The viscous sublayer is practically very thin (y + <5), and we can assume that shear stress is close to constant and the same as shear stress τ in all layers. So,

$$\tau(y) = \mu\frac{\partial U}{\partial y} = \tau_w$$

After integrating y and using the boundary condition U = 0 if y = 0, we get a linear relationship between average velocity and distance from the wall.

$$U = \frac{\tau_{wy}}{\mu}$$

Using simple algebra and making use of the definitions u + and y + produce

$$u^+ = y^+$$

Because the speed and distance from the wall have a linear relationship, the fluid layer near the wall is also called the laminar sub-layer. Beyond the viscous sublayer (30 $<y^+<500$), there are areas where viscous dominance and turbulent effects are equally important. Shear stress varies slowly with the distance of the wall. In this region, the interior is assumed to be constant and equal to shear stress. An assumption regarding the turbulent length scale allows the relationship of u^+ and y^+ to be obtained as follows

$$u^+ = \frac{1}{\kappa}\,ln(y^+) + B = \frac{1}{\kappa}\,ln(Ey^+) \qquad (2.7)$$

Numerical constant values are obtained based on measurements so that von Karman's constant κ ≈ 0.4 and the additive constant B ≈ 5.5 (or E ≈ 9.8) on smooth walls; increased surface roughness can reduce the value of B.

Values κ and B are universal constants that are valid for all turbulent flows through smooth walls at high Reynolds numbers. Because of the logarithmic relationship between u^+ and y^+, the formula (3.18) is often called the log-law, and the layer where y^+ takes values between 30 and 500 log-law layers.

Experimental measurements show that the log-law is valid in the region of $0.02 < y/\delta <$ 0.2. For larger values of y, the velocity-defect law (3.17) gives the correct form. In overlapping territories, the log law and velocity law must be the same. a suitable overlap is obtained by assuming the following logarithmic form

$$\frac{U_{max} - U}{u_\tau} = -\frac{1}{\kappa} ln\left(\frac{y}{\delta}\right) + A$$

where A is a constant. This velocity-defect law is often called the law of wake.

Figure 3.11 from Schlichting (1979) shows the nearby agreement between theoretical conditions (3.18) and (3.19) in their zones of legitimacy and experiment data.

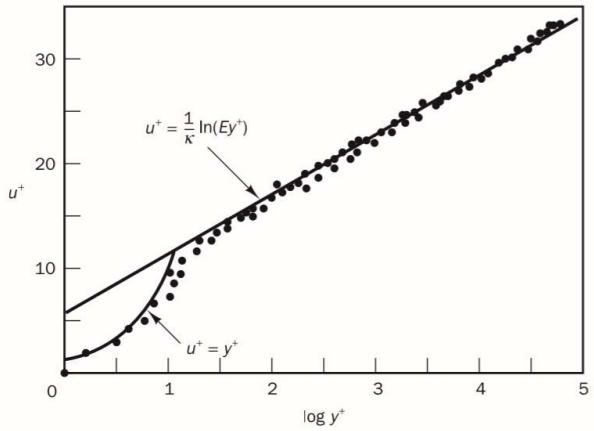

Figure 2.19 Velocity Distribution near a solid wall (H K Versteeg and W Malalasekera, 2005)

Turbulent boundary layers adjacent to solid surfaces consist of two regions:

- Inner area: 10-20% of the total thickness of the wall layer; shear stress is (almost) constant and equal to wall shear stress τ w. In this region there are three zones. In order to increase the distance from the wall, we have: - linear sub-layers: viscous stresses dominate flow adjacent to the surface - buffer layers: viscous and turbulent stresses have similar strengths - log-law layers: turbulent (Reynolds) stress dominates.
- Outer region or law-of-the-wake layer: core flow dominated by inertia away from the wall, free of direct viscous effects.

2.8 References

Adamovsky, D., Neuberger, P., & Adamovsky, R. (2015). Changes in energy and temperature in the ground mass with horizontal heat exchangers - The energy source for heat pumps. *Energy and Buildings*, *92*, 107–115. https://doi.org/10.1016/j.enbuild.2015.01.052

Alam, T., & Kim, M. H. (2018). A comprehensive review on single phase heat transfer enhancement techniques in heat exchanger applications. *Renewable and Sustainable Energy Reviews*, *81*(August 2017), 813–839.

https://doi.org/10.1016/j.rser.2017.08.060

Bozzoli, F., Cattani, L., & Rainieri, S. (2016). Effect of wall corrugation on local convective heat transfer in coiled tubes. *International Journal of Heat and Mass Transfer*, *101*, 76–90. https://doi.org/10.1016/j.ijheatmasstransfer.2016.04.106

Carslaw, H. S., & Jaeger, J. C. (1946). *Conduction of Heat in Solids*. Oxford UK: Claremore Press.

Chokphoemphun, S., Pimsarn, M., Thianpong, C., & Promvonge, P. (2015). Thermal performance of tubular heat exchanger with multiple twisted-tape inserts. *Chinese Journal of Chemical Engineering*, *23*(5), 755–762. https://doi.org/10.1016/j.cjche.2015.01.003

D.A. Ball, R.D. Fischer, D. L. H. (1983). Design methods for ground-source heat pumps. *The 1983 Annual Meeting of the American Society of Heating, Refrigerating and Air-Conditioning Engineers*, 416–440. Atlanta: ASHRAE.

D.J. McConalogue, R. S. S. (1968). Motion of fluid in a curved tube. *Proc. Roy. Soc. London A*, 37–53.

Dean, W. R. (1927). Note on the motion of fluid in a curved pipe. *The London, Edinburgh, and Dublin Philosophical Magazine and Journal of Science*, *4*, 208-223.

Dean, W. R. (1928). The stream-line motion of fluid in a curved pipe. *The London, Edinburgh, and Dublin Philosophical Magazine and Journal of Science*, *5*, 673–695.

Dehghan, B., Sisman, A., & Aydin, M. (2016). Parametric investigation of helical ground heat exchangers for heat pump applications. *Energy and Buildings*, *127*, 999–1007. https://doi.org/10.1016/j.enbuild.2016.06.064

Dennis, S. C. R., & NG, M. (1982). Dual solutions for steady laminar flow through a curved tube. *Quarterly Journal of Mechanics and Applied Mathematics*, *35*(3), 305–324. https://doi.org/10.1093/qjmam/35.3.305

E.W. Heinonen, R.E. Tapscott, M.W. Wildin, A. N. B. (1996). *Assessment of anti-freeze solutions for ground-source heat pump systems*.

Eiamsa-ard, S., Thianpong, C., & Eiamsa-ard, P. (2010). Turbulent heat transfer enhancement by counter/co-swirling flow in a tube fitted with twin twisted tapes. *Experimental Thermal and Fluid Science*, *34*(1), 53–62. https://doi.org/10.1016/j.expthermflusci.2009.09.002

Eskilson, P. (1987). *Thermal analysis of heat extraction boreholes*. University of Lund.

Florides, G., & Kalogirou, S. (2007). Ground heat exchangers-A review of systems, models and applications. *Renewable Energy*, *32*(15), 2461–2478. https://doi.org/10.1016/j.renene.2006.12.014

H.Y. Zeng, N.R. Diao, Z. H. F. (2003). Efficiency of vertical geothermal heat exchangers in ground source heat pump systems. *International Journal of Thermal Sciences*, 77–81.

H K Versteeg and W Malalasekera. (2005). An Introduction to Computational Fluid Dynamics. In *Pearson Education Limited* (Vol. 6). https://doi.org/10.1109/mcc.1998.736434

Hellstrom, G. (1991). *Ground Heat Storage: Thermal Analyses of Duct Storage Systems*. University of Lund.

I. Sarbu, C. S. (2010a). General review of ground-source heat pump systems for heating and cooling of buildings. *WSEAS Transaction on Heat and Mass Transfer*, 31–40.

I. Sarbu, C. S. (2010b). *Heat Pumps*. Timisoara: Politehnica Publishing House.

Ishigaki, H. (1993). Fundamental characteristics of laminar flows in a rotating curved pipe. *Trans. JSME B*, 1494–1501.

Ishigaki, H. (1996). Laminar flow in rotating curved pipes. *J. Fluid Mech.*, 373–388.

Ishigaki, H. (1999). Laminar convective heat transfer in rotating curved pipes. *JSME Int. J. Ser. B*, 489–497.

Ito, H. (1987). Flow in curved pipes. *JSME Int. J.*, 543–552.

J.E. Bose, J.D. Parker, F. C. M. (1985). *Design/data Manual for Closed-loop Ground-coupled Heat pump Systems*. Oklahoma State Univ for ASHRAE.

J.E. Bose, M.D. Smith, J. D. S. (2002). Advances in ground source heat pump systems—an international overview. *Proceedings of the 7th Int. Conference on Energy Agency Heat Pump*, 313–324. Beijing.

J.W. Thornton, T.P. McDowell, J.A. Shonder, P.J. Hughes, D. Pahud, G. H. (1997). Residential vertical geothermal heat pump system models: calibration to data. *ASHRAE Transactions*, 660–674.

Jalaluddin, & Miyara, A. (2015). Thermal performance and pressure drop of spiral-tube ground heat exchangers for ground-source heat pump. *Applied Thermal Engineering*, *90*, 630–637. https://doi.org/10.1016/j.applthermaleng.2015.07.035

Kao, H. C. (1992). Some aspects of bifurcation structure of laminar flow in curved ducts. *J. Fluid Mech.*, 519–539.

Kavanaugh, S.P. and Rafferty, K. (1997). *Ground-Source Heat Pumps, Design of*

Geothermal Systems for Commercial and Institutional Buildings. Atlanta: ASHRAE.

L.R. Ingersoll, O.J. Zobel, A. C. I. (1954). *Heat Conduction with Engineering Geological, and other Applications*. New York: McGraw-Hill.

L.S. Yao, S. A. B. (1975). Entry flow in a curved pipe. *J. Fluid Mech.*

Li, X. wei, Meng, J. an, & Guo, Z. yuan. (2009). Turbulent flow and heat transfer in discrete double inclined ribs tube. *International Journal of Heat and Mass Transfer*, *52*(3–4), 962–970. https://doi.org/10.1016/j.ijheatmasstransfer.2008.07.027

Li, X. wei, Yan, H., Meng, J. an, & Li, Z. xin. (2007). Visualization of longitudinal vortex flow in an enhanced heat transfer tube. *Experimental Thermal and Fluid Science*, *31*(6), 601–608. https://doi.org/10.1016/j.expthermflusci.2006.06.007

Liu, S., & Sakr, M. (2013). A comprehensive review on passive heat transfer enhancements in pipe exchangers. *Renewable and Sustainable Energy Reviews*, *19*, 64–81. https://doi.org/10.1016/j.rser.2012.11.021

Luo, J., Rohn, J., Bayer, M., & Priess, A. (2013). Modeling and experiments on energy loss in horizontal connecting pipe of vertical ground source heat pump system. *Applied Thermal Engineering*, *61*(2), 55–64. https://doi.org/10.1016/j.applthermaleng.2013.07.022

Meng, J. A., Liang, X. G., Chen, Z. J., & Li, Z. X. (2005). Experimental study on convective heat transfer in alternating elliptical axis tubes. *Experimental Thermal and Fluid Science*, *29*(4), 457–465. https://doi.org/10.1016/j.expthermflusci.2004.04.006

N.K. Muraya, D.L. O'Neal, W. M. H. (1996). Thermal interference of adjacent legs in a vertical U-tube heat exchanger for a ground-coupled heat pump. *ASHRAE Transactions*, 12–21.

Nobari, M. R. H., & Gharali, K. (2006). A numerical study of flow and heat transfer in internally finned rotating straight pipes and stationary curved pipes. *International Journal of Heat and Mass Transfer*, *49*(5–6), 1185–1194. https://doi.org/10.1016/j.ijheatmasstransfer.2005.06.042

Pahud, D., & Matthey, B. (2001). Comparison of the thermal performance of double U-pipe borehole heat exchangers measured in situ. *Energy and Buildings*, *33*(5), 503–507. https://doi.org/10.1016/S0378-7788(00)00106-7

Rainieri, S., Bozzoli, F., Cattani, L., & Pagliarini, G. (2012). Experimental investigation

on the convective heat transfer enhancement for highly viscous fluids in helical coiled corrugated tubes. *Journal of Physics: Conference Series*, *395*(1). https://doi.org/10.1088/1742-6596/395/1/012032

Rainieri, S., Bozzoli, F., Cattani, L., & Pagliarini, G. (2013). Compound convective heat transfer enhancement in helically coiled wall corrugated tubes. *International Journal of Heat and Mass Transfer*, *59*(1), 353–362. https://doi.org/10.1016/j.ijheatmasstransfer.2012.12.037

Sarbu, I., & Sebarchievici, C. (2014). General review of ground-source heat pump systems for heating and cooling of buildings. *Energy and Buildings*, *70*, 441–454. https://doi.org/10.1016/j.enbuild.2013.11.068

W.M. Collins, S. C. R. D. (1975). The steady motion of a viscous fluid in a curved tube. *Q. J. Mech. Appl. Math.*

W.Y. Soh, S. A. B. (1984). Laminar entrance flow in a curved pipe. *J. Fluid Mech.*, 109–135.

Y. Gu, D. L. O. (1998). Development of an equivalent diameter expression for vertical U-tubes used in ground-coupled heat pumps. *ASHRAE Transactions*, 347–355.

Yang, W., Lu, P., & Chen, Y. (2016). Laboratory investigations of the thermal performance of an energy pile with spiral coil ground heat exchanger. *Energy and Buildings*, *128*, 491–502. https://doi.org/10.1016/j.enbuild.2016.07.012

Zarrella, A., Emmi, G., & De Carli, M. (2017). A simulation-based analysis of variable flow pumping in ground source heat pump systems with different types of borehole heat exchangers: A case study. *Energy Conversion and Management*, *131*, 135–150. https://doi.org/10.1016/j.enconman.2016.10.061

Zheng, N., Liu, P., Shan, F., Liu, Z., & Liu, W. (2016a). Effects of rib arrangements on the flow pattern and heat transfer in an internally ribbed heat exchanger tube. *International Journal of Thermal Sciences*, *101*, 93–105. https://doi.org/10.1016/j.ijthermalsci.2015.10.035

Zheng, N., Liu, P., Shan, F., Liu, Z., & Liu, W. (2016b). Numerical investigations of the thermal-hydraulic performance in a rib-grooved heat exchanger tube based on entropy generation analysis. *Applied Thermal Engineering*, *99*, 1071–1085. https://doi.org/10.1016/j.applthermaleng.2016.02.008

Zheng, N., Liu, P., Shan, F., Liu, Z., & Liu, W. (2017). Turbulent flow and heat transfer enhancement in a heat exchanger tube fitted with novel discrete inclined grooves. *International Journal of Thermal Sciences*, *111*, 289–300.

https://doi.org/10.1016/j.ijthermalsci.2016.09.010

Zheng, N., Liu, W., Liu, Z., Liu, P., & Shan, F. (2015). A numerical study on heat transfer enhancement and the flow structure in a heat exchanger tube with discrete double inclined ribs. *Applied Thermal Engineering*, *90*, 232–241. https://doi.org/10.1016/j.applthermaleng.2015.07.009

Zheng, N., Yan, F., Zhang, K., Zhou, T., & Sun, Z. (2020). A review on single-phase convective heat transfer enhancement based on multi-longitudinal vortices in heat exchanger tubes. *Applied Thermal Engineering*, *164*(May 2019), 114475. https://doi.org/10.1016/j.applthermaleng.2019.114475

CHAPTER

3

CONSIDERATION OF DISCRETE DOUBLE INCLINED RIBS IN LOW CURVATURE COIL FOR GSHP SYSTEM

3.1 Introduction

The increase in global warming has triggered a rise in the use of renewable energy sources. The Ground Source Heat Pump (GSHP) system is a technology which utilizes renewable energy. This system can improve the efficiency of cooling and heating in commercial buildings. GSHP is connected to Ground Heat Exchanger (GHE) with vertical or horizontal configurations. GHE is used to reject heat to the ground or to absorb heat from the ground. Vertical configurations are usually installed at depths from 15 to 150 m while horizontal configuration can be installed in trenches with depths from 1 to 2 m.

One of GHE horizontal configuration is slinky. The slinky GHE has better thermal performance compared to straight pipes (Adamovsky et al., 2015; Congedo et al., 2012; Wu et al., 2010). The slinky pipe curvature is capable of producing secondary flow resulting from centrifugal force. The amount of research on slinky-coil GHE is not as much as research on GHE straight pipes. The use of two GHE slinky-coil sets in a long time and the number of different loop angles compared to the heat transfer capability has been investigated by (Fujii, et al., 2012). However, the complexity of the slinky-coil, mathematical models have never been used to predict the performance of

slinky GHE in a long time.

Several developments were made to improve the slinky performance of GHE. These include the vertical and horizontal configurations while geometry-based variations on coil pitch distance, coil diameter, tube diameter, tube material, the length between slinky and ground composition. Chong et al. (2014) researched the effect of slinky performance on numerical vertical and horizontal configurations. The results of this study indicate that both configurations produce differences in thermal performance with a maximum of less than 5%.

Ali et al. (2017) researched slinky in experimental vertical and horizontal configurations. They stated that vertical configuration tends to perform more superior than horizontal configuration on the heat extraction rate. Selamat et al. (2015) observed the effect of the number of loops, tube material, and the distance between loops. They stated that the operation of the double and triple loops produced higher thermal performance 83% and 162%, respectively, compared to one loop at the same pump power. The use of copper pipes results in an average heat transfer increase of 48% compared to HDPE pipes. In parallel operations, thermal performance can increase from 10% to 14% when there were distances between loops available. Mostly slinky GHE is low curvature coil. Hardik et al. (2015) researched several curvatures of the coil. They concluded that large curvature has high heat transfer. Strong secondary flow contributes to high heat transfer.

Some researchers observed the flow pattern of the coil pipe. Some articles depict hydrodynamic characters such as velocity fields, secondary flow, and pressure drop in theory (Acrawal et al., 1993; Dean, 1927, 1928), experiments (Austin and Seader, 1974; Saffari et al., 2014), or numeric (Agrawal and Nigam, 2001; Dennis and NG, 1982). Some process parameters are examined with several different boundary conditions, such as constant heat flux, constant temperature, or convection heat transfer (Prabhanjan et al., 2004; Salimpour, 2009).

Wang and Sundén (2004) studied the heat transfer and flow of fluid in a square channel with broken V-shape ribs using the LCT and PIV techniques. They concluded that broken ribs had better performance at high Reynolds numbers. Meng et al. (2005) found that the use of the discrete double inclined rib tube (DDIR-tube) generates multiple vortexes on the laminar flow so that heat transfer increases. Li et al. (2007) inject ink to see flow patterns inside the DDIR-tube. Tang and Zhu (2013) observed the flow structure and heat transfer in the rectangular pipe with the addition of discrete rib

arrays using numerical simulations and experiments. Kathait and Patil (2014) conducted experiments on heat transfer and friction factors of a corrugated tube with gaps. Zheng et al. (2015)investigated DDIR-tube effect of three pairs of v-type ribs by using numerical simulation. They concluded that ribs could produce three pairs of counter-rotating vortex and mainstream flow divided into six helical streams. This flow makes the intense turbulent mixing between the wall and the core of the flow.

As far as the author's knowledge, no research has been carried out in the modeling of modified coil pipe shapes to improve GHE performance. The purpose of our study is to overcome low curvature coil by adding DDIR on the coil wall. This research is to clarify the impact of DDIR use on improving the performance of heat transfer and fluid flow for ground-source heat pump system applications.

3.2 Simulation of DDIR in Low Curvature Coil

3.2.1 Model Description

As shown in Figure 3. 1 (a)-(d), the tube is divided into three parts, namely the entrance, ribbed coil, and exit region. Entrance and exit regions have a length (l) of 200 mm while the axial length of the ribbed coil section is 3.53 m. The inner diameter of the tube (d) is 14.46 mm, tube thickness is 0.71 mm, coil pitch (P) is 100 mm, coil diameter (D) is 900 mm (curvature of coil 2.22 m^{-1}), the double discrete inclined ribs details are ribs pitch (p), then number of circumference of ribs was 4, inclination angle of ribs is (α). three values height of ribs RHC1, RHC2 and RHC3, were used to investigate on thermo-hydraulic performance on coil ribbed tube. Coil plain tube (PC) was used to see improved performance of the DDIR. The details description of geometry can be seen in table 3.1.

Table 3.1. Details Geometry of Heat Exchanger Models

Model	Ribs Height (mm)	Ribs Angle (°)	Ribs Pitch (mm)	Curvature Coil (m^{-1})
RHC1	0.45	45	22	2.22
RHC2	0.75	45	22	2.22
RHC3	1	45	22	2.22
PC	-	-	-	2.22

3.2.2 Numerical Methods

Numerical simulations were carried out by utilizing commercial CFD software, ANSYS FLUENT 17.2, to examine the ribbed coil The governing equations of flow and heat transfer inside the tube are as follows (ANSYS Academic Research, 2017):

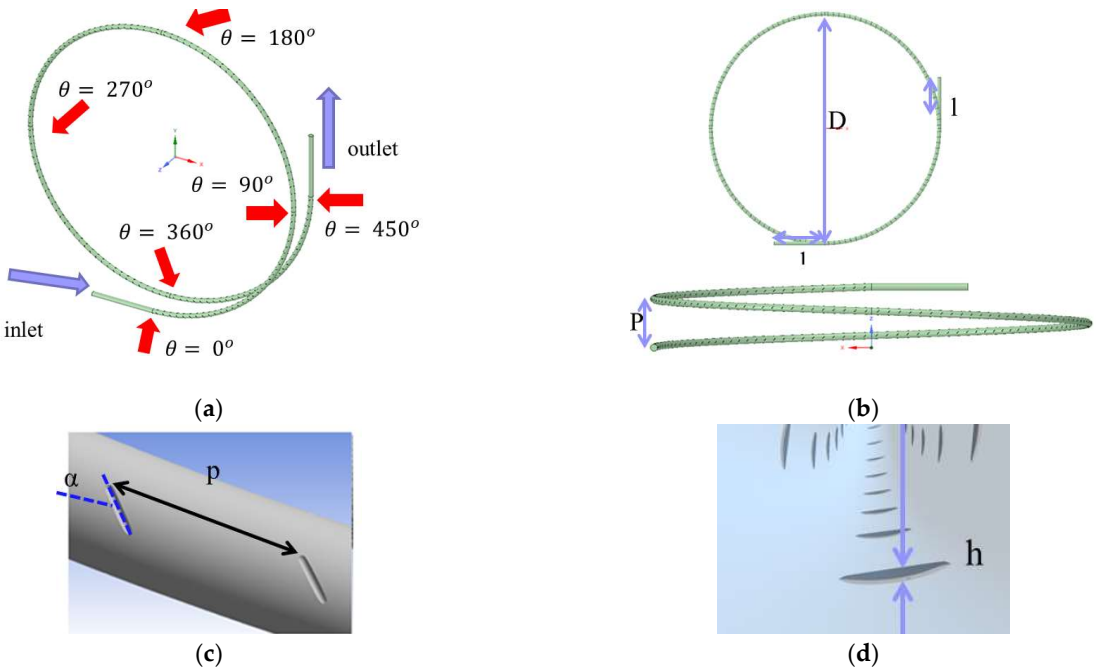

Figure 3. 1. (a) General view of computational domain and several cross sections of coil for data collection; (b) view from top and side; (c) Location of ribs outside view; (d) Location of ribs inside

Continuity Equation:

$$\frac{\partial(\rho \mathrm{u}_i)}{\partial x_i}=0 \tag{3.1}$$

Momentum Equation:

$$\frac{\partial(\rho \mathrm{u}_i)}{\partial t}+\frac{\partial(\rho \mathrm{u}_i \mathrm{u}_j)}{\partial x_j}=-\frac{\partial p}{\partial x_i}+\frac{\partial}{\partial x_j}\left(\mu\frac{\partial(\mathrm{u}_i)}{\partial x_j}-\rho\overline{u_i' u_j'}\right) \tag{3.2}$$

Energy Equation:

$$\frac{\partial(\rho T)}{\partial x_i}+\frac{\partial(\rho \mathrm{u}_i T)}{\partial x_i}=\frac{\partial}{\partial x_i}\left(\frac{\lambda}{c_p}\frac{\partial T}{\partial x_i}\right) \tag{3.3}$$

Turbulence Kinetic Energy Equation:

$$\frac{\partial(\rho T)}{\partial x_i}+\frac{\partial(\rho \mathrm{u}_i T)}{\partial x_i}=\frac{\partial}{\partial x_i}\left(\frac{\lambda}{c_p}\frac{\partial T}{\partial x_i}\right) \tag{3.4}$$

Specific dissipation rate equation:

$$\begin{aligned}\frac{\partial(\rho\omega)}{\partial t}+\frac{\partial(\rho u_i\omega)}{\partial x_i} &= \varphi\rho S^2-\beta\rho\omega^2+\frac{\partial}{\partial x_i}\left((\mu+\sigma_\omega u_t)\frac{\partial\omega}{\partial x_i}\right)\\ &+2(1-F_1)\rho\sigma_{\omega^2}\frac{1}{\omega}\frac{\partial\kappa}{\partial x_i}\frac{\partial\omega}{\partial x_i}\end{aligned} \tag{3.5}$$

Where ρ, T, λ and c_p are density, temperature, thermal conductivity, and heat capacity specific, respectively.

The boundary conditions used in this simulation are as follows. On the inlet side, uniform velocity is used, while the outflow boundary condition is used on the outlet side. Assumption of non-slip and uniform wall temperature conditions on the wall and ribs are used. Water is selected as a working fluid. All simulations use the steady flow approach with Reynolds numbers from 6172 to 10288. The SIMPLE algorithm is used for velocity-pressure coupling. Discretization of the governing equation utilizes the second-order upwind scheme. The minimum convergence criterion was 10^{-3} for continuity, velocity and turbulence equations and 10^{-7} for energy equation.

3.2.3 Data Reduction

Based on the simulation results of velocity and temperature filed, the average heat transfer coefficient can be determined by applying logarithmic mean temperature difference (LMTD) on heat transfer rate where:

$$Q=\dot{m}c_p(T_o-T_i) \tag{3.6}$$

$$h=\frac{Q}{\int_A dA\,\Delta T_m} \tag{3.7}$$

Where LMTD can be written as follows

$$\Delta T_m = \frac{(T_w - T_o) - (T_w - T_i)}{\ln\left(\frac{T_w - T_o}{T_w - T_i}\right)} \tag{3.8}$$

Where m, T_o, T_i, T_w and C_p are is mass flowrate, the bulk temperature at upstream, downstream and wall of the coil, and specific heat capacity, respectively. The use of LMTD is valid because based on the assumption, the property value of the working fluid is constant. Wall temperature is set as same as ground Temperature on our previous research (Ali et al., 2017).

Reynolds number, Nusselt number, friction factors are determined as follows:

$$\mathrm{Re} = \frac{\rho u d}{\mu} \tag{3.8}$$

$$Nu = \frac{hD}{\lambda} \tag{3.10}$$

$$f = \frac{\Delta p}{(l/d)\left(\rho \frac{v^2}{2}\right)} \tag{3.11}$$

Where μ, h, and l are dynamics viscosity, heat transfer coefficient, axial length tube.

Ito's Critical Reynolds number is used to calculate the transition from laminar to turbulent flow (Ito, 1959).

$$\mathrm{Re}_{cr} = 20000\left(\frac{d}{D}\right)^{0.32} \tag{3.12}$$

To know the improvement of the system, we consider about effect pressure drop and heat exchanger rate on net coefficient of performance, COP_{net_heat}, of ground source heat pump system in heating mode.

$$COP_{net\_heat} = \frac{Q_H}{L_{comp} + L_{pump}} = \frac{Q_C + L_{comp}}{L_{comp} + L_{pump}} \tag{3.13}$$

Where, Q_H and Q_C are cooling and heating rate, L_{comp} and L_{pump} are power input to compressor and pump, respectively. If DDIR-coil increase the cooling rate by Q_C' and

pumping power by L'_{pump}, the net heating COP becomes

$$COP'_{net\_heat} = \frac{COP_{net\_heat} + Q'_C/(L_{comp} + L_{pump})}{1 + L'_{pump}/(L_{comp} + L_{pump})} \quad (3.14)$$

It is assumed that L_{comp} is kept constant.

By considering condition of $COP_{net\_heat} < COP'_{net\_heat}$, then the following equations is obtained

$$COP_{net\_heat} < \frac{COP_{net\_heat} + Q'_C/(L_{comp} + L_{pump})}{1 + L'_{pump}/(L_{comp} + L_{pump})} \quad (3.15)$$

From pervious equation, improvement of COP is given as

$$Q'_C > L'_{pump} \quad (3.16)$$

The pumping power is expressed as product of volumetric flowrate, V (m^3/s) and pressure loss, Δp (Pa).

$$L_{pump} = V\,\Delta p, L'_{pump} = V\,\Delta p' \quad (3.17)$$

From equation 3.15 and 3.16, the following equation is obtained

$$\frac{Q'_C}{Q_C} - \frac{V\,\Delta p}{Q_C}\frac{\Delta p'}{\Delta p} > 0 \quad (3.18)$$

Where Q_C, Q'_C, V, Δp, and $\Delta p'$, are cooling rate (W/m), an increase of cooling rate (W/m), volumetric flow rate (m^3/s), pressure drop loss (Pa), and increase of pressure loss (Pa), respectively.

DDIR of the coil is evaluated by the Coefficient of Performance (COP) improvement factor in heating mode in Eq 3.18. If left term of equation 3.18 is bigger than zero, it means there is enhancement performance of the GSHP system. All the COP improvement factors are evaluated based on heat transfer and fluid flow of straight tube by using Nusselt number and friction factor in a smooth straight tube.

3.2.4 Mesh Independence Test

Ansys Meshing 17.2 is used to produce three-dimensional meshing. Fluid domains are discretized using unstructured mesh elements. The mesh distance near the tube and ribs wall is calculated based on $y^+ = 1$ to produce a more accurate result.

Table 3.2. Grid Independence Test

GHE Type	Coarse	Medium	Fine+
DDIR Coil (Number of Elements)	18168327	181645194	19008154
Pressure Drop (Pa/m)	589.471	592.568	592.929
Relative Deviation	0.077%	0.060%	-
Heat Transfer Coefficient (W/(m^2K))	3172.4	3169.6	3172.15
Relative Deviation	0.007 %	0.080%	-

+ Fine mesh results are selected as the base of relative deviation

3.3 Result and Discussion

To give a good explanation of the thermo-hydraulic effect DDIR on coil tube, we investigate temperature and velocity contour, circumferential heat flux, and vortex intensity.

3.3.1 Model Validation

The simulation results were compared with the Gnielinski correlation for the Nusselt number and Petukhov correlation for friction factors in the turbulent flow through smooth pipe to verify the accuracy of the numerical simulation procedures applied in this research. Figure 3.2 illustrates the comparison between simulation results and correlation. The simulation results confirm the correlations within 1% and 7.6% for friction factor and Nusselt number, respectively.

3.3.2 Fluid Flow Characteristics

In this analysis, cold water at 280 K with a Re = 8230 enters the helical pipe with a predetermined boundary condition. The working fluid is made to heat up when it flows along with the coil with a wall temperature of 291 K. The critical Re in the coil is 5332. The turbulent intensity is calculated based on the empirical correlation for pipe flows as follows (ANSYS Academic Research, 2017).

$$I = 0.16\left(\mathrm{Re}_{D_H}\right)^{-1/8} \tag{15}$$

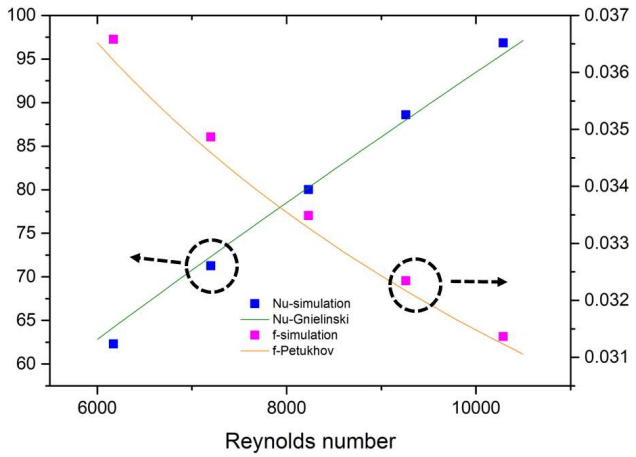

Figure 3.2 Validation of smooth tube friction factor and Nusselt number.

Figure 3.3 shows the evolution of velocity contour in several axial positions along the length of the coil (every 90º, i.e., ¼ turns) from 0º to 450º. The details of geometry modification is described in table 3.1. It can be seen that both PC and RHC2 have reached fully developed flow at first θ = 90º, the further velocity contours keep a constant shape. Both tubes also indicate the high velocity shifted from the center of the tube at θ= 0º to outside of the coil. This phenomenon is caused by the secondary flow of the coil. However, the velocity magnitude contour of the ribbed tube is somewhat distorted. It may be caused by flow by the ribs.

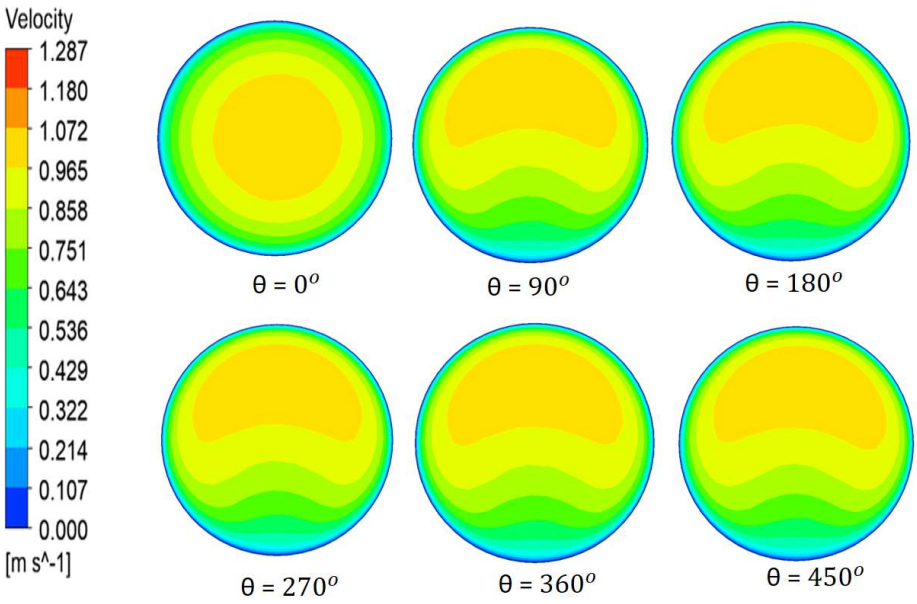

(a)

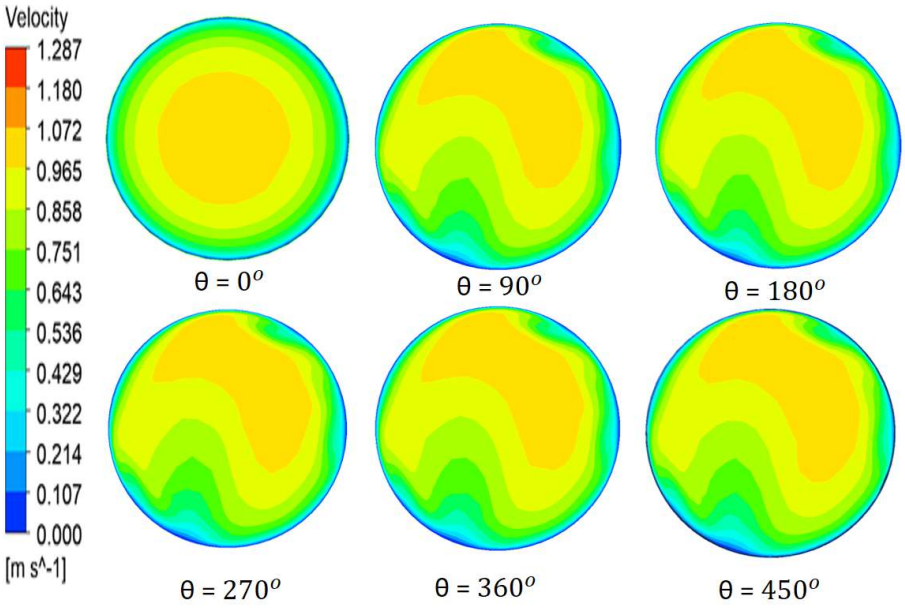

(b)

Figure 3.3 Evolution of velocity contour along the axial length of the coil at Re = 8230, top and downside of the tube are outer side and inner side of the coil (a) PC; (b) RHC

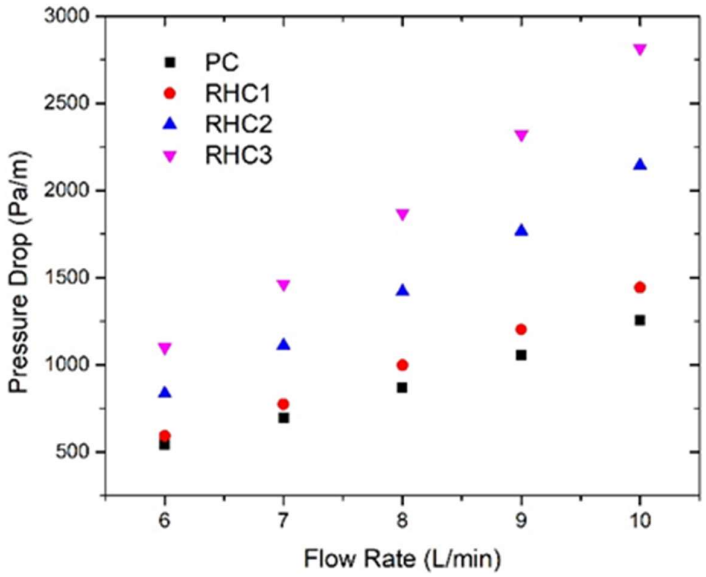

Figure 3.4. Comparison of pressure drop in different configuration of ribs.

Figure 3.4 shows the effect DDIR on pressure drop at various flow rates. An apparent trend is found where pressure drop increases with the increase of ribs height. PC and RHC1 have similar pressure drop values, especially at a low flow rate when compared to RHC2 and RHC3. The RHC2 and RHC3 suffer more pressure drop than

that of PC. Higher flow rate effect could be more domination in this phenomenon, although the higher flowrate leads to smaller friction factors in all tubes. The pressure drop could be triggered by ribs generated flow generated. The maximum frictional pressure drop of RHC3 is about 124% greater than that of PC at $\dot{V}$= 10 L/m.

3.3.3 Heat Transfer Characteristics

The thermal performance of DDIR in the coil was studied concerning heat transfer rate and temperature distribution within several cross-sections of the tube. Figure 3.5 shows the effect of flow rate on the heat transfer rate for PC and RHC. It can be seen that heat transfer rate almost linearly increases with an increase in flowrate for curved tube ribs as well as curved tube plain. However, the amplitude of variation of all variation of RHC is more significant than that of for PC, which can attribute to the better mixing caused by longitudinal swirls flow in the ribs. The highest heat transfer rate is obtained by RHC3, which relatively larger about 27 % greater than that of PC at $\dot{V}$= 10 L/m.

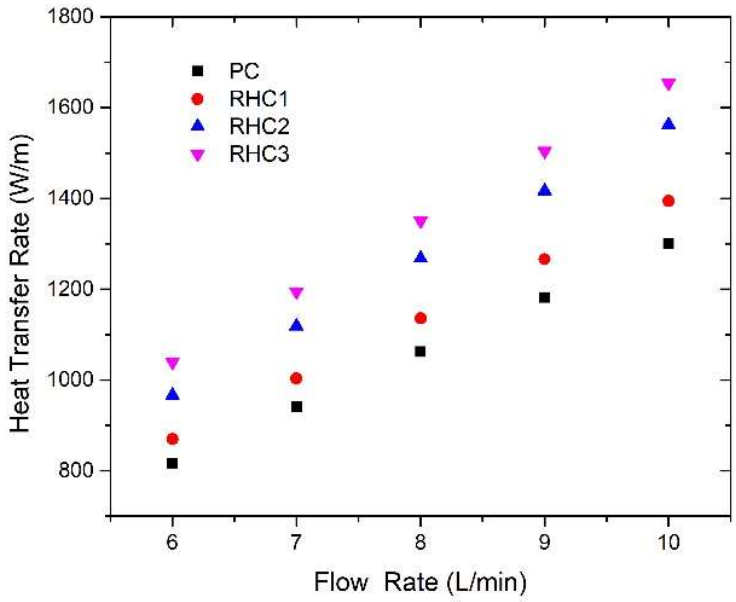

Figure 3.5. Comparison of heat transfer rate in different configuration of ribs.

Figure 3.6, It can be seen that longer axial distance or more significant coil angle tend to have more uniformity temperature profile. The colder fluid in the core of the tube at θ= 0° tends to move to the outer side of the coil at θ= 90° on both tubes by

increasing coil angle. However, the temperature profile of the ribbed tube is somewhat distorted. The temperature profile of curved tube ribs looks hotter compared to the curved tube plain at the same position above θ= 90°. It could be caused by thermal mixing of flow generated by the ribs.

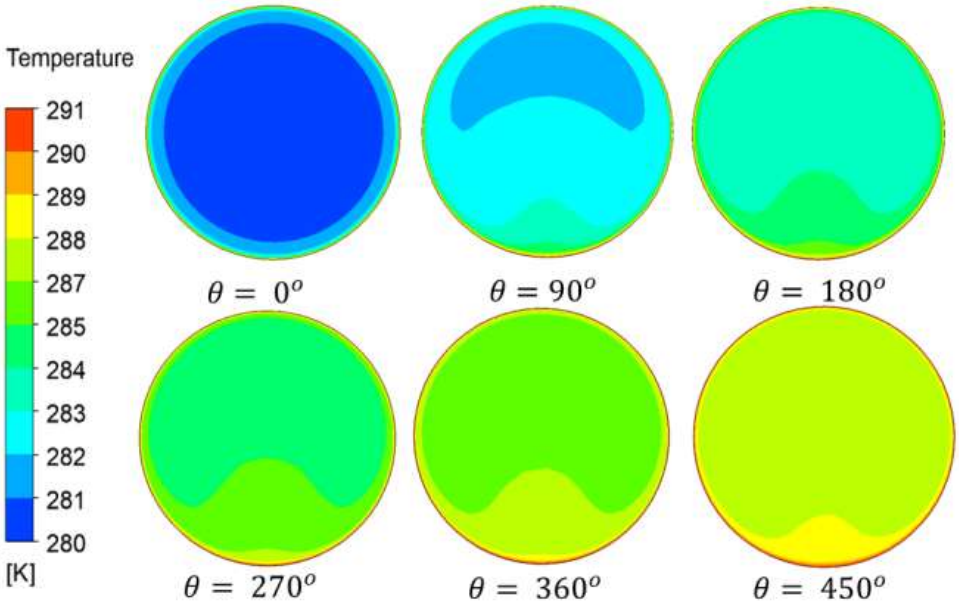

(a)

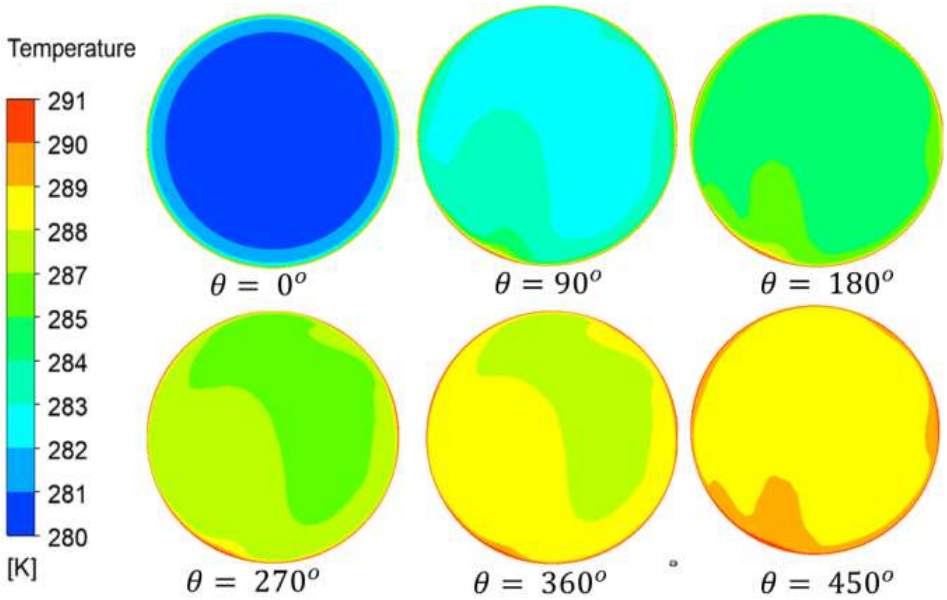

(b)

Figure 3.6. Evolution of temperature contour along axial length of the coil at Re = 8230, top and downside of the tube are outside and inner side of coil (a) PC; (b) RHC2.

3.3.4 Wall Heat Flux

Figure 3.7 shows the circumferential distribution (β) of heat flux surfaces calculated from the local wall temperature, local bulk temperature, and fluid-side local heat transfer coefficient. The overview of this distribution of Figure 3.8(a) is following Hardik et al. (2015) and Xin and Ebadian (1997) studies on the plain coil. Surface heat fluxes have varying sinusoidal values in the circumferential direction. Heat flux distribution is a mirror of the temperature difference distribution between the wall and fluid near the wall. Therefore, a small difference from the difference in temperature between fluids near walls and walls can result in significant changes to the surface heat flux. On the outside and inside of the coil, the surface of the heat flux is sinusoidal. Surface heat transfer is the maximum value on the outermost side at 0° or 360°, while the minimum value is on the inner side at 180°

.

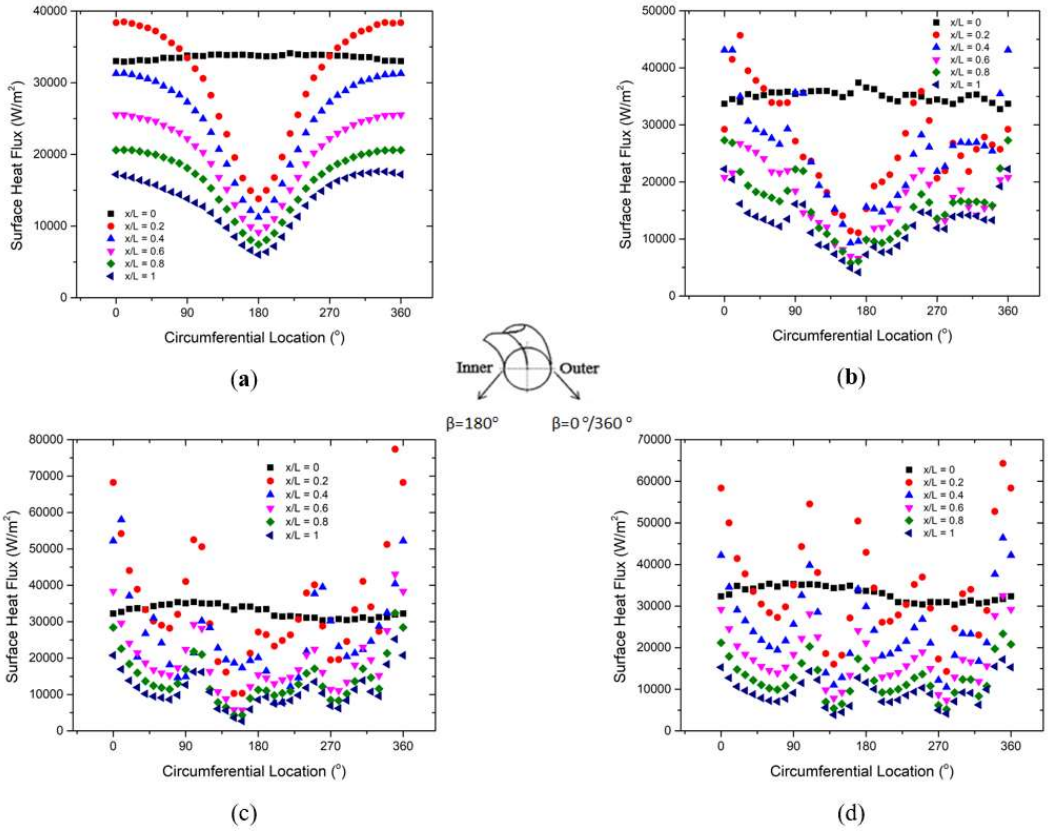

Figure 3.7. Circumferential surface heat flux distribution at different axial point of coil at Re = 8230 (a) PC; (b) RHC1; (c) RHC2; (d) RHC3.

In Figure 3.7 (b)-(d), all RHC variations have higher fluctuation of wall heat flux than that of PC. The higher height of ribs can contribute to the more considerable change of wall heat flux distribution. Generally, the increment of the height of ribs indicates lower wall heat flux at each axial location. At x / L = 1, the average heat flux plain coil has the highest value of 13512 W/m2, while the average heat flux ribs of 1 mm have the lowest value of 9359 W/m^2. This trend shows decrement in heat transfer caused by the bulk temperature approaching wall temperature. It can be seen that there are significantly bottomed out of surface heat fluxes in several circumferential locations. Then, the summary of the majority high and low heat flux locations on the circumferential tube is mentioned as follows. The high heat flux in PC is at 10^o while the low is at 180^o. At RHC1, the high heat flux is at 260-20^o and the low heat flux is at 160-170^o. At RHC2, the high heat flux is at 350^o-10^o, and the low heat flux at 150^o-160^o. At RHC3, the high heat flux is at 350^o, and the low heat flux value is at 280^o. The distribution pattern could be contributed by proper thermal mixing due to the flow generated by the ribs.

3.3.5 Secondary Flow Pattern

Figure 3.8 illustrates the variation of the vortex location for different ribs at the same Reynolds number. Based on Zheng et al. (2015) research, the use of double discrete inclined ribs (DDIR) on straight pipes can generate several vortices. However, in our research, we did not find any additional vortexes in ribs application on low curvature coil. In general view, vortex deflection has increased with increasing size of ribs, streamlined changing from smooth pattern to distorted pattern. The distorted pattern could be resulted by the merge of the main flow and DDIR's induced flow. Based on the above analysis at the same Reynolds number, vortex deflection will increase with increasing height of ribs, and pressure loss will be more significant and more distorted vortex deflection conditions than the smaller ribs. The more distorted vortex could contribute to enhanced heat transfer.

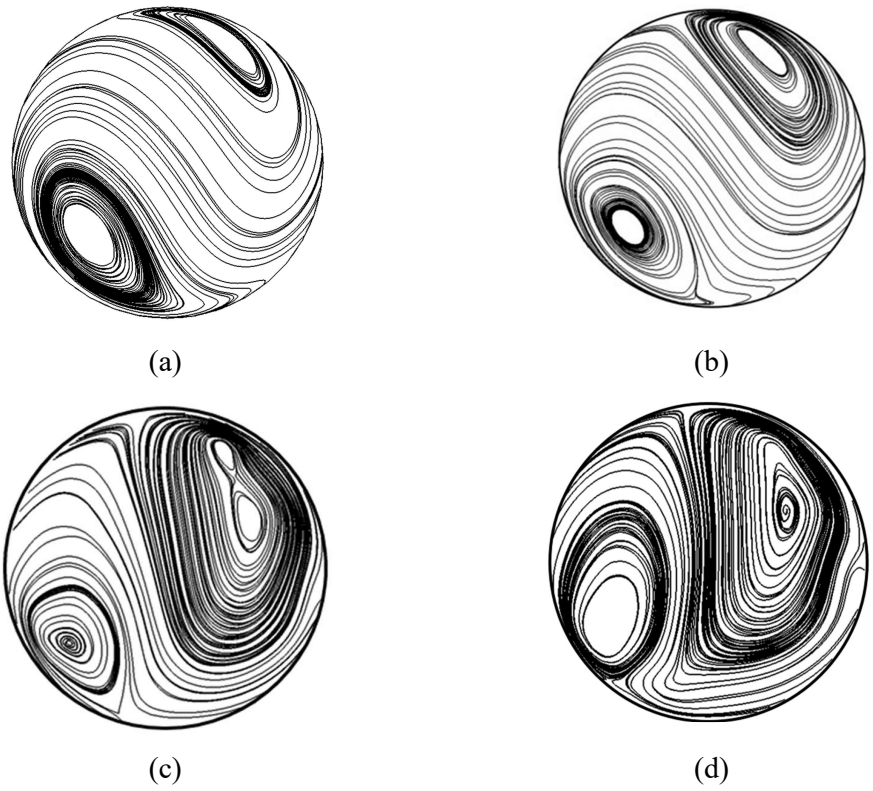

Figure 3.8. Secondary flow in Re = 8230 top and downside of tube are outer side and inner side of coil, respectively (a) PC; (b) RHC1; (c) RHC2; (d) RHC3.

To find out the influence of secondary flow in this study, our research use method, which was proposed by Lin, et al. (2009) and Tang, et al. (2017). They apply absolute vorticity flux intensity to relate improvement of heat transfer and pressure drop on the pipe. The intensity can illustrate the flow field in the coil. This parameter is a crucial factor for secondary flow typical features. It can be described as eq (14)

$$J_{ABS}^{n} = \frac{1}{A}\iint \left|\omega^{n}\right| dA \tag{14}$$

Where A, n, and ω are cross-section area (m^2), the direction of the normal cross-section and vorticity, respectively. Vorticity is a curl of u-velocity in the flow field. The vorticity can be stated as follows

$$\omega = \nabla \times u \tag{15}$$

Figure 3.9 shows changes in absolute vorticity flux. Secondary flow intensity gradually increases with increasing flow rate, which occurs both at curved tube plain and curved tube ribs. RHC1 tend to perform slightly better than the PC on the same

flow rate. What is interesting in this graph is the dramatic increase in vortex intensity in RHC2 and RHC3. This phenomenon could be affected by the significant deviation of secondary flow, as shown in Fig 3.8. The characteristics of absolute vorticity flux could be the reason why pressure drop and heat transfer, in Figure 3.4 and 3.5, PC and RHC1 have almost similar value meanwhile RHC2 and RHC3 tends to have higher pressure drop and heat transfer than PC.

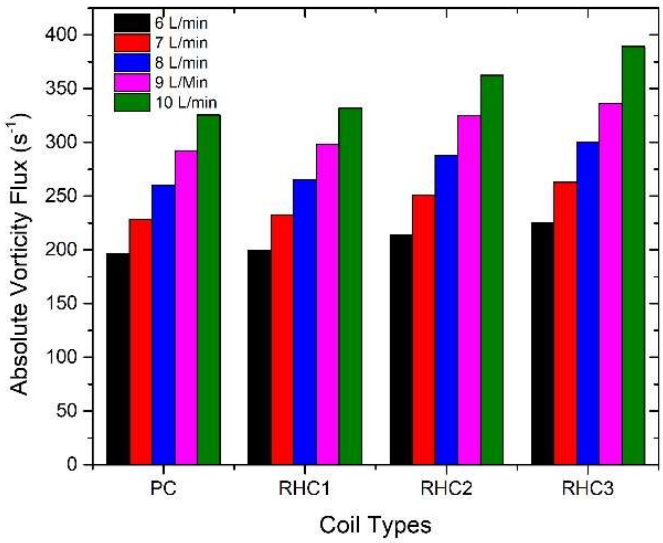

Figure 3.9. Variation of absolute vorticity flux with type of coil and flow rates.

Generally, COP improvement factors, as shown in Figure 3.10 are always positive. The use of higher ribs results in a COP Improvement factor that is very significant compared to the plain coil. However, the increase in flowrate decreases the COP improvement factor slowly. This could be caused by an increase in energy from the use of ribs compensated with energy loss due to pressure drop. The rate of this COP Improvement factor will probably level off at higher flow rate.

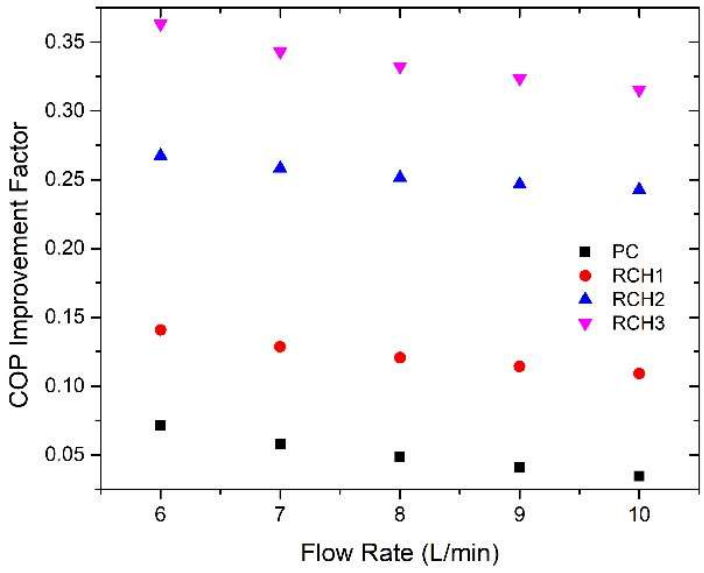

Figure 3.10. Effect of double discrete inclined ribs on COP Improvement factor at various flowrates

3.4 Conclusion

The results of numerical study of heat transfer and pressure drop enhancement in DDIR applied to low curvature coil are described in this paper. Based on the result, the following conclusions are drawn. Pressure drop and heat transfer dependent on ribs height of low curvature coil, Circumferential wall heat flux on PC is varying sinusoidal form. Meanwhile, the heat flux distributions of RHCs tend to fluctuate. Higher ribs contribute higher fluctuation of heat flux. The longer axial distance contributes to the lower heat flux due to the bulk temperature approaching to wall temperature., The usage of higher ribs could contribute a higher deviation vortex than that of PC., The characteristics of pressure drop and heat transfer could be related to the absolute vorticity flux., and the higher ribs can enhance COP improvement factor. Maximum improvement at given flow rate COP is RHC3 eightfold higher than PC. However, increasing flowrate tends to decrease COP Improvement factors.

3.5 References

Acrawal, S., Jayaraman, G., Srivastava, V. K., & Nigamt, K. D. P. (1993). Power law fluids in a circular curved tube. part i. laminar flow. *Polymer-Plastics Technology*

and Engineering, *32*(6), 595–614. https://doi.org/10.1080/03602559308021024

Adamovsky, D., Neuberger, P., & Adamovsky, R. (2015). Changes in energy and temperature in the ground mass with horizontal heat exchangers - The energy source for heat pumps. *Energy and Buildings*, *92*, 107–115. https://doi.org/10.1016/j.enbuild.2015.01.052

Agrawal, S., & Nigam, K. D. P. (2001). Modelling of a coiled tubular chemical reactor. *Chemical Engineering Journal*, *84*(3), 437–444. https://doi.org/10.1016/S1385-8947(00)00370-3

Ali, M. H., Kariya, K., & Miyara, A. (2017). Performance analysis of slinky horizontal ground heat exchangers for a ground source heat pump system. *Resources*, *6*(4), 1–18. https://doi.org/10.3390/resources6040056

ANSYSAcademicResearch. (2017). *Help System-Fluent Theory Guide, ANSYS*.

Austin, L. R., & Seader, J. D. (1974). Entry Region for Steady Viscous Flow in Coiled Circular Pipes. *American Institute of Chemical Engineers*, *20*(4), 820–822.

Chong, C. S. A., Gan, G., Verhoef, A., & Garcia, R. G. (2014). Comparing the thermal performance of horizontal slinky-loop and vertical slinky-loop heat exchangers. *International Journal of Low-Carbon Technologies*, *9*(4), 250–255. https://doi.org/10.1093/ijlct/ctt001

Congedo, P. M., Colangelo, G., & Starace, G. (2012). CFD simulations of horizontal ground heat exchangers: A comparison among different configurations. *Applied Thermal Engineering*, *33–34*(1), 24–32. https://doi.org/10.1016/j.applthermaleng.2011.09.005

Dean, W. R. (1927). Note on the motion of fluid in a curved pipe. *The London, Edinburgh, and Dublin Philosophical Magazine and Journal of Science*, *4*, 208-223.

Dean, W. R. (1928). The stream-line motion of fluid in a curved pipe. *The London, Edinburgh, and Dublin Philosophical Magazine and Journal of Science*, *5*, 673–695.

Dennis, S. C. R., & NG, M. (1982). Dual solutions for steady laminar flow through a curved tube. *Quarterly Journal of Mechanics and Applied Mathematics*, *35*(3), 305–324. https://doi.org/10.1093/qjmam/35.3.305

Fujii, H., Nishi, K., Komaniwa, Y., & Chou, N. (2012). Numerical modeling of slinky-coil horizontal ground heat exchangers. *Geothermics*, *41*, 55–62. https://doi.org/10.1016/j.geothermics.2011.09.002

Hardik, B. K., Baburajan, P. K., & Prabhu, S. V. (2015). Local heat transfer coefficient in helical coils with single phase flow. *International Journal of Heat and Mass Transfer*, *89*, 522–538. https://doi.org/10.1016/j.ijheatmasstransfer.2015.05.069

Ito, H. (1959). Friction factor for turbulent flow in curved tube. *Journal Basic Engineering*, *81*, 123–134.

Jalaluddin, & Miyara, A. (2015). Thermal performance and pressure drop of spiral-tube ground heat exchangers for ground-source heat pump. *Applied Thermal Engineering*, *90*, 630–637. https://doi.org/10.1016/j.applthermaleng.2015.07.035

Kathait, P. S., & Patil, A. K. (2014). Thermo-hydraulic performance of a heat exchanger tube with discrete corrugations. *Applied Thermal Engineering*, *66*(1–2), 162–170. https://doi.org/10.1016/j.applthermaleng.2014.01.069

Li, X. wei, Yan, H., Meng, J. an, & Li, Z. xin. (2007). Visualization of longitudinal vortex flow in an enhanced heat transfer tube. *Experimental Thermal and Fluid Science*, *31*(6), 601–608. https://doi.org/10.1016/j.expthermflusci.2006.06.007

Lin, Z. M., Sun, D. L., & Wang, L. B. (2009). The relationship between absolute vorticity flux along the main flow and convection heat transfer in a tube inserting a twisted tape. *Heat and Mass Transfer*, *45*(11), 1351–1363. https://doi.org/10.1007/s00231-009-0511-z

Meng, J. A., Liang, X. G., & Li, Z. X. (2005). Field synergy optimization and enhanced heat transfer by multi-longitudinal vortexes flow in tube. *International Journal of Heat and Mass Transfer*, *48*(16), 3331–3337. https://doi.org/10.1016/j.ijheatmasstransfer.2005.02.035

Prabhanjan, D. G., Rennie, T. J., & Raghavan, G. S. V. (2004). Natural convection heat transfer from helical coiled tubes. *International Journal of Thermal Sciences*, *43*(4), 359–365. https://doi.org/10.1016/j.ijthermalsci.2003.08.005

Saffari, H., Moosavi, R., Nouri, N. M., & Lin, C. X. (2014). Prediction of hydrodynamic entrance length for single and two-phase flow in helical coils. *Chemical Engineering and Processing: Process Intensification*, *86*, 9–21. https://doi.org/10.1016/j.cep.2014.10.005

Salimpour, M. R. (2009). Heat transfer coefficients of shell and coiled tube heat exchangers. *Experimental Thermal and Fluid Science*, *33*(2), 203–207. https://doi.org/10.1016/j.expthermflusci.2008.07.015

Selamat, S., Miyara, A., & Kariya, K. (2015). Analysis of short time period of operation of horizontal ground heat exchangers. *Resources*, *4*(3), 507–523.

https://doi.org/10.3390/resources4030507

Tang, L., Yuan, S., Malin, M., & Parameswaran, S. (2017). Secondary vortex-based analysis of flow characteristics and pressure drop in helically coiled pipe. *Advances in Mechanical Engineering*, *9*(4), 1–11. https://doi.org/10.1177/1687814017700059

Tang, X. Y., & Zhu, D. S. (2013). Flow structure and heat transfer in a narrow rectangular channel with different discrete rib arrays. *Chemical Engineering and Processing: Process Intensification*, *69*, 1–14. https://doi.org/10.1016/j.cep.2013.01.005

Wang, L., & Sundén, B. (2004). An experimental investigation of heat transfer and fluid flow in a rectangular duct with broken V-Shaped ribs. *Experimental Heat Transfer*, *17*(4), 243–259. https://doi.org/10.1080/08916150490487611

Wu, Y., Gan, G., Verhoef, A., Vidale, P. L., & Gonzalez, R. G. (2010). Experimental measurement and numerical simulation of horizontal-coupled slinky ground source heat exchangers. *Applied Thermal Engineering*, *30*(16), 2574–2583. https://doi.org/10.1016/j.applthermaleng.2010.07.008

Xin, R. C., & Ebadian, M. A. (1997). The effects of Prandtl numbers on local and average convective heat transfer characteristics in helical pipes. *Journal of Heat Transfer*, *119*(3), 467–473. https://doi.org/10.1115/1.2824120

Zheng, N., Liu, W., Liu, Z., Liu, P., & Shan, F. (2015). A numerical study on heat transfer enhancement and the flow structure in a heat exchanger tube with discrete double inclined ribs. *Applied Thermal Engineering*, *90*, 232–241. https://doi.org/10.1016/j.applthermaleng.2015.07.009

CHAPTER

4

ANALYSIS OF THERMO-HYDRAULIC PERFORMANCE OF DDIR ON LOW CURVATURE COIL IN LAMINAR FLOW FOR GSHP SYSTEM

4.1 Introduction

Renewable energy sources play a crucial role in reducing fuel dependence and decreasing environmental quality due to combustion. As one of the renewable energy sources, geothermal energy can be utilized to supply electricity, heating, and cooling in buildings. Ground Source Heat Pump utilizes a somewhat stable temperature of the ground for space conditioning. However, the installation of ground heat exchangers (GHE) is quite expensive, which has become an obstacle in the widespread use of the GHSP. The solution to this problem is to use a heat pump combined with horizontal GHE. This GHE is cheaper in installation cost than that of other GHEs.

One of the most widely used horizontal GHE is the slinky type. This GHE only requires 20-30% of the length of the trench needed for a single pipe GHE configuration. The first study of the slinky application of GHE in combination with GSHP was carried out by Bose and Smith (1992). They stated that Slinky GHE could increase the increase in heat transfer area in limited space compared to other horizontally buried heat exchangers.

The Slinky GHE has a curvature which generates secondary flow due to centrifugal force. The slinky GHE has high efficiency can be attractive for business and homeowners to use GSHP. Design and appropriate operating strategies can be valuable for achieving this goal. Slinky GHE, coil curvature, is 2 m^{-1}, experimentally investigated in vertical and horizontal configurations. Based on this study, a vertical configuration has a better heat extraction rate performance than horizontal (Ali et al., 2017).

Most GHE slinky coils have small curvature. Hardik et al. (2015) examined the effect of curvature on the heat transfer coefficient. They stated that the increase in the curvature coil was accompanied by an increase in the heat transfer coefficient. Efforts to improve the performance of heat transfer are better by modifying the wall of the pipe to produce eddy vortex in a heat exchanger.

One method to improve heat transfer is to install double discrete inclined ribs (DDIR) on the tube wall. Meng et al. (2005), the first inventor of DDIR-tube, state that DDIR use on straight pipes can increase convective heat transfer in laminar flow. These ribs could generate multi-longitudinal vortex; hence good thermal mixing is obtained. Several studies have been conducted to determine the characteristics of heat transfer and pressure drop from DDIR-tube. Li et al. (2009) conducted a numerical and experimental study of 6 pairs of Ribs in the turbulent flow regime with Reynolds number from 15000 to 60000. They concluded that heat transfer increased 100-120% compared to plain tube, and pressure drop also increased 170-250%. Visualization of the flow field shows that there are additional vortices at the front and back of the ribs so that it generates vortex at the core of the flow. Zheng et al. (2015) conducted a numerical study of 3 pairs of ribs on several designs. They showed an increase in heat transfer around 1.8 to 3.6 times greater than the smooth tube, while the friction factor increased 2.1 to 5.6 times. The value of the Performance Evaluation Criteria (PEC) calculated based on the same pumping power has varied between 1.3 and 2.3.

The following year, Zheng et al. (2016) examined the effect of ribs configuration on flow patterns and heat transfer. They observed the detail of the flow structure generated by the parallel type ribs (P-Type) and V shape type ribs (V-type). They conclude that the average number of numbers and friction factors of V-type ribs have 25-76% and 86-94% higher than that of P-type ribs, respectively. Flow structure shows that P-type ribs only generate a vortex, while V-type ribs generate many

vortexes. Most of the research on DDIR-tube is carried out on straight pipes. In order to overcome low curvature coil, we want to clarify the performance of DDIR in the coil for GSHP application.

4.2 Computational Methods

In Fig. 4. 1, the domain is divided into 3 parts, namely inlet, coil, and exit areas. The length (l) of the inlet and exit area is 200 mm, while the axial length (L) of the coil is 3.53 m. inside and outside diameter of the tube are 14.46 and 15.88 mm, respectively. Whereas pitch (P) and diameter of the coil (D) are 100 and 900 mm, respectively.

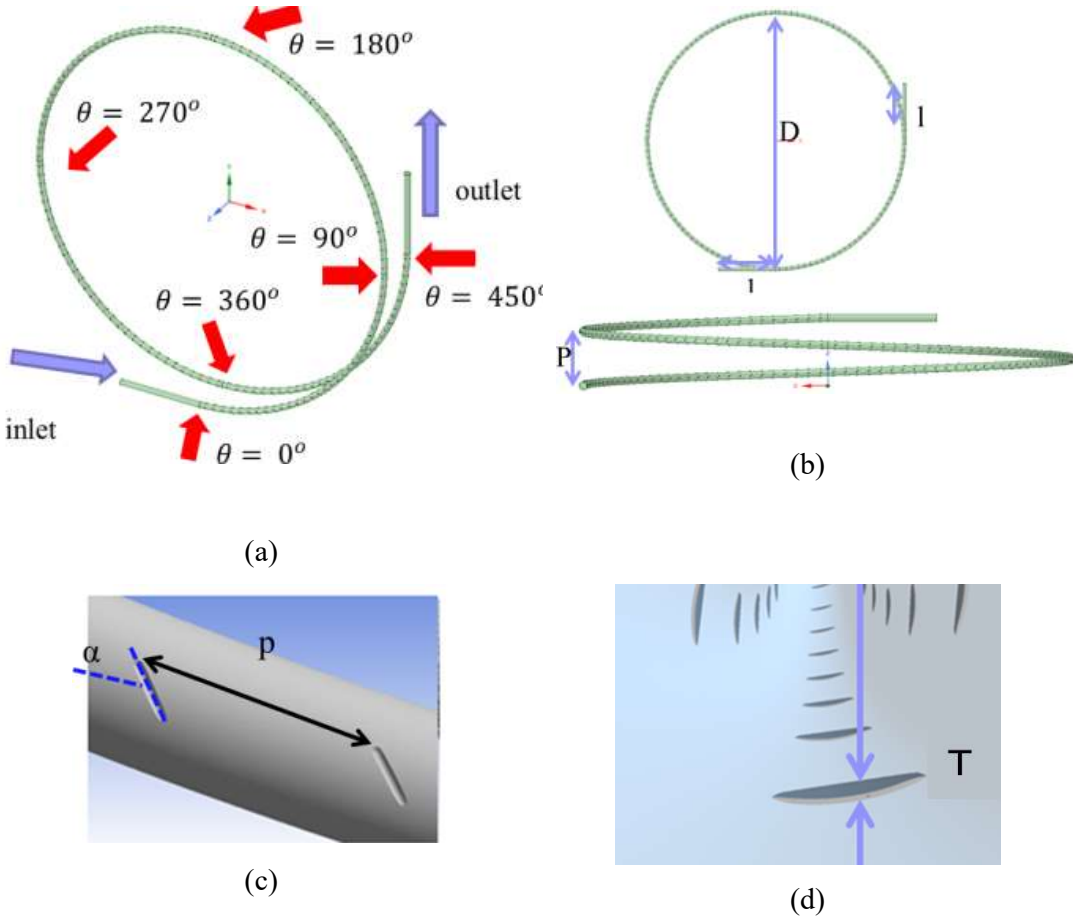

Fig. 4.1 (a) General view of the computational domain and several cross-sections of the coil for data collection; (b) view from top and side; (c) Location of ribs outside view; (b) Location of ribs inside

Three variations of the ribs height can be seen at table. Plain coil (PC) is used to determine the increase in heat transfer performance and the fluid flow of DDIR. The working fluid is water. All simulations are in steady-state conditions with Reynolds

number from 1028 to 5144. The simulations are carried out by using the turbulence model k-ω SST

Table 4.1. Details Geometry of Heat Exchanger Models

Model	Ribs Height (mm)	Ribs Angle (°)	Ribs Pitch (mm)	Curvature Coil (m^{-1})
RHC1	0.45	45	22	2.22
RHC2	0.75	45	22	2.22
RHC3	1	45	22	2.22
PC	-	-	-	2.22

This simulation has used several boundary conditions, i.e., inlet, wall tube, and outlet are velocity inlet, constant wall temperature, and outflow. The inlet water and wall temperatures are 280 K and 291 K, respectively. This temperature setting refers to our previous research conducted by Ali et al. (2017) at Saga University.

4.3 Data Reduction

The following equation calculates the heat transfer rate of the coil

$$Q = \dot{m} c_p (T_o - T_i) \tag{4.1}$$

The average heat transfer coefficient based on the simulation results of the flow and temperature fields calculated based on LMTD as follows

$$h = \frac{Q}{\int_A dA \, \Delta T_m} \tag{4.2}$$

Where,

$$\Delta T_m = \frac{(T_w - T_o) - (T_w - T_i)}{\ln\left(\frac{T_w - T_o}{T_w - T_i}\right)} \tag{4.3}$$

In this simulation, fluid properties are assumed to be constant so that the use of LMTD calculation is valid. Several dimensionless parameters such as Nusselt number, Reynolds number and friction factor are used as follows

$$\mathrm{Re} = \frac{\rho u d}{\mu} \tag{4.4}$$

$$Nu = \frac{hd}{\lambda} \tag{4.5}$$

$$f = \frac{\Delta p}{\left(\frac{l}{d}\right)\left(\rho \frac{v^2}{2}\right)} \tag{4.6}$$

For critical Reynolds number of flow in coil, Ito's correlation is utilized as follows

$$\mathrm{Re}_{cr} = 20000\left(\frac{d}{D}\right)^{0.32} \tag{4.7}$$

The critical Reynolds number of the coil in this research is 5322.

The utilization of ribs is evaluated by the Coefficient of Performance (COP) improvement factor in heating mode which is derived from Jalaluddin and Miyara (2015).

$$\frac{Q_C'}{Q_C} - \frac{V\,\Delta p}{Q_C}\frac{\Delta p'}{\Delta p} > 0 \tag{4.8}$$

The details derivation of Equation 4.8 can be seen in 3.2.3. The equation (4.8) tells that if the left term is bigger than zero, then COP is enhanced. All of the COP improvement factors are evaluated based on thermal and hydraulic performance of a straight tube. Several Nusselt number and friction factor correlations in a straight tube are applied to determine laminar, transition, and turbulent because Reynolds number range is from 1028 to 5144.

Nusselt number and friction factor for laminar region

$$Nu = 3.66 \tag{4.9}$$

$$f = \frac{64}{\mathrm{Re}} \tag{4.10}$$

Meanwhile, Nusselt number for transition region is solved by using a linear interpolation method of modified Gnielinski Nusselt number for uniform wall temperature (Gnielinski, 2013). The interpolations is valid for 2300< Re < 4000 as follows.

$$Nu = (1-\gamma)\,\mathrm{Nu}_{lam,2300} + \gamma\,\mathrm{Nu}_{turb,4000} \tag{4.11}$$

With

$$\gamma = \frac{\mathrm{Re}-2300}{2300-4000} \tag{4.12}$$

$\mathrm{Nu}_{lam,2300}$ is calculated by the following equation

$$Nu_{m,T} = \left(Nu_{m,T,1}^3 + 0.7^3 + \left(Nu_{m,T,2} - 0.7 \right)^3 + Nu_{m,T,3}^3 \right)^{1/3} \tag{4.13}$$

Where

$Nu_{m,T,1} = 3.66$ and

$Nu_{m,T,2} = 1.615\sqrt[3]{\mathrm{Re}\,\mathrm{Pr}\,d/L}$ and

$$Nu_{m,T,3} = \left(\frac{2}{1+22\,\mathrm{Pr}} \right)^{1/6} \left(\mathrm{Re}\,\mathrm{Pr}\,d/L \right)$$

Then $\mathrm{Nu}_{turb,4000}$ is calculated by the following equation

$$Nu = \frac{(f/8)(\mathrm{Re}-1000)\,\mathrm{Pr}}{1+12.7\sqrt{f/8}\,(\mathrm{Pr}^{2/3}-1)} \left[1+\left(\frac{d}{L} \right)^{2/3} \right] K \tag{4.14}$$

The K factor is

$$K = \left(\frac{\mathrm{Pr}}{\mathrm{Pr}_w} \right)^{0.11}$$

In eq. (4.14), the Konakov friction factor is used as follows

$$f = (1.8\,\mathrm{Log}_{10}\,\mathrm{Re} - 1.64)^{-2} \tag{4.15}$$

In transition region use proposed friction factor by Abraham et al. (2011) which is valid in transition region (2300 < Re < 4500) as follows

$$f = 3.0310^{-12}\,\mathrm{Re}^3 - 3.6710^{-8}\,\mathrm{Re}^2 + 1.4610^{-4}\,\mathrm{Re} - 0.151 \tag{4.16}$$

In turbulent region, Nusselt number for eq. (4.14) can be utilized. Then, Petukhov friction factor can be applied as follows

$$f = (0.79\,Ln(\mathrm{Re}) - 1.64)^{-2} \tag{4.17}$$

Figure 4.2 shows the Nusselt number and friction factor values in the laminar, transition and turbulent flow regimes based on several correlations in the Reynolds number from 100 to 6000.

4.4 Grid Independence and Validation

The three-dimensional mesh is created using Ansys Meshing 17.2. The fluid domain is discretized by unstructured mesh. To confirm precise results, three mesh sets, 26056369 (coarse), 26632952 (medium), and 27379496 (fine), are used to test grid independence at Reynolds number is the 4115.

In this test, heat transfer rate and pressure drop are evaluated. The relative deviation of heat transfer and pressure drop is calculated based on fine mesh. Heat transfer rate of coarse, medium, and fine mesh are 652.111, 652.189, and 652.490 W/m, respectively. The deviation heat transfer from coarse to fine and medium to fine are 0.058 and 0.046 %, respectively. The pressure drop of coarse, medium, and fine mesh are 397.590, 397.585, and 397.840 Pa/m, respectively. The deviation pressure drop from coarse to fine and medium to fine are 0.062 and 0.064 %, respectively. Therefore, the 27379496-mesh system is chosen sufficiently dense for the simulation.

Simulation is validated with our previous experiment Kuriyama et al. (2019) shown in Fig. 4.3 and 4.4. The experimental and simulation results for both Nu numbers and friction factors have a similar pattern even though some deviations happen. The average deviation between experimental and simulation for friction factor and Nusselt number are 11.69% and 12.43%, respectively.

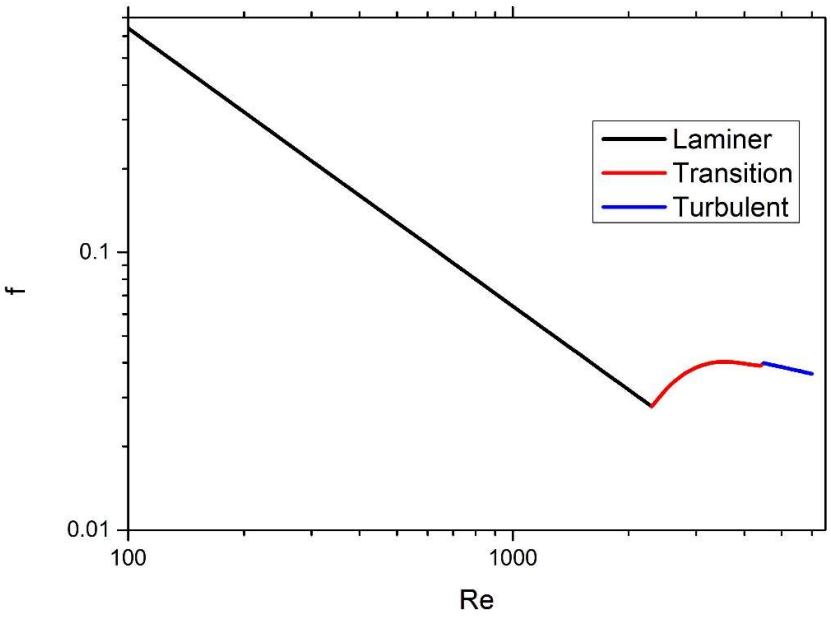

(a)

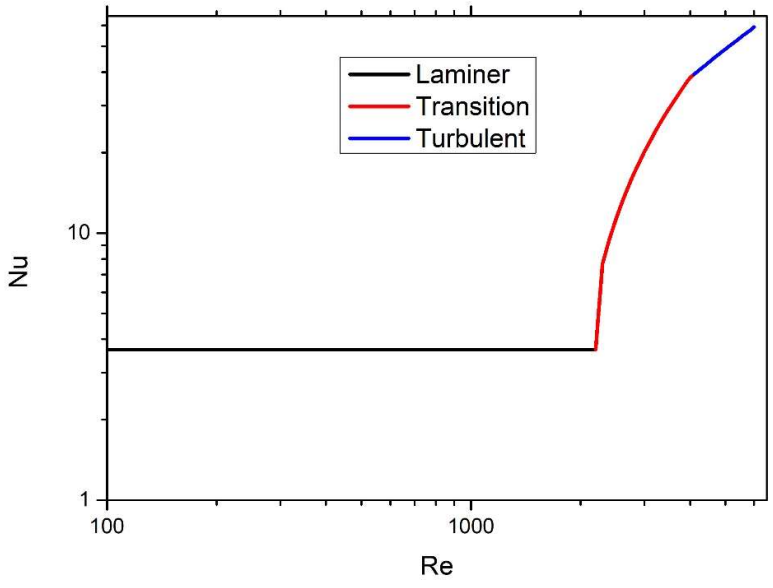

(b)

Fig 4.2 plotting several correlations of (a) friction factors (b) Nusselt number

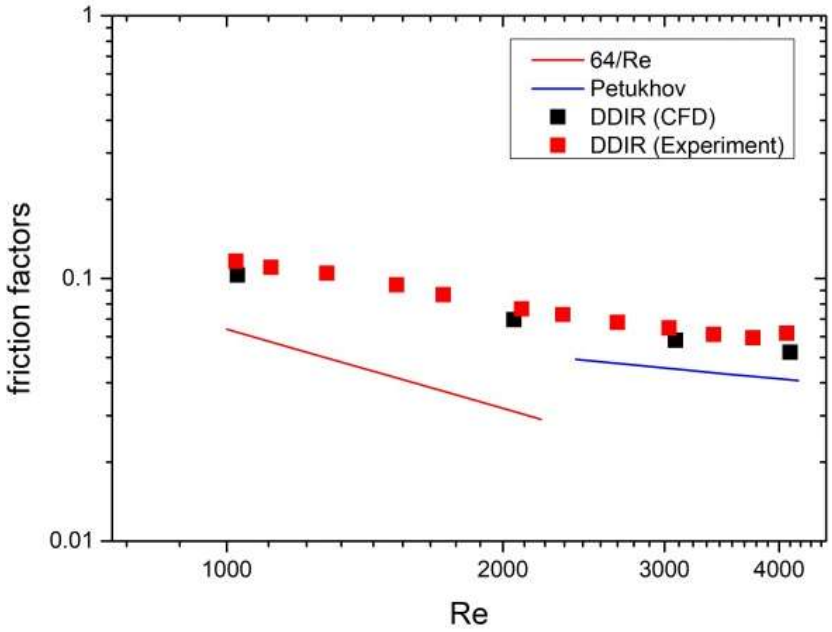

Fig. 4.3 Comparison of Numerical and Experimental friction factors

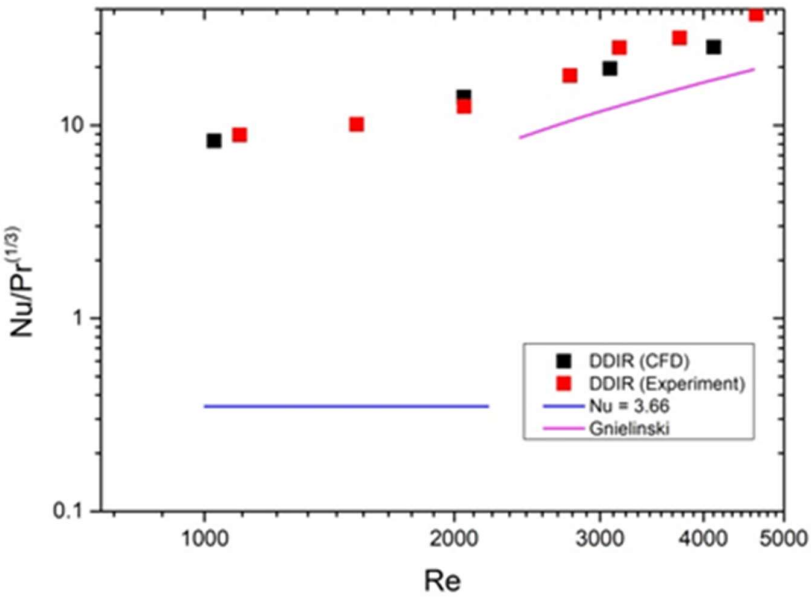

Figure 4.4 Comparison of Numerical and Experimental Nusselt number

4.5 Result and Discussion

The numerical results of this study are shown from Fig. 4.5 to 4.11, which depict pressure drop, velocity field, heat transfer rate, temperature field, flow structure, and COP Improvement factors, respectively.

4.5.1 Fluid Flow

In Fig. 4.5, the graph compares the frictional pressure drop of PC and RHCs in coil from 1 to 5 L/min. Overall, the pressure drops of RHC2 and RHC3 increases sharply over flowrate range, whereas the PC and RHC1 rise gradually. In 1 L/min, all of the coils just below 50 Pa/m. meanwhile, the pressure drop of PC and RHC1 far lower than that of RHC2 and RHC3, which are suffer higher pressure drop on higher flow rate. RHC2 and RHC3 seem that pressure drop has a quadratic relation to flowrate increments. The highest-pressure drop is suffered 789 Pa/m by RHC3, which relatively value about 95 % greater than that of PC at flowrate is 5L/min.

Pressure drop is a representation of energy consumption in a tube with a constant cross-sectional area (Gómez et al., 2015). Pressure drop increases due to increased height of ribs. This pressure drop is due to the use of large ribs, helping to induce a longer flow path around the ribs. The longer and stronger vortex flow causes better mixing of the fluid and can result in greater blockage of flow.

Figure 4.6 shows the change in the velocity field contour on the plain coil and ribs coil at the contour location from 0^{o} to 450^{o}. In the figure it appears that from 90 to 450 degrees there is no significant change. This phenomenon shows that the hydraulic boundary layer has been fully developed on both coils. However, what distinguishes the two coils is the contour distortion in the ribs coil. It is clearly seen that ribs can produce some swirl which could be distorted the contour. On the contour, We see that it could be local acceleration of flow near the ribs due to longer flow path. The higher velocity move tends to move close to outer side of coil, especially in a ribbed tube. This could trigger the thinning of the boundary layer some parts in outer coil.

4.5.2 Heat Transfer Rate

In Fig. 4.7, the scatter graph illustrates the heat transfer rate increment PC and RHCs on flowrate between 1 and 5 L/min. Overall, heat transfer rate increase in all of type of coil and more enhancement heat transfer by RHCs rather than heat transfer by PC. Furthermore, the most significant increment of heat transfer is RHC3. The number of heat transfer rate on RHC3 begin at just under 200 W/m in 1 L/min and rise significantly to reach over 850 W/m in 5 L/min. Around 150 W/m heat transfer of PC

in 1 L/min before climbing steadily, just over 650 W/m in 5 L/min. The heat transfer rate of RHC1 and RHC2 are between PC and RHC3 for the entire flow rate. We can see clearly that all the coils tend to have an almost linear relation with the increase of flow rate. The highest heat transfer rate is 873 W/m by RHC3, which about 26 % greater than that of PC at flowrate 5 L/min. Heat transfer rates from wall to fluid increase with increasing height of ribs. The longer flow path and strong vortex also contribute to better thermal mixing. This phenomenon could lead to less thermal resistance in the heat exchanger.

In Fig. 4.8, we can see temperature field of PC and RHC2 on cross-section from 0° to 450° at Re = 4115. We can undoubtedly identify that ribs capable of generating flow, which can alter temperature field. We can see that the ribs tube tends to have a hotter cross-section than that of plain coil. This phenomenon is caused by better thermal mixing of swirl generated by ribs. The contour also shows that the ribs coil capable of obtaining higher temperatures in the same axial length of coil. This performance could lead to less cost installation of the heat exchanger.

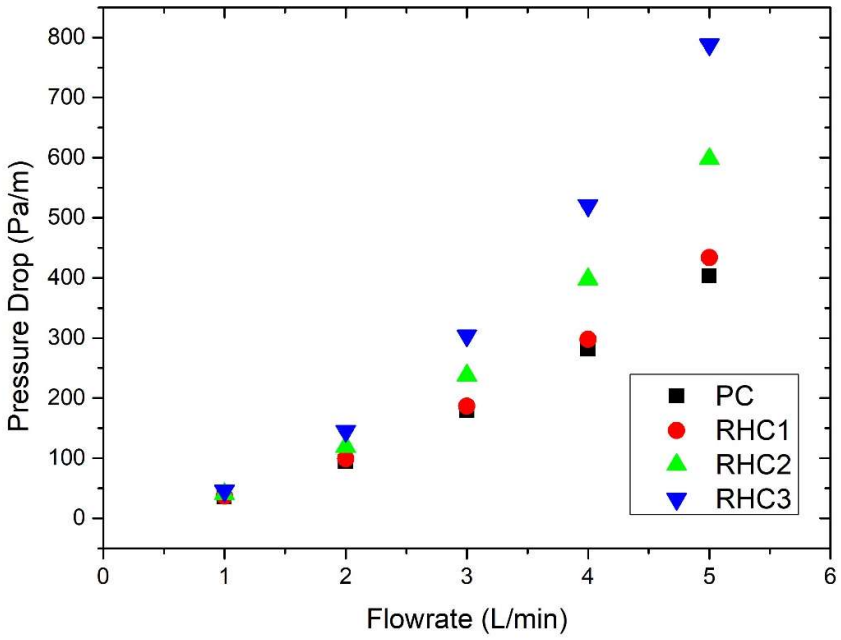

Fig. 4.5 Comparison of Pressure drop in different configuration of coil

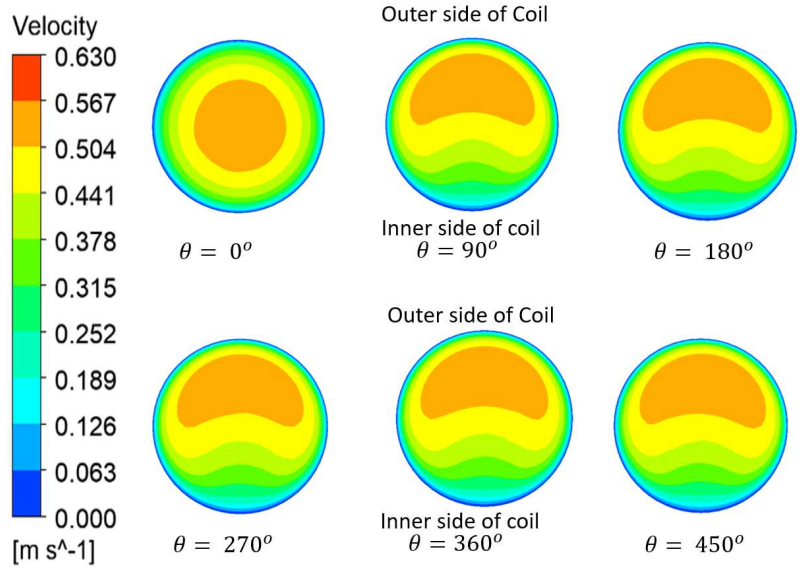

(a)

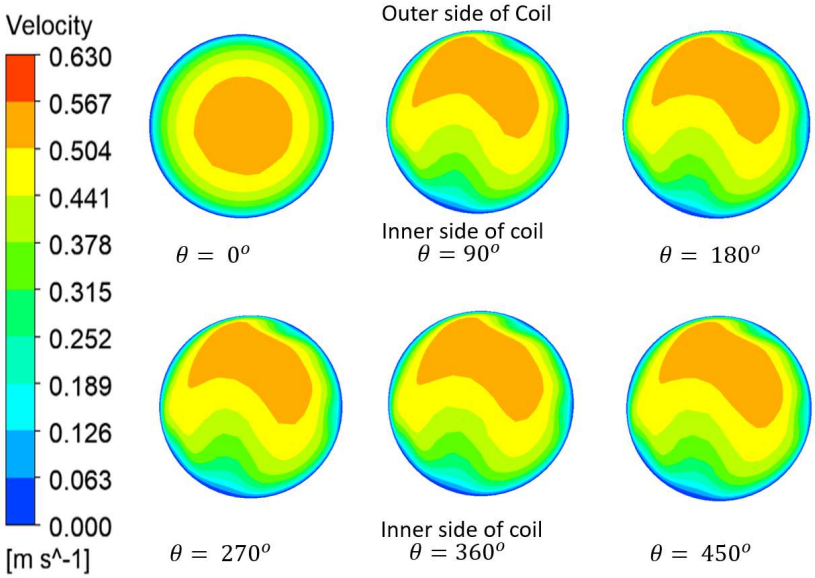

(b)

Fig. 4.6 velocity contour on several downstream cross-section at 4 L/min (a) PC, (b) RHC2

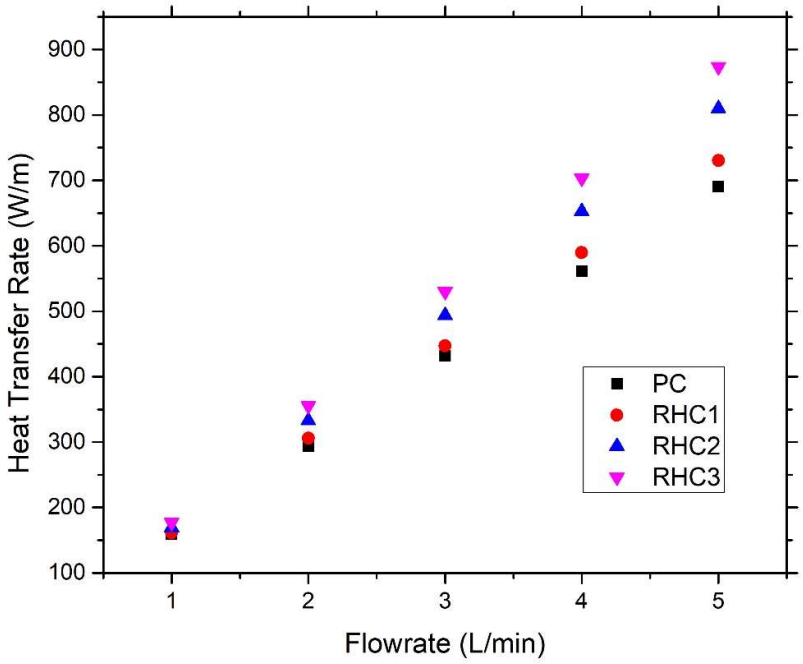

Fig. 4.7 Comparison of Heat transfer rate in different configuration of coil

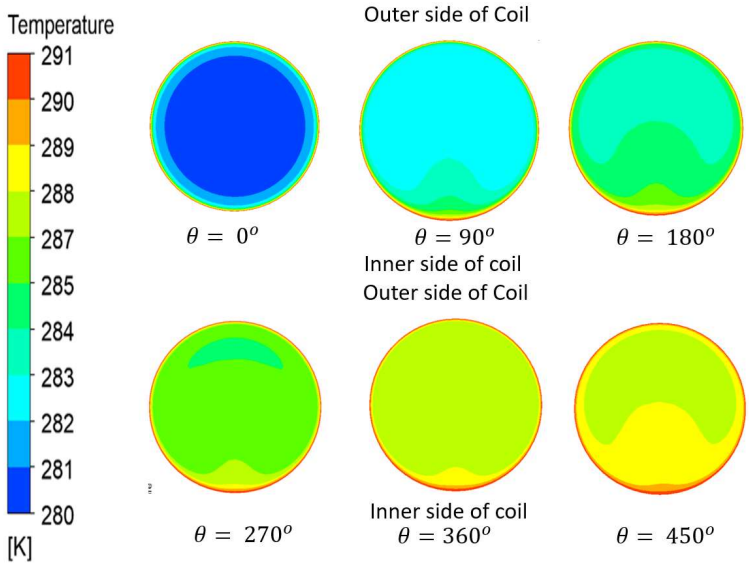

(a)

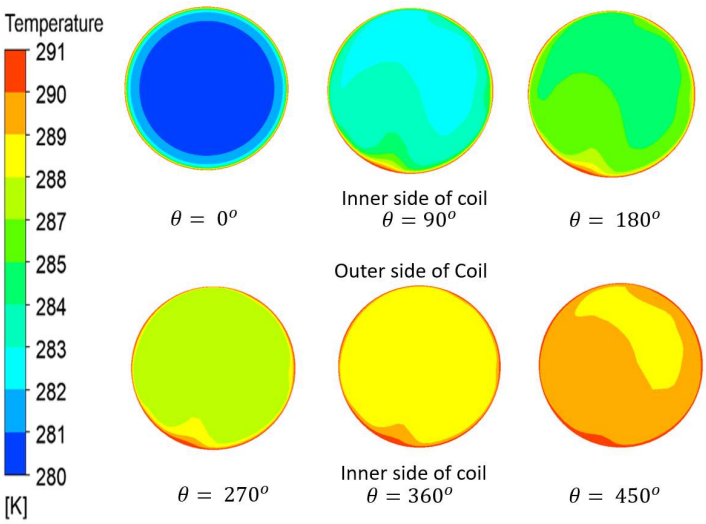

(b)

Fig. 4.8 Temperature contour on several downstream cross-section at 4 L/min (a) PC, (b) RHC2

4.5.3 Secondary Flow

In general, the secondary flow on the pipe bend is symmetry. However, we found out no symmetrical secondary flow structure, both PC and RHCs in this study. Based on research by Tang et al. (2017), secondary flow distortion is caused by the effect of the low curvature coil. Based on several studies of application V-type DDIR in a straight tube, the more installed ribs, the more vortexes generated (Li et al., 2009; Meng et al., 2005; Zheng et al., 2015). Nevertheless, in our study, we do not find any additional number of vortices on the low curvature coil. In general, the use of ribs is seen to be able to induce the flow around ribs to affect the main flow structure, both strength and distortions flow pattern. This phenomenon could be the answer to why higher height of ribs could promote enhancement of heat transfer (Fig. 4.7) and pressure drop (Fig. 4.5) in low curvature coil.

4.5.4 COP Improvement Factor

Fig. 4.10 shows the COP Improvement factor with regards to flowrate in a low curvature coil. COP Improvement factor is described in Eq. 8. Generally, it is evident that increasing high of ribs flowrate could increase the COP Improvement factor, especially in the entire flow rate. In contrast to earlier findings, however, the decrement of COP Improvement factor was detected mainly in medium to higher flow rate.

As shown in Fig. 4 and Fig 6, we clarify in the improvement of flow rate could enhance both heat transfer and pressure drop. However, it seems that the increase of pressure drop in quadratic relation, whereas the increase of heat transfer rate in almost linear relation in increasing the flow rate from 3 to 5 L/min. Based on both parameters, we can see the COP improvement factor will probably decline steadily after 5 L/min. This phenomenon could be the energy enhancement of heat transfer could not compensate energy loss of frictional pressure drop. However, the strange trend of the COP Improvement Factor happens on a low range flow rate between 1 (Re = 1028) and 2 L/min (Re = 2057). The COP Improvement factor increase in the increase in flowrate. The highest COP Improvement Factor is obtained 0.339 by RHC3, which relatively value about 478 % higher than that of PC at flowrate is 5 L/min.

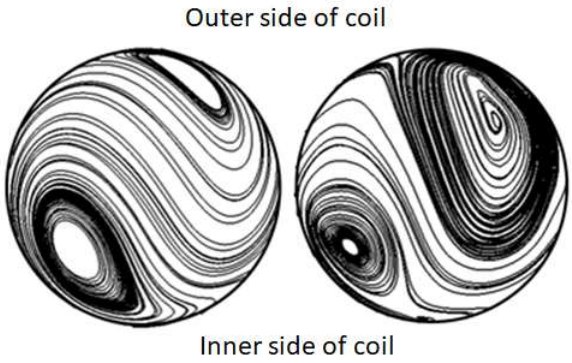

Fig. 4.9 secondary flow of PC (left) and RHC2 (right) on downstream cross section at 4 L/min.

In our research, we use the Reynolds number range from 1028 to 5144 on the coil. Based on Eq. (7), the critical Reynolds number of the coil is 5322; thus, all of Reynolds number in the coil is still laminar regime. However, the problem appears because, in our COP Improvement factor, we use straight tube correlations as a baseline to calculate thermal and fluid flow performance on all of the coils. Gnielinski (2013) and Abraham et al. (2011) state that heat transfer and pressure drop straight tube on the laminar to transition regime need to be evaluated.

Most of the heat transfer and pressure drop correlations have a gap at Re = 2300. Because of this problem, they make new correlations, as shown from Eq. (11) to Eq. (16). The mixing in the coil is higher than in the straight tube at the same flowrate and length of the tube (Naphon and Wongwises, 2006). Moreover, Srinivasan et al. (1968) Srinivasan states that the effect of coil curvature is substantially greater in laminar flow

than turbulent flow. On the laminar flow of the straight tube, it could be no eddies in flow field; hence heat transfer is less. In coil, the secondary flow appears in the same flowrate; hence proper thermal mixing occurs, and heat transfer enhancement. This reason is why the COP Improvement factor increases drastically for flow rate of 1 and 2 L/min.

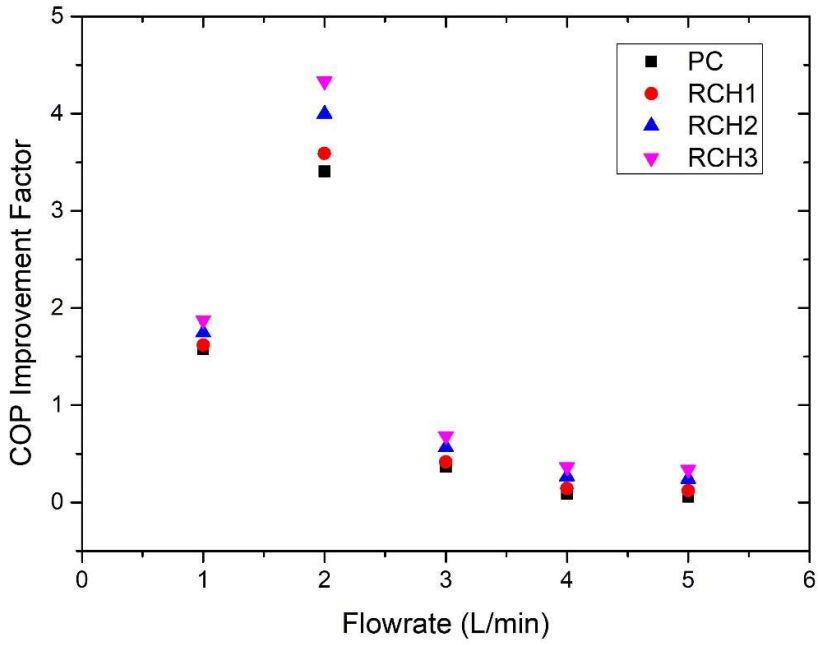

Fig 4.10. Comparison of COP Improvement factor configuration of coil

4.6 Conclusion

Numerical simulation of steady laminar flow for V-type DDIR in low curvature coil was investigated. Numerical solution of heat transfer rate and pressure drop in DDIR coil indicates that the DDIR could generate flow is better to heat transfer enhancement in laminar convection in the coil. The DDIR tube is developed. We find that the additional vortexes seem do not appears on the flow field. However, the effect of flow generated by ribs may merge with the main flow field; hence the vortex of the flow field become stronger. The heat transfer trends are almost linearly increased with the increase of flow rate, and the higher ribs height make higher heat transfer rate. The heat transfer rate of DDIR could maximum enhance at 26 % greater than that of PC. On the contrast, pressure drop trends are quadratic relation with the increase of flow rate and high of the ribs. The pressure drop of DDIR could maximum enhance at 95 % greater than that of PC. The unique pattern is shown at COP Improvement factors

because Reynolds number of the straight tube as baseline calculation to still in the transition regime. The sudden gap appears in the transition regime. The COP improvement factor decrease in increasing flowrate. However, DDIR tube still have superiority by 478 % greater than that of PC.

4.7 References

Abraham, J. P., Sparrow, E. M., & Minkowycz, W. J. (2011). Internal-flow Nusselt numbers for the low-Reynolds-number end of the laminar-to-turbulent transition regime. *International Journal of Heat and Mass Transfer*, *54*(1–3), 584–588. https://doi.org/10.1016/j.ijheatmasstransfer.2010.09.012

Ali, M. H., Kariya, K., & Miyara, A. (2017). Performance analysis of slinky horizontal ground heat exchangers for a ground source heat pump system. *Resources*, *6*(4), 1–18. https://doi.org/10.3390/resources6040056

Bose, J. E., and Smith, M. D. (1992). Performance of new ground heat exchanger configurations for heat pump. *Solar Engineering 1*.

Gnielinski, V. (2013). On heat transfer in tubes. *International Journal of Heat and Mass Transfer*, *63*, 134–140. https://doi.org/10.1016/j.ijheatmasstransfer.2013.04.015

Gómez-Pérez, C. A., Espinosa, J., Montenegro Ruiz, L. C., & van Boxtel, A. J. B. (2015). CFD simulation for reduced energy costs in tubular photobioreactors using wall turbulence promoters. *Algal Research*, *12*, 1–9. https://doi.org/10.1016/j.algal.2015.07.011

Hardik, B. K., Baburajan, P. K., & Prabhu, S. V. (2015). Local heat transfer coefficient in helical coils with single phase flow. *International Journal of Heat and Mass Transfer*, *89*, 522–538. https://doi.org/10.1016/j.ijheatmasstransfer.2015.05.069

Jalaluddin, & Miyara, A. (2015). Thermal performance and pressure drop of spiral-tube ground heat exchangers for ground-source heat pump. *Applied Thermal Engineering*, *90*, 630–637. https://doi.org/10.1016/j.applthermaleng.2015.07.035

Kuriyama, G., Ariwibowo, T. H., Kariya, K., & Miyara, A. (2019). Heat Transfer and Presser Drop Characteristics of Curved Tube with Discrete Ribs for Ground Source Heat Exchanger. *The 2019 Annual Conference of the Japan Society of Refrigerating and Air Conditioning Engineers*, 9–14. Tokyo: JSRAE.

Li, X. wei, Meng, J. an, & Guo, Z. yuan. (2009). Turbulent flow and heat transfer in

discrete double inclined ribs tube. *International Journal of Heat and Mass Transfer*, *52*(3–4), 962–970. https://doi.org/10.1016/j.ijheatmasstransfer.2008.07.027

Meng, J. A., Liang, X. G., Chen, Z. J., & Li, Z. X. (2005). Experimental study on convective heat transfer in alternating elliptical axis tubes. *Experimental Thermal and Fluid Science*, *29*(4), 457–465. https://doi.org/10.1016/j.expthermflusci.2004.04.006

Naphon, P., & Wongwises, S. (2006). A review of flow and heat transfer characteristics in curved tubes. *Renewable and Sustainable Energy Reviews*, *10*(5), 463–490. https://doi.org/10.1016/j.rser.2004.09.014

Srinivasan, P., Nandapurkar, S., & Holland, F. (1968). Pressure drop and heat transfer in coils. *Chem Eng (Lond)*, *218*, 113–119.

Tang, L., Yuan, S., Malin, M., & Parameswaran, S. (2017). Secondary vortex-based analysis of flow characteristics and pressure drop in helically coiled pipe. *Advances in Mechanical Engineering*, *9*(4), 1–11. https://doi.org/10.1177/1687814017700059

Zheng, N., Liu, P., Shan, F., Liu, Z., & Liu, W. (2016). Effects of rib arrangements on the flow pattern and heat transfer in an internally ribbed heat exchanger tube. *International Journal of Thermal Sciences*, *101*, 93–105. https://doi.org/10.1016/j.ijthermalsci.2015.10.035

Zheng, N., Liu, W., Liu, Z., Liu, P., & Shan, F. (2015). A numerical study on heat transfer enhancement and the flow structure in a heat exchanger tube with discrete double inclined ribs. *Applied Thermal Engineering*, *90*, 232–241. https://doi.org/10.1016/j.applthermaleng.2015.07.009

CHAPTER

5

THERMAL AND FLOW CHARACTERISTICS OF DISCRETE DOUBLE INCLINED RIBS AT LOW CURVATURE COIL FOR GSHP APPLICATION

5.1 Introduction

The Ground Source Heat Pump (GSHP) has been proven as an efficient technology in the utilization of geothermal since the end of 1940s. The application of GSHP does not require high geothermal energy and can be installed in many places. This utilization is because soil temperatures have small fluctuations, while ambient air temperatures vary drastically. For example, in winter, air temperatures fluctuate from 0 ^{o}C to 16 ^{o}C (Chong et al., 2013).

Ground Heat Exchanger (GHE) is the primary key in the performance of the GHSP System. Increasing the efficiency of the GSHP system can be done by increasing the efficiency of GHE. Therefore, increasing the efficiency of the GSHP system can be done by increasing the efficiency of GHE by adopting a more advanced geometry. In general, Ground Heat Exchangers (GHE) in the GSHP systems is classified into two, namely the vertical GHE (VGHE) loop and horizontal GHE (HGHE) loop.

Popular HGHE horizontal loop configurations are straight pipe heat exchangers and slinky heat exchangers (Chong et al., 2013). This heat exchanger requires a more extensive installation area than that of vertical GHE (VGHE). Based on studies of GHE geometry, slinky GHE is commonly utilized in HGHE application. This GHE has

several advantages over vertical heat exchangers, i.e., easy installation, no need for special installation skills, and low installation costs. HGHEs are commonly set up in shallow trenches at a depth of 1 to 2 m from the ground surface.

To improve GHE performance, many researchers changed the tube design, some of which were on VGHE. Fin (Bouhacina et al., 2015), and grooved tube (Acuña and Palm, 2010) were applied to improve thermal performance of VGHE. However, the modification of the geometry configuration is not commonly found in HGHE, especially the slinky type.

Several studies have been carried out to improve the performance of the slinky HGHE. Wu et al. (2010)investigated some curvature coils and coil central intervals. They concluded that the difference in curvature did not show a significant increase in heat transfer extraction. However, a small curvature has a higher heat extraction rate at the same trench length. Central distance intervals increase specific heat extraction. However, increasing the central interval distance decreases the heat extraction at the same trench length. Selamat et al. (2016)conducted simulation on the influence of the reclined and standing orientation of the slinky-ground heat exchanger. The results of this study indicate the use of standing orientation can extend the adequate period time by 14%. Ali et al. (2017) investigated the effect of standing and reclined orientation on the performance of slinky ground heat exchangers. They stated that the increase in heat transfer standing was higher than that of reclined. Standing slinky ground heat exchangers are influenced by deeper soil temperatures besides the amount of black fill material standing is more excellent than reclined slinky ground heat exchangers, which have higher thermal conductivity than the soil at the location.

Slinky GHE type has a low curvature coil. Hardik et al., (2015) experimented with the effect of curvature on the coefficient of heat transfer on several types of coil. They claim that large curvature results in high heat transfer due to strong secondary flow for thermal mixing. The curvature coil performance character has similarities with a straight tube. In low curvature coil, the weak centrifugal force leads to a low-pressure drop and low-heat transfer, especially at low flow rates Choi et al. (2018). Hence, this weakness could be solved by augmentation of coil.

Meng (2003) conducted experiment augmented the first Discrete Double Inclined Ribs (DDIR) straight tube study to improve heat transfer performance in the heat exchanger as his Ph.D. thesis in 2003. The result shows that the ribs could generate longitudinal vortex. Li et al. (2009) did experiment and simulation of the thermal

characteristics of the DDIR-tube. They concluded that DDIR-straight tube could increase heat transfer increase from 100% to 120% higher than that of plain tube. However, the pressure drop has also increased from 170% to 250%. Zheng et al. (2016) analyzed the thermal and fluid flow performance of DDIR-tubes using numerical analysis. Based on this study, DDIR-tube can increase heat transfer and friction factor 1.58-2.46 and 1.82-5.03 times above than that of smooth tube, respectively.

We conducted preliminary studies on the effect of DDIR on the 2.22 m^{-1} curvature coil (Ariwibowo et al., 2019a, 2019b, 2019c; Kuriyama et al., 2019). The result shows that in heat transfer and pressure drop increase in the increase both ribs height and flowrate. Higher ribs can lead to a more significant distorted vortex of flow structure. The research shows that the use of DDIR-coil show two vortexes. This result is the opposite of the use of DDIR-straight tube which The addition of ribs can increase the amount of vortex. This phenomenon could be caused combine among three flow, i.e., primary flow, secondary flow, and rib-induced flow. However, we do not know which flow and which geometry configurations could enhance heat exchanger performance of DDIR-coil. Based on our best knowledge, there has been no research about the application of DDIR on low curvature coil heat exchanger. The goal of this research is to present a good DDIR-coil design and to obtain the characteristics of heat transfer and fluid flow in several coil configurations for GSHP application.

5.2 Materials and Methods

5.2.1 Model Descriptions

The illustration diagram of DDIR-coil used in this study is shown in Figure 5.1. The coil consists of three parts, namely inlet extension, test section, and outlet extension. In all simulations, the length of the extension both inlet and outlet is 200 mm. This extension is to ensure that flows almost fully developed and eliminates disturbance in the downstream section.

The tube inside diameter, tube thickness, coil pitch, number of ribs at one perimeter are 14.46 mm, 0.71 mm, 100 mm, and four pieces, respectively. The geometry configuration of all models can be seen in table 1. The curvature of coil is defined as $\mathrm{C} = 1/R$ where R is the radius of coil. To find out the effect of DDIR-coil on increasing the heat exchanger performance, we also calculate straight-tube, plain-coil, and DDIR-straight tube as a benchmark. Whereas diameter of the coil, angle of ribs,

Curvature are symbolized as *D*, *α*, and *C*, respectively. Pitch coil, pitch ribs and ribs height are symbolized as P, p and T, respectively.

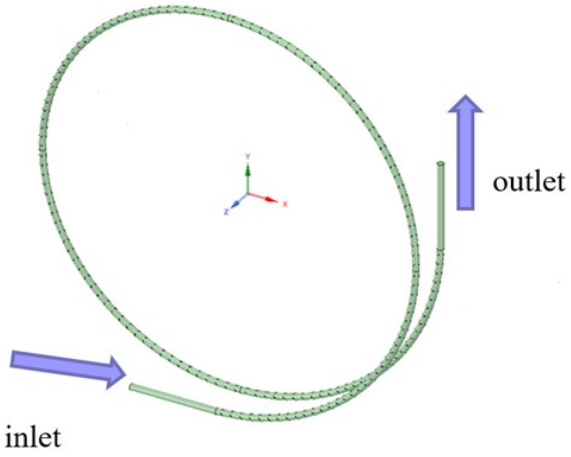

Figure 5.1 Schematic diagram of the DDIR-coil.

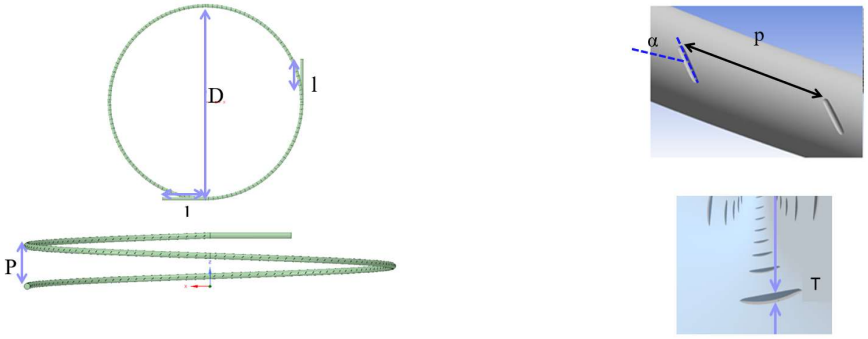

(a) (b)

Figure 5.2 Structure and configuration of DDIR-coil (a) Top view and side of coil, (b) Location of ribs inside and outside coil surface

Table 5.1. Geometric specifications of the Heat Exchanger model.

Model	Curvature of coil (m^{-1})	Ribs Height (mm)	Ribs Angle (°)	Ribs Pitch (mm)	Axial Length (mm)
MR-C1	3.33	1	45	22.50	2359
MR-C2	2.66	1	45	22.50	2948
MR-A1	2.22	1	20	22.50	3534
MR-A2	2.22	1	30	22.50	3534
MR-P1	2.22	1	45	33.75	3534
MR-P2	2.22	1	45	45.00	3534
MR-P3/MR-C3/MR-A3	2.22	1	45	22.50	3534
MR-S	-	1	45	22.50	3534
MP-C1	3.33	-	-	-	2359
MP-C2	2.66	-	-	-	2948
MP-C3	2.22	-	-	-	3534

5.2.2 Governing Equation and Mathematical Methods

The flow simulation utilizes Reynolds averaged Navier-Stokes (RANS) equation. The simulation is assumed as heat transfer, and fluid flow is turbulent, steady-state, and no heat loss to environment. Shear stress tensor κ-ω (SST κ-ω) is a turbulent model that shows an excellent performance in modeling adverse pressure gradient. This model combines κ-ω model in near-wall and κ-ε model in the core flow (ANSYS Academic Research, 2017).

The Governing equations are as per the following

Continuity equation:

$$\frac{\partial(\rho u_i)}{\partial x_i} = 0 \tag{5.1}$$

Momentum equation:

$$\frac{\partial(\rho u_i)}{\partial t} + \frac{\partial(\rho u_i u_j)}{\partial x_j} = -\frac{\partial p}{\partial x_i} + \frac{\partial}{\partial x_j}\left(\mu\frac{\partial(u_i)}{\partial x_j} - \rho\overline{u'_\iota u'_\jmath}\right) \tag{5.2}$$

Energy Equation:

$$\frac{\partial}{\partial x_i}(\rho T) + \frac{\partial}{\partial x_i}(\rho u_i T) = \frac{\partial}{\partial x_i}\left(\frac{\lambda}{c_p}\frac{\partial T}{\partial x_i}\right) \tag{5.3}$$

Turbulence Kinetic Energy Equation:

$$\frac{\partial(\rho\kappa)}{\partial t} + \frac{\partial(\rho u_i\kappa)}{\partial x_i} = \tilde{P}_\kappa - \beta^*\rho\kappa\omega + \frac{\partial}{\partial x_i}\left((\mu + \sigma_\kappa u_t)\frac{\partial\kappa}{\partial x_i}\right) \tag{5.4}$$

Specific dissipation rate equation:

$$\begin{aligned}\frac{\partial(\rho\omega)}{\partial t} + \frac{\partial(\rho u_i\omega)}{\partial x_i} &= \varphi\rho S^2 - \beta\rho\omega^2 + \frac{\partial}{\partial x_i}\left((\mu + \sigma_\omega u_t)\frac{\partial\omega}{\partial x_i}\right) \\ &+ 2(1 - F_1)\rho\sigma_{\omega^2}\frac{1}{\omega}\frac{\partial\kappa}{\partial x_i}\frac{\partial\omega}{\partial x_i}\end{aligned} \tag{5.5}$$

Where blending function F_1 is described as follows

$$F_1 = tanh\left\{\left\{min\left[max\left(\frac{\sqrt{\kappa}}{\beta^*\omega y}, \frac{500\upsilon}{y^2\omega}\right), \frac{4\rho\sigma_{\omega 2}\kappa}{CD_{\kappa\omega}y^2}\right]\right\}^4\right\}$$

Where

$$CD_{\kappa\omega} = max(2\rho\sigma_{\omega 2}(1/\omega)(\partial\kappa/\partial x_i)(\partial\omega/\partial x_i), 10^{-10})$$

and y is the distance to the adjacent wall

Turbulent eddy viscosity is described by

$$\upsilon_t = \frac{\varphi_1\kappa}{max(\varphi_1\omega, SF_2)}$$

Where S is a constant measure of strain rate and F_2 is a second blending function described as follows

$$F_2 = \left\{\left[max\left(\frac{2\sqrt{\kappa}}{\beta^*\omega y}, \frac{500v}{y^2\omega}\right)\right]^2\right\}$$

The SST model uses a production limiter to prevent turbulence buildup in stagnation areas as follows

$$P_\kappa = \mu_t \frac{\partial u_i}{\partial x_j}\left(\frac{\partial u_i}{\partial x_j} + \frac{\partial u_j}{\partial x_i}\right) \rightarrow \tilde{P}_\kappa = min(P_\kappa, 10.\beta^*\rho\kappa\omega)$$

All constants used, β^*, φ_1, β_1, $\sigma_{\kappa 1}$, $\sigma_{\omega 1}$, $\varphi_{2,}\beta_2$, $\sigma_{\kappa 2}$, and $\sigma_{\omega 2}$, are a combination of constants calculated based on the $\kappa - \varepsilon$ and $\kappa - \omega$ model. All equations were solved using ANSYS FLUENT 17.2 which is a commercial software based on the finite volume method. For Velocity-Pressure Coupling, the SIMPLE algorithm was utilized. The minimum convergence criterion for the continuity, velocity, and turbulence equation is 10^{-3}, and the energy equation is 10^{-7}.

5.2.3 Grid Generation and Independence Test

Three-dimensional mesh made using ANSYS Meshing 17.2. The discretized domain uses unstructured-tetrahedral elements, as shown in Figure 5.3. To obtain more accurate results, the value of y^+ is less than 1. This setting can make fine quality mesh near the wall and ribs. To find out the accuracy of numerical simulations, we use three sets of grids with 16136244 (coarse), 17779526 (medium), and 20175527 (fine) elements, which were used to test the grid independence test at Re = 4115. In this test, the pressure drop and heat transfer rate were checked.

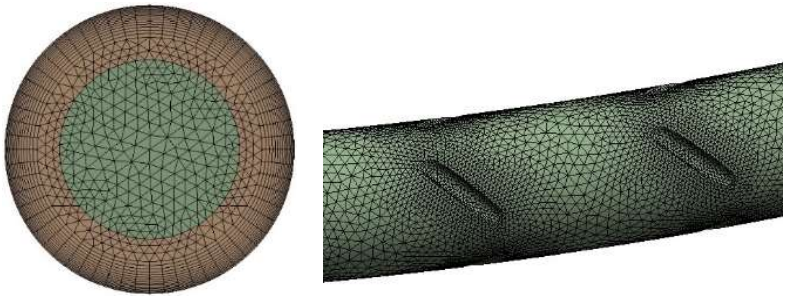

(a) (b)

Figure 5.3 Mesh system of DDIR-coil: (a) mesh in the cross-section plane of coil angle 0^o ; (b) mesh on ribs.

The relative deviations of pressure drop and heat transfer rate were determined based on the value of the fine mesh. Nusselt numbers of coarse, medium, and fine mesh

were 71.27, 72.02, and 72.76, respectively. The deviation of Nusslet number from coarse to fine and medium to fine were 2.04 and 1.01 %, respectively. Friction factors of coarse, medium, and fine mesh were 0.08273, 0.08330, and 0.08391, respectively. The deviation friction factors from coarse to fine and medium to fine are 1.39 and 0.71 %, respectively. Therefore, the 20175527-mesh system was chosen quite dense in this study.

5.2.4 Boundary Condition and Data Reduction

Velocity inlet boundary condition was adopted with uniform velocity, water temperature constant value is 280 K, the pressure outlet boundary condition was utilized. The flow at the wall was assumed as no slip. The wall temperature is assumed to be constant and uniform at 291 K in the inner side of the tube. Outside of the tube was assumed as perfectly insulated; hence no heat loss to surroundings. The tested flow rate is 1 L/min (Re = 1028), 2 L/min (Re = 2057), 3 L/min (Re = 3086), 4 L/min (Re = 4115), and 5 L/min (Re = 5144). The equation of κ in the $\kappa - \omega$ turbulence model uses enhanced wall treatment in wall boundary conditions. This setting means that for all boundary conditions for fine mesh, Low-Reynolds-number treatment was utilized. To find out the strength of vortex, we use swirl strength (λ_{ci}). This method calculates strength of vortex based on the velocity gradient tensor. Swirl strength uses the imaginary portion of the complex eigenvalues of the velocity gradient tensor to describe vortices (ANSYS Academic Research, 2017; Holm´en, 2012).

The following equation calculates heat transfer rate of the coil

$$Q = \dot{m} c_p (T_o - T_i) \tag{5.6}$$

Where, T_o and T_i are bulk temperature on downstream and upstream crossection, respectively. Calculation of the average heat transfer coefficient is obtained as follows

$$h = \frac{Q}{\int_A dA\, \Delta T_m} \tag{5.7}$$

Where, ΔT_m is Logarithmic Mean Temperature Difference (LMTD) and T_w is wall temperature.

$$\Delta T_m = \frac{(T_w - T_o) - (T_w - T_i)}{ln\left(\frac{T_w - T_o}{T_w - T_i}\right)} \tag{5.8}$$

All water properties are assumed to be constant, so the use of LMTD calculations is valid.

Some dimensionless numbers are used in this study as follows

$$Re = \frac{\rho u d}{\mu} \tag{5.9}$$

$$Nu = \frac{hd}{\lambda} \tag{5.10}$$

$$f = \frac{\Delta p}{\left(\frac{l}{d}\right)\left(\rho \frac{v^2}{2}\right)} \tag{5.11}$$

To find out the critical of the Reynolds number of the coil, we use the Ito's correlation [19] as follows

$$Re_{cr} = 20000 \left(\frac{d}{D}\right)^{0.32} \tag{5.12}$$

Coefficient of Performance (COP) improvement factor, the derivation can be seen in equation 3.17, is utilized to evaluate DDIR-coil performance as follows

$$\frac{Q_C'}{Q_C} - \frac{V\,\Delta p}{Q_C}\frac{\Delta p'}{\Delta p} > 0 \tag{5.13}$$

Where, Q_C, Q_C', V, $\Delta p'$, and Δp are cooling rate (W/m), an increase of cooling rate (W/m), volumetric flowrate (m^3/s), an increase of pressure drop (Pa/m), and pressure drop (Pa/m), respectively. If left term is larger than 0, it means the ground heat exchanger performance increase. The base of COP improvement factor is heat transfer and pressure drop of smooth straight tube on several corelations.

A few Nusselt number and friction factor correlations were used in the turbulent, transition, and laminar regime to determine the heat transfer rate and pressure drop for

smooth straight tubes because the Reynolds number in this study was from 1028 to 5144. Critical Reynolds number for ribs pitch variation and ribs angle is 5332. Then, critical Reynold numbers for curvature 2.22, 2.66 and 3.33 m^{-1} are 5332, 5652, and 6071, respectively.

For laminar region, Nusselt number and friction factor were calculated as follows

$$\mathrm{Nu} = 3.66 \tag{5.14}$$

$$f = \frac{64}{Re} \tag{5.15}$$

Meanwhile, the calculation of the Nusselt number in the transition region adopted a linear interpolation method of the New Gnileniski Nusslet number (Gnielinski, 2013), which is valid at $2300 < Re < 4000$ and constant wall temperature.

$$Nu = (1-\gamma)Nu_{lam,2300} + \gamma Nu_{turb,4000} \tag{5.16}$$

Where

$$\gamma = \frac{Re - 2300}{2300 - 4000} \tag{5.17}$$

$Nu_{lam,2300}$ was calculated as follows

$$Nu_{m,T} = \left(Nu_{m,T,1}^3 + 0.7^3 + \left(Nu_{m,T,2} - 0.7\right)^3 + Nu_{m,T,3}^3\right)^{1/3} \tag{5.18}$$

Where,

$Nu_{m,T,1} = 3.66$,

$Nu_{m,T,2} = 1.615\sqrt[3]{Re\ Pr\ d/L}$,

$Nu_{m,T,3} = \left(\frac{2}{1+22\ Pr}\right)^{1/6} (Re\ Pr\ \ d/L)$

Then $Nu_{turb,4000}$ was calculated as follows

$$Nu = \frac{(f/8)(Re - 1000)Pr}{1 + 12.7\sqrt{f/8}(Pr^{2/3} - 1)}\left[1 + \left(\frac{d}{L}\right)^{2/3}\right]K \tag{5.19}$$

The K factor was described as

$$K = \left(\frac{Pr}{Pr_w}\right)^{0.11}$$

The friction factors in equation 5.19 use Konakov's friction factors as follows

$$f = (1.8\, Log_{10}Re - 1.64)^{-2} \quad (5.20)$$

Whereas in the transitional regime, Abraham friction factor (Abraham et al., 2011) that is valid Reynold number from 2300 to 4500 are used as follows

$$f = 3.03\, 10^{-12}Re^3 - 3.6710^{-8}Re^2 + 1.46\, 10^{-4}Re - 0.151 \quad (5.21)$$

For the turbulent regime, calculation the Nusselt number in equation 18 and the friction factor use Petukhov friction factors as follows

$$f = (0.79\, ln\, (Re) - 1.64)^{-2} \quad (5.22)$$

5.3 Result and Discussion

5.3.1 Model validation

We adopted some of the results of experiments conducted by Meng (2003) to validate numerical simulations as shown in Figure 5.4 and 5.5. The numerical results were following the experimental results on the f and $Nu/Pr^{1/3}$, Although there were some deviations. The average deviation between simulation and experimental results is 10.6 % for $Nu/Pr^{1/3}$ and 3.9 % for f. This deviation can be caused by the uncertainty of the experimental measurements and the difference between numerical and experimental methods. Accordingly, the numerical method used in the study of heat transfer and pressure drop is reliable.

5.3.2 Flow Structure and Heat Transfer

The behavior of the flow structure on DDIR-coil needs to be examined before discussing the results. The resulting flow analysis is an effective way of describing the flow in the DDIR-coil. Plain-coil is used as a comparison of how significant the effect

of DDIR-coil is on the flow structure. Figure 5.6 shows a three-dimensional flow display in the downstream coil area for Re = 4115.

In plain-coil, flow particles tend to occupy an outer side -coil position. The flow is caused by centrifugal force. This centrifugal force also causes some water particles near the wall to move towards the inner side of coil. In general, DDIR-coil produces two vortices when water particles pass through the ribs, namely the front vortex and the rear vortex.

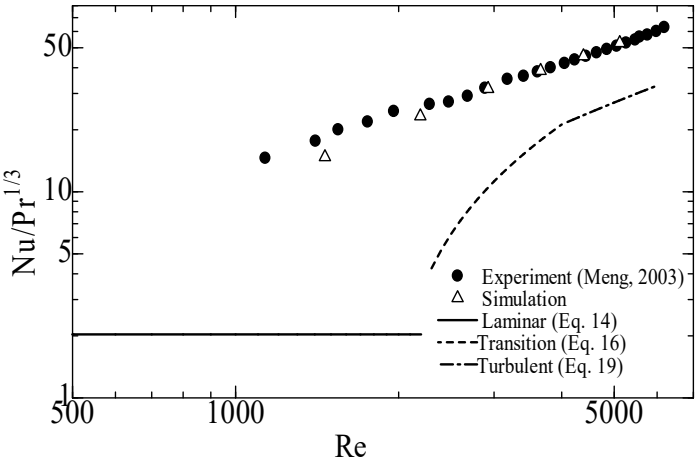

Figure 5.4. Comparison of $Nu/Pr^{1/3}$ between simulation results and experiment results for the proposed DDIR-straight tube.

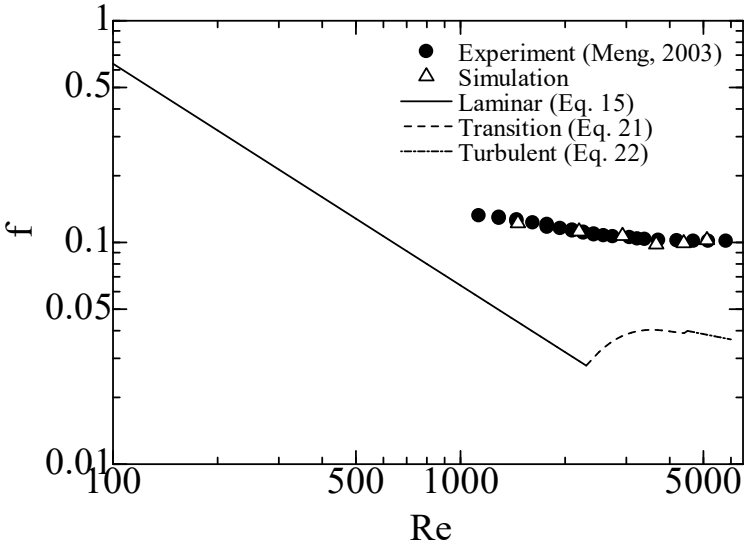

Figure 5.5. Comparison of friction Factors between simulation results and experiment results for the proposed DDIR-straight tube.

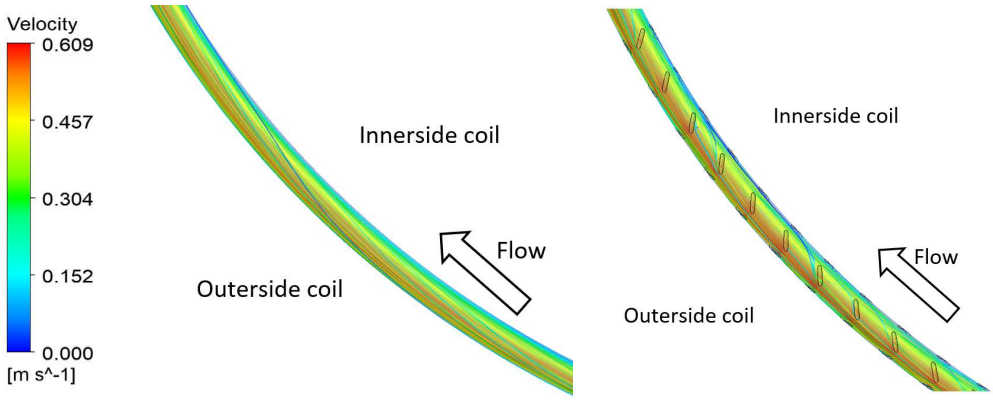

Figure 5.6. Limiting 3D isometric view streamline for Re = 4115 (a) MP-C3; (b) MR-C3

In DDIR-coil, flow particles tend to be distributed almost evenly both at inner side and outer side of coil. The ribs-induced flow is caused by force of the front vortex and rear vortex, which affect the centrifugal coil force. This phenomenon is confirmed by the tendency of water particle flow near the wall from outer side of coil to be distorted to outerside of coil several times when it crosses ribs before finally, the particle flow moves towards the inner side of coil. The path of water particles in DDIR-coil tends to be longer than that of plain-coil.

Tangential velocity and streamline observations are a remarkable way to determine the performance of DDIR effects in the flow field. Figure 5.7 shows the tangential velocity vector in the downstream coil. In plain-coil, the gradient velocity vector near the wall looks smaller than in DDIR-coil. Besides, the plain-coil location of the stagnation point and separation point tends to have a longer circumferential length than that of DDIR-coil. This tendency is possible because the flow generated by ribs can distort the flow so that it shifts the location of the stagnation point and the separation point. The DDIR-straight tube shows that there are two pairs of vortices in opposite directions. The velocity gradient was significant in the two pairs of vortexes. The stagnation point and flow separation are clearly symmetrical to each other.

Figure 5.8 shows a streamlined downstream coil. A pair of counter-rotating vortex is produced in both plain-coil and DDIR-coil. Based on research into the application of DDIR on straight tubes, the addition of ribs is accompanied by an increase in the number of longitudinal vortices (Zheng et al., 2015). This research conduct by using two pairs of V-type ribs on circumferential of tube. The generated vortex should be two

pairs. However, in this study, we found one pairs. No additional vortex appears because the vortex generated by the ribs joins the vortex caused by the centrifugal coil force.

This result is confirmed by the size of the vortex seen in the streamline. DDIR-coil tends to have a larger vortex size than that of plain-coil. On the DDIR-straight tube, two pairs of vortexes of similar size and flow patterns that appear dense are seen. This pattern indicates that the DDIR-stright tube pathway particles are longer than that of DDIR-coil and DDIR-plain. The quantitative increment of DDIR-coil in heat transfer from the side of fluid flow and heat transfer can be seen in Figure 5.11.

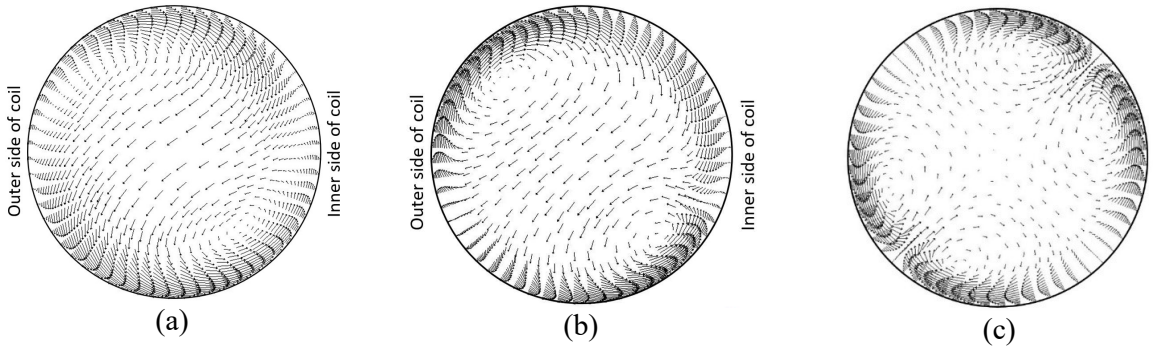

Figure 5.7. Tangential velocity vector in outlet test section for Re = 4115 (a) MP-C3; (b) MR-C3, (c) MR-S.

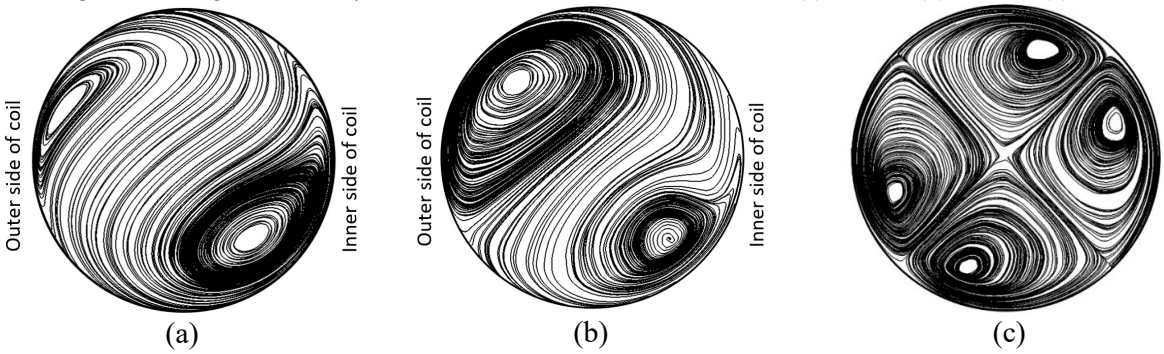

Figure 5.8. Streamlines in outlet test section for Re = 4115 (a) MP-C3; (b) MR-C3; (c) MR-S

The movement of the ribs-induced vortex with different types of shape is illustrated in Figure 5.9. Vortex core visual images are displayed based on iso-surface values of swirling strength of $40s^{-1}$. The structure of powerful vortexes is mostly constructed behind the ribs. The structure indicate that the strength of the rear vortex is greater than that of the front vortex. On DDIR-straight tube, the distribution of the vortex appears evenly on each ribs at the same circumferential perimeter. However, on

DDIR-coil, the vortex distribution is not the same in every ribs at one circumferential perimeter. This distribution is because the DDIR-straight tube primary flow and the ribs induced flow do not interfere with each other whereas the DDIR-secondary secondary flow and ribs induced flow interfere with each other.

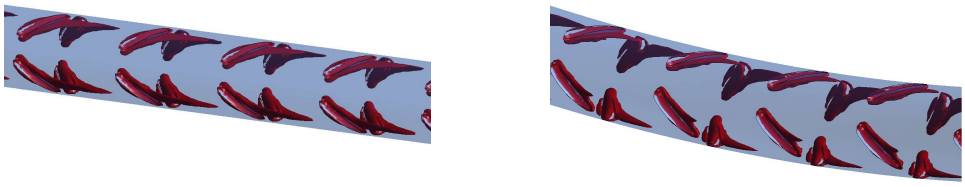

Figure 5.9. Vortex cores ($\boldsymbol{\lambda_{ci}}$ = 40s^{-1}) generated for Re = 4115 (a) MR-S; (b) MR-C3

Figure 5.10 shows the distribution of local heat transfer coefficient for Re = 4115 for DDIR-straight tube and DDIR-coil at the same axial length. It seems clear that the heat transfer coefficient of both DDIR-straight tube and DDIR-coil is much higher on the surface of the ribs; this is because the flow is incident directly onto the surface of the ribs.

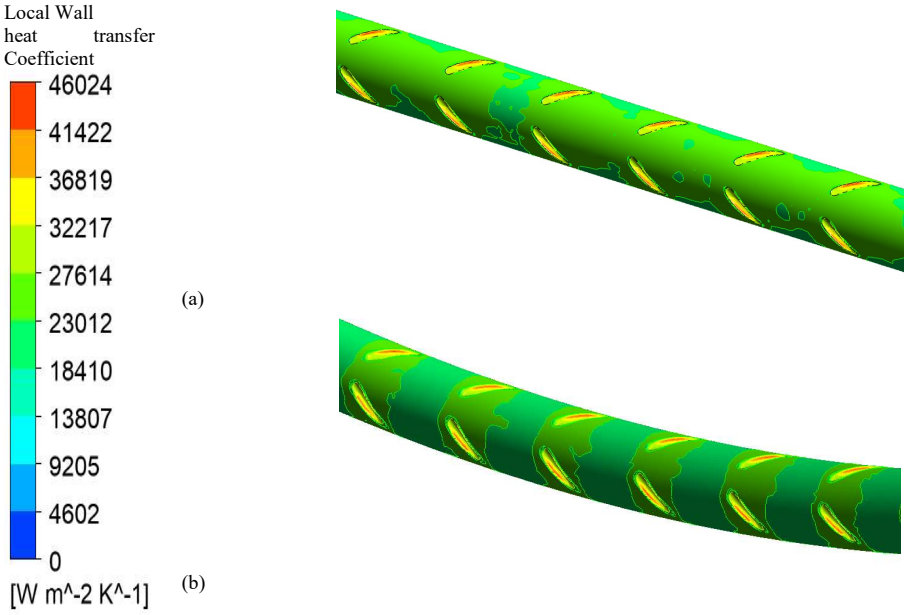

Figure 5.10**.** Local wall heat transfer coefficient contours on the wall of the test section for Re = 4115 (a) MR-S; (b) MR-C3

The local heat transfer coefficient was discovered somewhat higher at the rear ribs due to rear induced vortex. This phenomenon is caused by the strength of the rear vortex higher than that of the front vortex. However, it can be seen clearly that the local heat transfer coefficient is slightly higher in the DDIR-straight tube than that of in the DDIR-coil. DDIR-straight tube produces two flows, primary flow, and ribs induced flow. Meanwhile, DDIR-coil produces three flows, namely primary flow, secondary flow, and ribs-induced flow. Secondary flow and ribs-induced flow probably combine, then weakening the strength of the vortex; hence local heat transfer in DDIR-coil is slightly smaller than that of DDIR-straight tube.

5.3.3 Ribs Angle Effect

The variation of heat transfer rate, pressure drop and COP improvement factors with different rib angle and flowrate are shown in Figure 5.11 (a), (b) and (c). As can be seen, heat transfer and pressure drop increase with increasing flow rate. This increment may be due to increased flowrate that can generate greater windward, leeward, and higher swirl strength. An interesting pattern is shown by an angle of 20^{o} and 45^{o}. These two angles show almost a similar performance in both heat transfer and pressure drop in the range flowrate. A more detailed check shows that the 30 ^{o} angle has a slightly smaller heat transfer performance than that of the other angles. Whereas the pressure drop showed a more significant increase in each angle of the ribs. The increase in heat transfer is approximately 13.9%-25.15% and the pressure drop increases approximately 26.8%-89.5% over plain-coil. In Figure 5.11 (a), (b) and (c), heat transfer rate, pressure drop and COP improvement factor of straight DDIR-straight tube at 45^{o} ribs angle are also plotted. The straight tube is used as benchmark performance of DDIR-coil at 45^{o}. As mentioned above, DDIR is more effective in straight tube than coil. However, DDIR-coil is still more suitable for use in ground heat exchangers because the ground heat exchanger is installed in a trench and the coil has higher performance than that of straight tube in the same length of trench.

5.3.4 Curvature Effect

Figures 5.12 (a), (b) and (c) show the effect of the curvature of the DDIR-coil on the performance of heat transfer, pressure drop and COP improvement factors at a rib angle of 45^o and pitch rib of 22.5 mm in flowrate from 1 to 5 L/min. The graphs also illustrate plain-coil performance as a benchmark for increasing DDIR-coil performance. Commonly, decrease in curvature on DDIR-coil results in an increase in heat transfer rate and pressure drop.

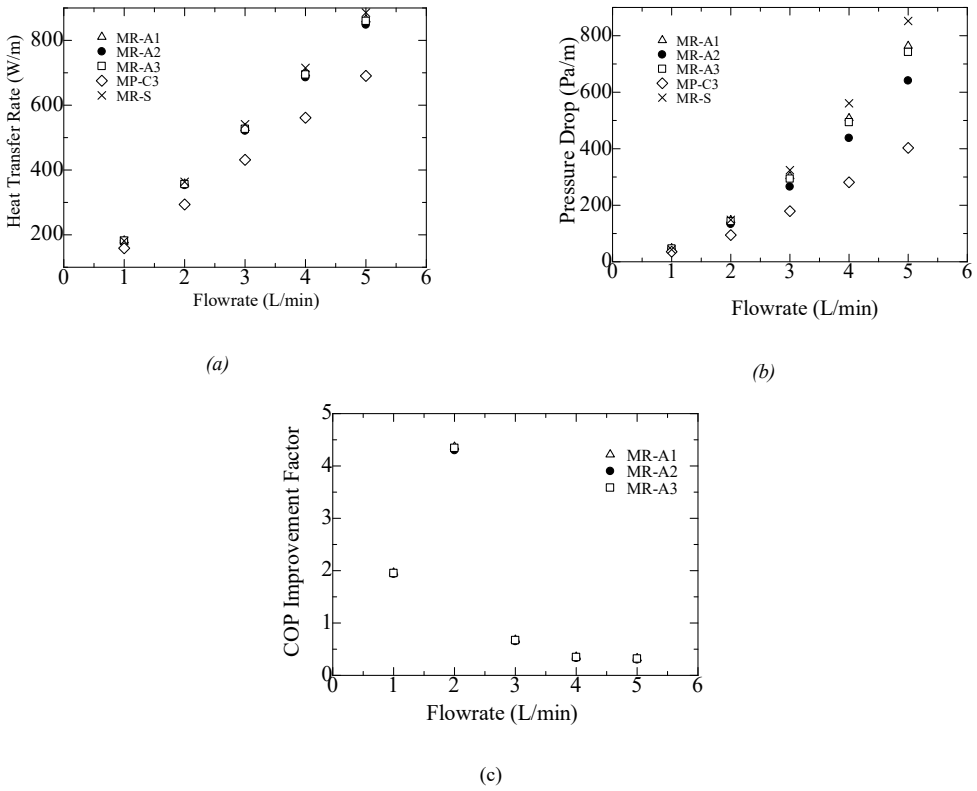

Figure 5.11. Performance Characteristics in Angle ribs variation (a) heat transfer rate; (b) Pressure; (c) COP Improvement Factor.

The decrease in curvature appears significantly at the heat transfer rate, but the decrease in pressure drop is very insignificant. The use of DDIR-coil shows more significant than that of plain-coil. The increase in heat transfer rate on curvature 2.22, 2.66, and 3.33 m^{-1} are 12.70-22.85%, 16.27-29.11%, and 14.50-24.51%, respectively. The increment in pressure drop on curvature 2.22, 2.66, and 3.33 m^{-1} are 27.28-80.45%, 28.87-82.81% and 30.83-84.17%, respectively. The value of COP Improvement Factors varies from 0.25-5.29. This trend shows that DDIR-coil provides benefits in terms of energy conservation. Although the heat transfer rate and pressure drop characters

increase with the increase in the curvature coil, the COP Improvement factor shows an interesting trend. The highest increase occurred at 2.22 $m^{-1,}$ and the lowest occurred at 2.66 m^{-1}. Dramatic increase and decrease of COP Performance factors in Curvature variations also happen at first flowrate. The COP Improvement Factors tend to change drastically in flow rate 1-3 L/min because the factors are calculated on equation 13-21 for straight tube Nusselt number and friction factors. The trend is triggered mainly flow on the straight tube in the transition regime. Hence, drastic change happens on this area.

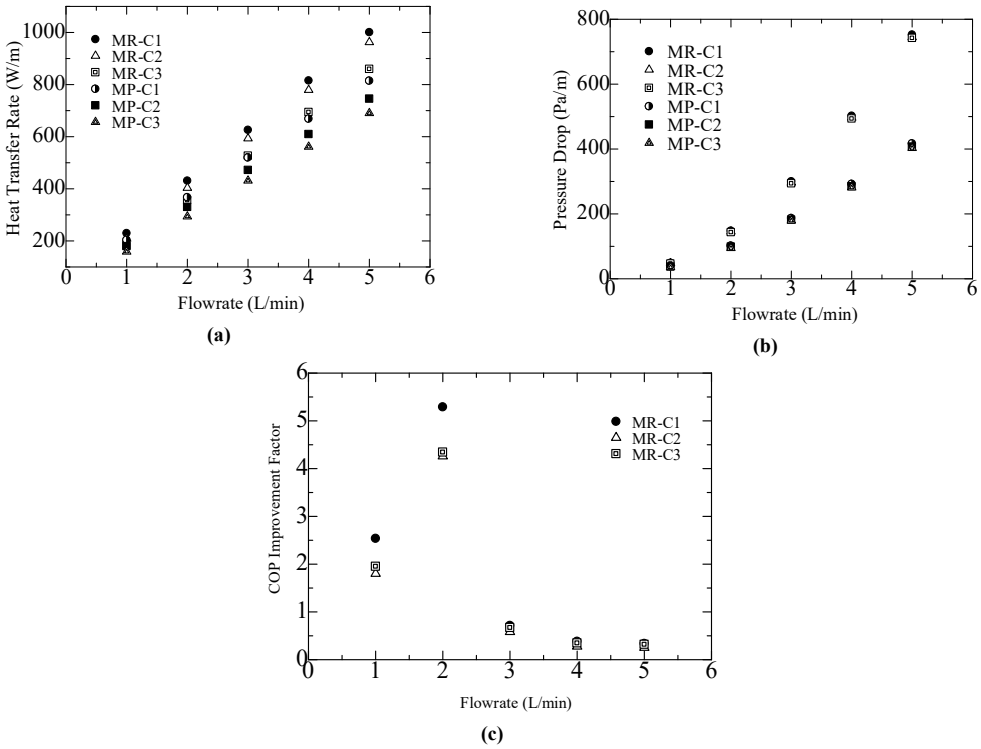

Figure 5.12. Performance Characteristics in Curvature variation (a) heat transfer rate; (b) Pressure Drop; (c) COP Improvement Factors

5.3.5 Ribs Pitch Effect

Figures 5.13(a), (b) and (c) show the effect of pitch ribs on the performance of heat transfer and flow at a rib angle of 45^o and axial coil length of 3533.75 mm. Pitch ribs are calculated based on the axial distance on the center coil. It is clear that the heat transfer rate and pressure drop slightly increased when pitch ribs increased. The reason for this phenomenon is that heat transfer increases more in the downstream ribs than that of upstream ribs, and increment ribs pitch decreases regions in downstream. Heat transfer and pressure drop increase, relative to plain coil, increases by 7.7 - 25.5% and

by 12.7 - 84.1 %, respectively. The COP Improvement Factor in pitch ribs varies between 0.19 to 4.34. It can be seen that the value of COP Improvement Factors increases with the decrease in distance between ribs on all flowrates. Significant increase in COP Improvement Factor at a flow rate of 1-2 L/min. Then there is a significant decrease in the flow rate of 2-3 L/min. Then, a decrease occurs slowly at a flow rate of 3-5 L/min. A sudden change in COP Factors that occurs at flow rates of 1-3 L/min occurs due to performance calculations occurring on a straight tube. At this flow rate, the flow is in the transition area so that the heat transfer and pressure drop have increased significantly. However, when it has passed the transition regime, tube performance tends to be more stable and turbulent enough so that straight tube performance approaches coil performance. This characteristic tends to result in a gradual decrease in COP Improvement factors at 3-5 L/min.

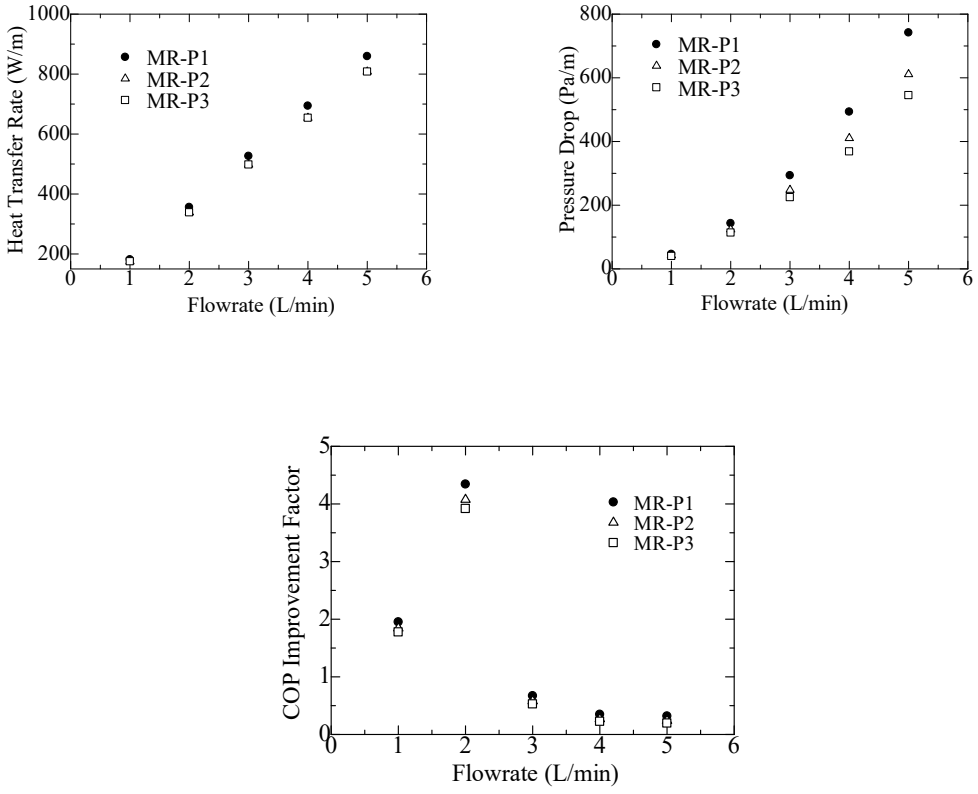

Figure 5.13. Performance Characteristics in ribs pitch (a) heat transfer rate; (b) Pressure Drop ; (c) COP Improvement Factor.

5.4 Conclusion

The results of the research on the effect of DDIR of Low curvature coil on increasing heat transfer, pressure drop, and COP Improvement factors are presented in this paper. The flow structure is described and analyzed. The influence of ribs angle, curvature, and ribs pitch are examined at a specific flowrate range so that the thermal and hydraulic characteristics of DDIR-coil are summarized as follows:

In the flowrate range investigated, DDIR-coil heat transfer increased from 7.7 to 29.11% bigger than that of plain-coil, and the pressure drop increased from 12.7 to 89.5% higher than that of plain-coil. COP Improvement factors approximately vary between 0.25 and 5.29.

The multiple longitudinal vortex arrangement in the DDIR-coil down stream is not apparent when compared to DDIR-straight. However, the Vortex local DDIR in coil is formed and has a strength similar to the vortex local DDIR in straight tube. The combination of secondary flow and ribs induced flow occurs so that the strength of the vortex in DDIR-coil tends to be higher than in plain coil. This phenomenon results in a relatively longer streamline and strong turbulence between the wall area and the core area, which increases heat transfer.

COP Improvement factors increase with decreasing pitch ribs. Ribs angle 20^{o} results in high COP Improvement Factors. Curvature coil 2.66 m^{-1} produces high COP Improvement Factors. The use of DDIR in low curvature coil / slinky-coil is recommended for practical applications of Ground Heat Exchanger, especially at low flowrate.

5.5 References

Abraham, J. P., Sparrow, E. M., & Minkowycz, W. J. (2011). Internal-flow Nusselt numbers for the low-Reynolds-number end of the laminar-to-turbulent transition regime. *International Journal of Heat and Mass Transfer*, *54*(1–3), 584–588. https://doi.org/10.1016/j.ijheatmasstransfer.2010.09.012

Acuña, J., & Palm, B. (2010). Comprehensive Summary of Borehole Heat Exchanger Research at KTH. *Conference on Sustainable Refrigeration and Heat Pump Technology. Stockholm, Sweden. June 2009*, p. 69. Retrieved from http://urn.kb.se/resolve?urn=urn:nbn:se:kth:diva-73137

Ali, M. H., Kariya, K., & Miyara, A. (2017). Performance analysis of slinky horizontal

ground heat exchangers for a ground source heat pump system. *Resources*, *6*(4), 1–18. https://doi.org/10.3390/resources6040056

ANSYSAcademicResearch. (2017). *Help System-Fluent Theory Guide, ANSYS*.

Ariwibowo, T H, Kuriyama, G., Kariya, K., & Miyara, A. (2019). Numerical Analysis of Thermo-Hydraulic Performance of Double Discrete Inclined Ribs on Curvature Coil in Laminar Flow for Ground Source Heat Pump System Application. *15th Asia Pasific Conference on Built Environment*, 7. Kaohsiung: ASHRAE REgion XIII.

Ariwibowo, Teguh Hady, Miyara, A., & Kariya, K. (2019). Consideration of Double Discrete Inclined Ribs in Low Curvature Coil for GSHP System. *International Journal of Sustainable and Green Energy*, *8*(3), 56–64. https://doi.org/10.11648/j.ijrse.20190803.12

Bouhacina, B., Saim, R., & Oztop, H. F. (2015). Numerical investigation of a novel tube design for the geothermal borehole heat exchanger. *Applied Thermal Engineering*, *79*, 153–162. https://doi.org/10.1016/j.applthermaleng.2015.01.027

Choi, H. K., Yoo, G. J., Pak, J. H., & Lee, C. H. (2018). Numerical study on heat transfer characteristics in branch tube type ground heat exchanger. *Renewable Energy*, *115*, 585–599. https://doi.org/10.1016/j.renene.2017.08.064

Chong, C. S. A., Gan, G., Verhoef, A., Garcia, R. G., & Vidale, P. L. (2013). Simulation of thermal performance of horizontal slinky-loop heat exchangers for ground source heat pumps. *Applied Energy*, *104*, 603–610. https://doi.org/10.1016/j.apenergy.2012.11.069

Gnielinski, V. (2013). On heat transfer in tubes. *International Journal of Heat and Mass Transfer*, *63*, 134–140. https://doi.org/10.1016/j.ijheatmasstransfer.2013.04.015

Hardik, B. K., Baburajan, P. K., & Prabhu, S. V. (2015). Local heat transfer coefficient in helical coils with single phase flow. *International Journal of Heat and Mass Transfer*, *89*, 522–538. https://doi.org/10.1016/j.ijheatmasstransfer.2015.05.069

Holm´en, V. (2012). Methods for Vortex Identification. https://doi.org/10.1016/s0166-218x(03)00180-x

Kuriyama, G., Ariwibowo, T. H., Kariya, K., & Miyara, A. (2019). Heat Transfer and Presser Drop Characteristics of Curved Tube with Discrete Ribs for Ground Source Heat Exchanger. *The 2019 Annual Conference of the Japan Society of Refrigerating and Air Conditioning Engineers*, 9–14. Tokyo: JSRAE.

Li, X. wei, Meng, J. an, & Guo, Z. yuan. (2009). Turbulent flow and heat transfer in

discrete double inclined ribs tube. *International Journal of Heat and Mass Transfer*, *52*(3–4), 962–970. https://doi.org/10.1016/j.ijheatmasstransfer.2008.07.027

Meng, J. A. (2003). *Enhanced Heat Transfer Technology of Longitudinal Vortices Based on Field-coordination Principle and its Application*. Tsinghua University.

Selamat, S., Miyara, A., & Kariya, K. (2016). Numerical study of horizontal ground heat exchangers for design optimization. *Renewable Energy*, *95*, 561–573. https://doi.org/10.1016/j.renene.2016.04.042

Teguh Hady Ariwibowo, Akio Miyara, K. K. (2019). Thermal and hydraulic performance simulation of curved tube with discrete ribs heat exchanger for ground source heat pump system. *Proceedings of 53rd Air Conditioning and Refrigeration Union Conference*, 17–20.

Wu, Y., Gan, G., Verhoef, A., Vidale, P. L., & Gonzalez, R. G. (2010). Experimental measurement and numerical simulation of horizontal-coupled slinky ground source heat exchangers. *Applied Thermal Engineering*, *30*(16), 2574–2583. https://doi.org/10.1016/j.applthermaleng.2010.07.008

Zheng, N., Liu, P., Shan, F., Liu, Z., & Liu, W. (2016). Effects of rib arrangements on the flow pattern and heat transfer in an internally ribbed heat exchanger tube. *International Journal of Thermal Sciences*, *101*, 93–105. https://doi.org/10.1016/j.ijthermalsci.2015.10.035

Zheng, N., Liu, W., Liu, Z., Liu, P., & Shan, F. (2015). A numerical study on heat transfer enhancement and the flow structure in a heat exchanger tube with discrete double inclined ribs. *Applied Thermal Engineering*, *90*, 232–241. https://doi.org/10.1016/j.applthermaleng.2015.07.009

CHAPTER

6

THERMAL CHARACTERISTICS OF DISCRETE DOUBLE INCLINED RIBS ON SLINKY COIL GROUND HEAT EXCHANGER

6.1 Introduction

In the last few decades, lack of energy, global warming, and air pollution are severe threats to the lives of living creatures in the world. The main trigger of global warming is carbon dioxide gas emissions mainly from fossil fuels (Alkaff et al., 2016). Several attempts have been made to reduce the impact of CO2 emissions by conserving energy ((Fay, 2002; Saboori et al., 2012; Yusof, 2011). To achieve this target, many researchers have focused on sustainable energy resources such as hydropower, geothermal energy (Guney, 2005), biomass, solar (Trieb et al., 2009), and wind (Herbert et al., 2007). Utilization of geothermal energy sources in the shallow grounds, Ground Source Heat Pump (GSHP) is a common alternative that is widely applied in various sectors in industries such as hot water production and heating or cooling air, both commercial and domestic buildings.

The use of GSHP results is efficient energy consumption so that the installation of GSHP increases from 10% to 30% every year in 30 countries lately. The main advantage of the GHSP system is the high coefficient of performance compared to conventional heat pumps. The main reason is that GSHP can use the ground as a heat sink in summer or heat source in winter (Metz, 1983; Piechowski, 1998, 1999). Generally, there are two types of GSHP, including open-loop systems using

groundwater or surface water directly and closed-loop systems with ground heat exchangers (Cavazza, 1981; D. Kirkham, 1972; Wu et al., 2010). The closed-loop system is divided into two types, namely vertical type and horizontal type, which is utilized depends on the geographical area and the availability of land.

An understanding of climate change and the thermal character of ground composition is essential in GHE installations. The design of the heat exchanger, which produces high thermal performance and is supported by the availability of land for installation, is taken into consideration. In addition, the GHE design has a balance between improved performance and financing costs.

Horizontal Ground heat exchangers are preferred when the GHE is viewed from the installation only buried between 1 to 2 meters from the ground surface. It does not require complicated equipment and skills in the GHE installation (Florides and Kalogirou, 2007). The balance of the use of GSHP in the summer and winter needs to be maintained. The ground thermal balance is vital for long terms usage of the GHE. The use of the GSHP system as a heater in winter is very profitable as a long-term investment (Badescu, 2007; Esen et al., 2006; Genchi et al., 2002).

Utilization of GSHP both in summer and winter season can reduce the cost of energy more than methane heating systems or conventional air-conditioners. Moreover, the GHSP system produces lower pollutant emissions (Esen et al., 2007; Esen et al., 2007; Inalli and Esen, 2004). The use of the GSHP system has been widely applied in developed countries, but efforts to promote the GSHP system are critical. A good slinky GHE design can attract small companies and homeowners to implement the GSHP system.

The design and strategy to improve the performance of Slinky GHE is very necessary to achieve these goals. Mostly, the slinky coil has curvature between 1.6 and 2.5 m^{-1}, which is considered as low curvature (Chong et al., 2013). Low curvature coil has similar characteristics as a straight tube in thermal and hydrodynamics (Bharadwaj et al., 2009; Han et al., 2013; Islam and Miyara, 2007; Islamoglu and Parmaksizoglu, 2003; Masao et al., 1988; Webb, 1981). Modification of the pipe surface results in a more turbulent flow structure besides increasing the heat transfer area [23-28]. Corrugated plastic pipes were found to be able to increase heat transfer in Earth-air heat exchangers (EAHE). Meanwhile, corrugated (Sakaya et al., 1980) and twisted (Dayton, 2011) tubes are used as heat transfer pipes for heat transfer at ground level.

GHE from high thermal conductivity materials such as copper can produce improved thermal performance compared to plastic pipes. At EAHE (Santamouris et al., 1995), the use of copper pipes has been widely used. Copper pipes have high reliability for up to 50 years of operation. However, copper pipes have a disadvantage, such as corrosion when the pipe buried in the ground. Nowadays, composite copper pipes are a good alternative for replacing pure copper and are commercially available. Composite copper ensures durability where the pipe is coated with a protective layer on hard ground. However, the use of this additional layer is not expected to reduce GHE thermal performance. A combination of modified slinky pipe and high thermal conductivity pipe coating material can drive this goal.

Discrete Double Inclined Ribs (DDIR) tube is recommended to obtain heat transfer enhancement as a longitudinal vortex generator by several researchers (Li et al., 2009; Li et al., 2007; Meng et al., 2005; Zheng et al., 2015). They stated that the DDIR tube could carry out energy saving due to heat transfer enhancement that is greater than the energy loss due to pressure drop. We have conducted several studies on the effect of using DDIR on the thermal performance of the Slinky coil under ideal and steady-state assumptions. Based on our findings, DDIR has the potential to increase the performance of the Slinky coil (Ariwibowo et al., 2020; Ariwibowo et al., 2019a; Ariwibowo et al., 2019b; Kuriyama et al., 2019; Ariwibowo and Miyara, 2019). In this research, we would like to clarify the performance application of DDIR to the thermal performance of slinky-coil GHE in transient conditions.

6.2 Materials and Methods

6.2.1 Model Descriptions and Governing Equations

The computational domain is 3 dimensional with a size of 6 m x 1.4 m x 5 m, as seen in Figure 6.1 (a). Due to computational limitations, the analysis is only one loop. Slinky GHE is buried 1.5 meters from the ground surface. Then, the detailed geometry of the pipe can be seen in Figure 6.1 (b) slinky coil loop GHE consists of 2 straight tubes and a coil. The straight pipe is installed on the upstream and downstream of the coil. The length of the straight tube and coil tube is 0.7 m and 3.1 m, respectively. The total axial length of one loop is 4.5 m. The slinky coil diameter (D), coil pitch (P_C), and the straight pipe is 1 m, 100 mm and 700 mm, respectively. The angle of ribs (α), axial ribs pitch (P_R), and ribs height (T) are 45^o, 22.5 mm, and 1 mm, respectively.

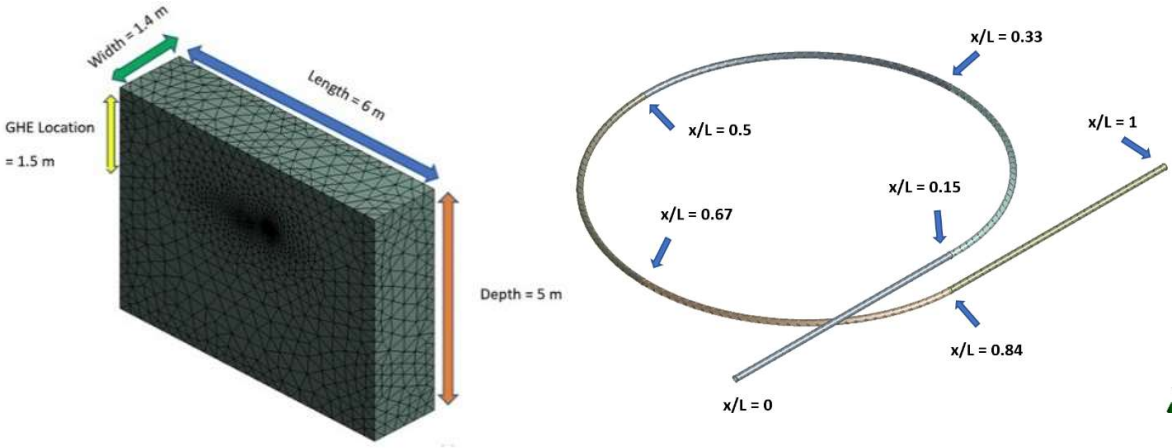

(a) (b)

Figure 6.1. (a) Schematic diagram of the general computational domain; (b) General view of the waterside computational domain and several cross-sections of the GHE for data collection

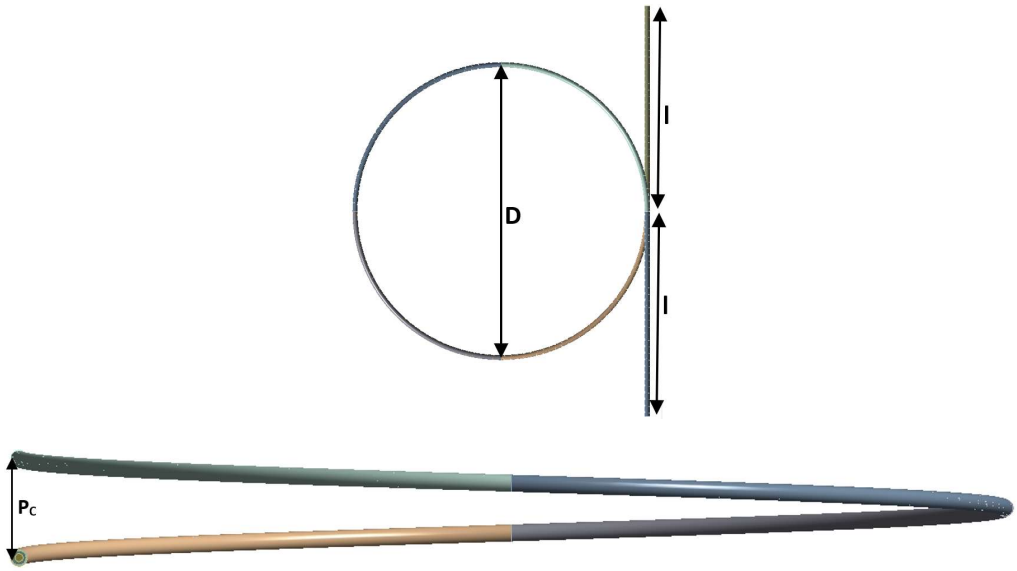

(a)

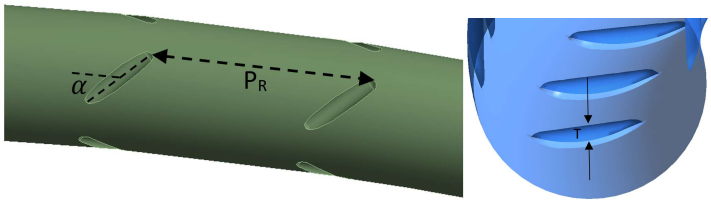

(b)

Figure 6.2. Configuration of DDIR-coil (a) Top view and side of coil, (b) Location of ribs inside and outside coil surface.

This simulation uses ground at Saga University, Saga City, Japan. The topsoil layer is soft Ariake clay soil, which has a thickness of between 10 to 20 meters with a maximum value of 30 meters. Natural water content is 12 to 173% (Khamehchiyan and Iwao, 1994). Soil samples were taken in the Saga City Fukudomi area, which consisted of clay from ground level to a depth of 15 m, sand, and sandy-clay from 15 to 20 meters and a water content of 30 to 150% which varied at different depths (Hino et al., 2007). In this research, our concern in only 5-meter depth from the top ground surface; hence we simulate heat transfer on clay. The thermophysical properties of clay can be seen in table 6.2. Sandy clay and sand are also tested to see the impact of ground thermal conductivity on GHE performance.

Table 6.1. Pipe sizing and thermophysical properties materials.

Pipe material	**Inner diameter (mm)**	**Wall thickness (mm)**	**Density (kg/m^3)**	**Specific heat (J/kg·K)**	**Thermal conductivity (W/m·K)**
Composite:					
Copper (inner)	14.9	0.65	8978	381	387.6
LDPE (outer)	-	0.59	920	3400	0.34
Copper	14.9	1.24	8978	381	387.6
HDPE	14.9	1.24	955	2300	0.41

The main geometry and detailed meshing in the cross-section of GHE can be seen in Figure 6.3. The computational domain is divided into three main parts, namely water and pipe, ground interface, and main ground. Meshing water and side pipes are less than 1 millimeter in size, while the main ground has a mesh size of 0.25 meters, so a ground interface is needed, which is used as a link between the mesh in the water and pipe domain with the main ground. The plain coil total mesh is 24987160 elements, and the ribs coil total mesh is 33432535 elements.

Table 6.2. The properties of ground (*JSME Data Book: Heat Transfer*, 2009)[42].

Parameters	Density (kg/m^3)	Heat Capacity (J/kg·K)	Thermal Conductivity (W/m·K)
Clay (water content: 27.7%)[1]	1700	1800	1.2
Sandy Clay (water content: 21.6%)[1]	1960	1200	2.1
Dry Sand (water content: 0 %)[2]	1815	620	0.3

[1] Taken from JSME Hand book [42] , [2]Taken from Hailu et al. [49]

Flow simulation uses the Reynolds average Navier-Stokes (RANS) equation. This transient simulation solves the case of heat transfer and turbulent flow. In this case, the energy transport equation is used to solve the phenomenon of convection on the side of the water flow and conduction on the ground side around GHE.

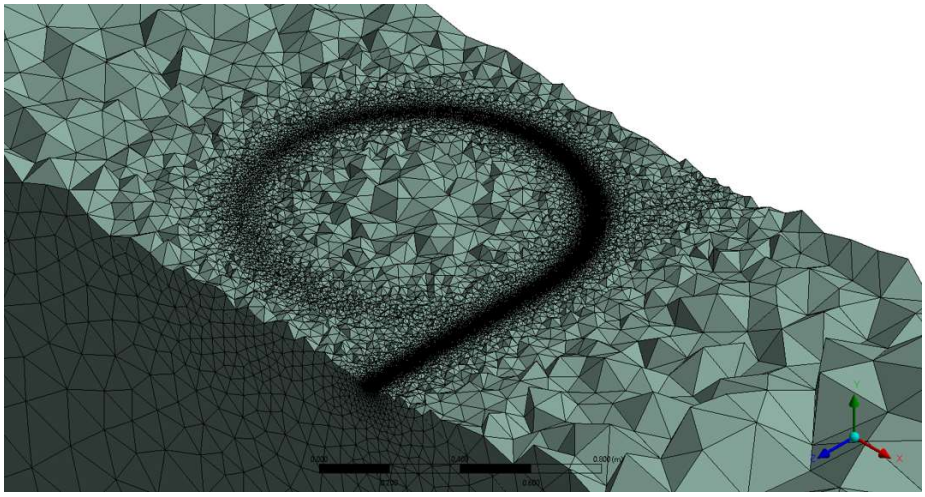

Figure 6.3. Mesh structure on the coil and surrounding ground

The κ-ω SST turbulence model is utilized. To obtain more accurate results, the value of y^+ is 1. The time step used in the transient analysis was in a minute basis. The details of the momentum equation, continuity, energy transport in the fluid zone are shown as follows

Continuity Equation

$$\frac{\partial(\rho u_i)}{\partial x_i} = 0 \tag{6.1}$$

Momentum Equations

$$\frac{\partial(\rho u_i)}{\partial t} + \frac{\partial(\rho u_i u_j)}{\partial x_j} = -\frac{\partial p}{\partial x_i} + \frac{\partial}{\partial x_j}\left(\mu \frac{\partial(u_i)}{\partial x_j} - \rho\overline{u'_\iota u'_J}\right) \tag{6.2}$$

Energy Equations

$$\frac{\partial}{\partial x_i}(\rho T) + \frac{\partial}{\partial x_i}(\rho u_i T) = \frac{\partial}{\partial x_i}\left(\frac{\lambda}{c_p}\frac{\partial T}{\partial x_i}\right) \tag{6.3}$$

Turbulence Kinetic Energy Equation

$$\frac{\partial(\rho\kappa)}{\partial t}+\frac{\partial(\rho u_i\kappa)}{\partial x_i}=\tilde{P}_\kappa-\beta^*\rho\kappa\omega+\frac{\partial}{\partial x_i}\left((\mu+\sigma_\kappa u_t)\frac{\partial\kappa}{\partial x_i}\right) \tag{6.4}$$

Specific dissipation rate equation

$$\begin{aligned}\frac{\partial(\rho\omega)}{\partial t}+\frac{\partial(\rho u_i\omega)}{\partial x_i}&\\ =\varphi\rho S^2-\beta\rho\omega^2+\frac{\partial}{\partial x_i}\left((\mu+\sigma_\omega u_t)\frac{\partial\omega}{\partial x_i}\right)&\\ +2(1-F_1)\rho\sigma_{\omega^2}\frac{1}{\omega}\frac{\partial\kappa}{\partial x_i}\frac{\partial\omega}{\partial x_i}&\end{aligned} \tag{6.5}$$

Whereas the energy transport equation in the ground side is described as follows

$$\rho_s C_p\frac{\partial T}{\partial t}=\nabla.(k\nabla T) \tag{6.6}$$

All equations are solved using ANSYS FLUENT 17.2, which is based on the finite volume method. All of the constant and parameters of equations can be seen in ANSYS Manual (2017). Swirl strength (λ_{ci}) is utilized to find out the strength of the vortex. In this method, the strength of the vortex is calculated based on the velocity gradient tensor. Swirl strength uses the imaginary portion of the complex eigenvalue of the velocity gradient to interpret vortices (ANSYS Manual, 2017; Holm´en, 2012).

6.2.2 Boundary condition, Initial Condition and Data Reduction

A constant and uniform temperature of 29 ^{o}C is used at the top ground surface. In the bottom ground section, a constant heat flux of 65 mW/m^2 was used (Pollack et al., 1993). For Temperature profile up to a depth of 5 m, we use experimental data on July 1, 2016, at Saga University, Japan (Ali et al., 2017). For cooling mode, the initial conditions of temperature distribution on the ground are assumed to be the same as the temperature profile on the experiment. Temperature boundary conditions of far-field vertical grounds are set as constant temperature, while boundary conditions of ground that are close to GHE are set as adiabatic. Analysis of the domain uses the temperature distribution profile using the equation illustrated in Figure 6.4.

$$T_y = 0.0148\,y^4 + 0.3366\,y^3 + 2.6865\,y^2 + 9.3082\,y + 29.62 \tag{6.7}$$

Velocity inlet and outflow are used as boundary conditions for inlet and outlet. Inlet water is assumed to be uniform velocity and a constant temperature of 27 °C. Determination of the critical Reynolds number for flow in the coil using the Ito's correlation (Ito, 1959) as follows

$$Re_{cr} = 20000\left(\frac{d}{D}\right)^{0.32} \tag{6.8}$$

According to the geometry size of the coil, the critical Reynolds number for the coil in this study is 5171. Based on Recr, the flowrate 2 L/min is a laminar flow with Re = 3406, and flowrate 4 L/min is a turbulent flow with Re = 6812.

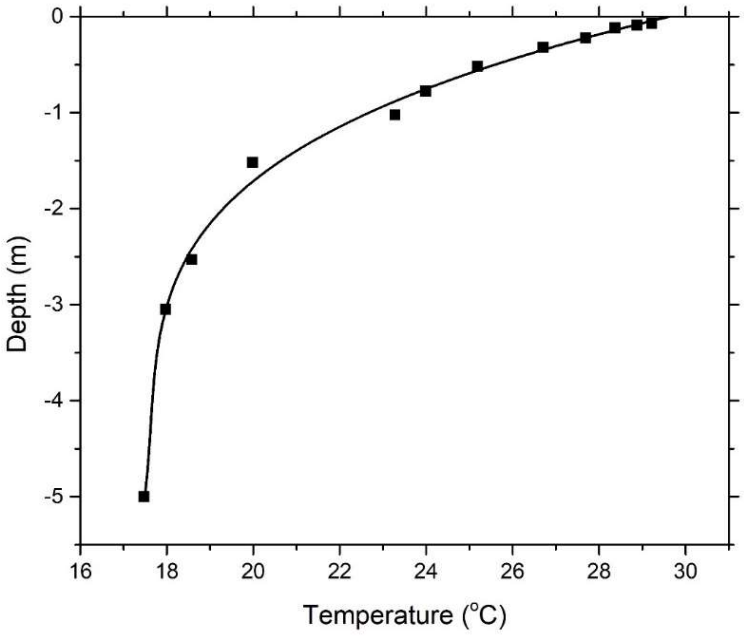

Figure 6.4. Ground temperature profile for Initial Condition (Ali et al., 2017).

The heat transfer rate is calculated using the following equation:

$$Q = \dot{m}C_p\,(T_o - T_i) \tag{6.9}$$

where $\dot{m}$, Cp, Ti and To are flow rate of water (kg/s), the specific heat of water (J/(kg·K)), inlet and outlet temperatures of water, respectively. The heat transfer rate of the axial length of the coil or trench length can be calculated using the following equation:

$$\bar{Q} = \frac{Q}{L} \tag{6.10}$$

The following equations calculate local heat transfer coefficient

$$\lambda = \frac{Q^{"}}{(T_b - T_w)} \tag{6.11}$$

Where, $Q^{"}$, T_b, and T_w are heat flux (W/m^2), bulk temperature (^{o}C), and wall temperature (^{o}C), respectively. Heat flux and wall temperatures were taken from average value on the perimeter of the coil.

Table 6.3. Simulation conditions and fluid flow regime for all of the simulation models

Case	Flow rate (L/min)	Pipe Material	Type	Flow regime[1]	Ground
Case 1	2	Composite	Plain-coil	Laminar[1]	Clay
Case 2	2	Composite	DDIR-coil	Laminar[1]	Clay
Case 3	4	Composite	Plain-coil	Turbulent[1]	Clay
Case 4	4	Composite	DDIR-coil	Turbulent[1]	Clay
Case 5[3]	2	Composite	DDIR-coil	Laminar[1]	Clay
Case 6	2	Copper	Plain-coil	Laminar[1]	Clay
Case 7	2	Copper	DDIR-coil	Laminar[1]	Clay
Case 8	2	HDPE	Plain-coil	Laminar[1]	Clay
Case 9	2	HDPE	DDIR-coil	Laminar[1]	Clay
Case 10	2	Composite	Plain-straight	Turbulent[2]	Clay
Case 11	4	Composite	Plain-straight	Turbulent[2]	Clay
Case 12	2	Composite	Plain-coil	Laminar[1]	Sand
Case 13	2	Composite	DDIR-coil	Laminar[1]	Sand
Case 14	2	Composite	Plain-coil	Laminar[1]	Sandy Clay
Case 15	2	Composite	DDIR-coil	Laminar[1]	Sandy Clay

[1]Critical Reynolds number is calculated based on Equation (6.8), [2]Critical Reynolds number is 2300, [3]intermittent mode

To understand the improvement of GHE modification to the GSHP system, we use net coefficient of performance, COP_{net_cool} as follows

$$COP_{net\_cool} = \frac{Q_C}{L_{comp} + L_{pump}} = \frac{Q_H - L_{comp}}{L_{comp} + L_{pump}} \tag{6.12}$$

Where, Q_H and Q_C are cooling and heating rate, $L_{comp}$and L_{pump} are power input

to the compressor and pump, respectively. If DDIR-coil increase the heating rate by Q'_H and pumping power by L'_{pump}, the net heating COP becomes

$$COP'_{net\_cool} = \frac{COP_{net\_cool} + Q'_H/(L_{comp} + L_{pump})}{1 + L'_{pump}/(L_{comp} + L_{pump})} \quad (6.13)$$

The compressor power (L_{comp}) is assumed as constant. By using $COP_{net\_cool} < COP'_{net\_cool}$, then the following equation is obtained

$$COP_{net\_cool} < \frac{COP_{net\_cool} + Q'_H/(L_{comp} + L_{pump})}{1 + L'_{pump}/(L_{comp} + L_{pump})} \quad (6.14)$$

Improvement of the system can be achieved with following equation

$$Q'_H > L'_{pump} \quad (6.15)$$

The pumping power is given as product of volumetric flowrate V (m^3/s) and pressure drop, Δp (Pa).

$$L_{pump} = V\,\Delta p, L'_{pump} = V\,\Delta p' \quad (6.16)$$

From equation 6.15 and 6.17, the following equation is obtained

$$\frac{Q'_H}{Q_H} - \frac{V\,\Delta p}{Q_H}\frac{\Delta p'}{\Delta p} > 0 \quad (6.17)$$

Where Q_H, Q'_H, V, Δp, and $\Delta p'$, are heating rate (W/m), an increase of heating rate (W/m), volumetric flow rate (m^3/s), pressure drop loss (Pa/m), and increase of pressure loss (Pa/m), respectively.

6.3 Result and Discussions

6.3.1 Model Validation

Figure 6.5 shows the heat transfer rate from experimental and simulated data. The experimental data are taken from previous experiment at Saga University (Ali et al., 2017). Due to the lack of experimental data, in this validation, experimental data are taken starting from the 99th minute of the beginning operation. In experiments, the inlet temperature fluctuates, so the heat transfer rate of the experiment fluctuates slightly. It can be seen in the figure 6.5 that the simulation and experimental data trends are the same and have almost the same value. The average deviation between the results of the experiment and the simulation is 7%.

6.3.2 Pre-analysis

Pipe configuration and curvature affect flow characteristics in GHE are important to understand the GHE performance. Therefore, pressure drop is observed in several pipe configurations. Simulation results show pressure drop in case 1 and case 2 are 219 Pa/m and 395 Pa/m, respectively. Meanwhile, cases 3 and 4 are 676 Pa/m and 1431 Pa/m, respectively. The straight plain, used as a pressure drop reference in calculating the COP improvement factor, has pressure drops for cases 10 and case 11 are 65 Pa/m and 205 Pa/m, respectively.

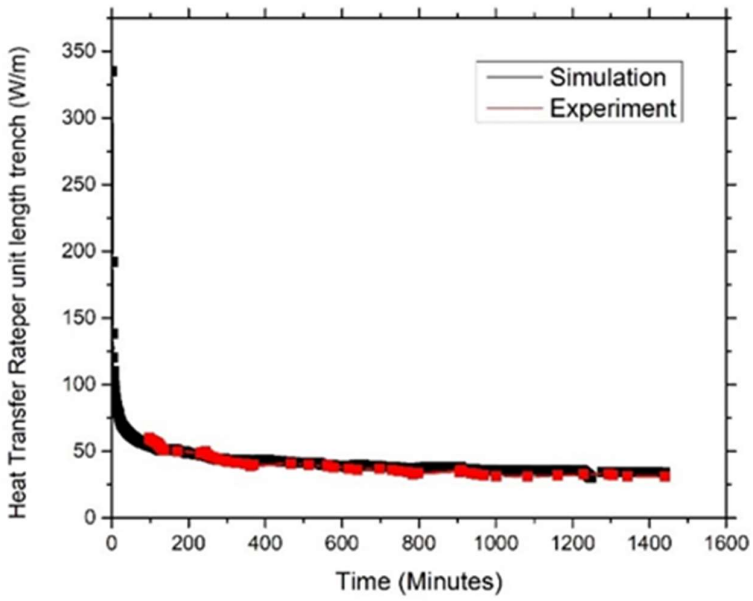

Figure 6.5 Comparison of heat transfer rate per unit trench length between simulation and experimental results

6.3.3 Flow structure

The flow structure characteristics of ribs coil and plain coil need to be investigated before discussing the results. This flow analysis is quite useful to describe the flow in the coil, such as in Figure 6.6 and 6.7. Figure 6.6 shows a 3D streamline on plain and ribs coil in case 1 and 2. On a plain coil, the high-velocity fluid particles occupy the location of the outer side of the coil. This phenomenon is caused by centrifugal force. This force also causes some water particles near the wall to move to the innerside section. In ribs coil, high-velocity fluid particles are almost uniformly distributed throughout the domain. The flow generated by ribs interferes with the

centrifugal force of coil. This incident causes the tendency of the flow of water particles to move distorted towards the outside coil before finally going to the innerside coil. Thus, the air particle path in the ribs coil is further than that of the plain coil.

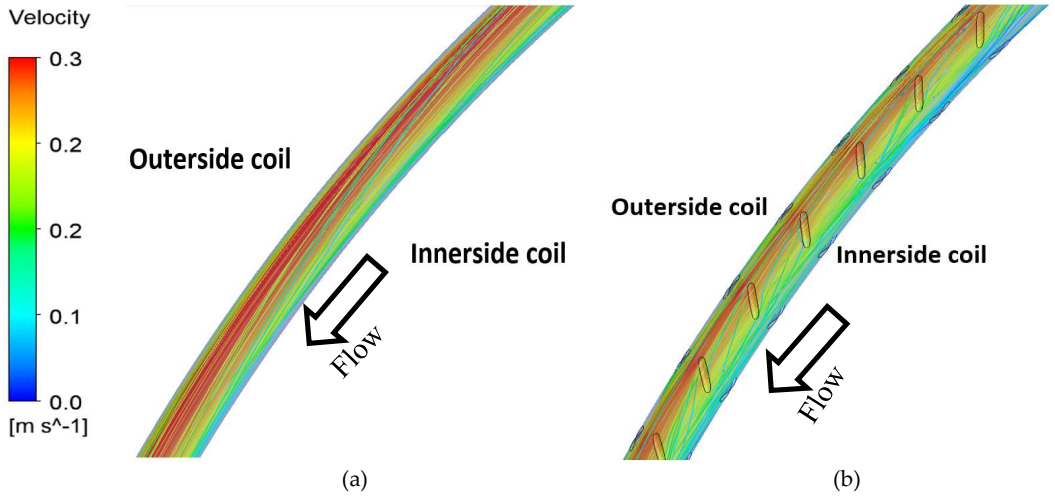

Figure 6.6. top view of streamline on downstream coil for Re = 3406 (a) Case 1; (b) Case 2.

The result is supported by the strength of the vortex on the plain coil and ribs coil. In plain coil, the vortex is only produced by secondary flow of the coil so that the vortex strength produced is only $3.7s^{-1}$, as shown in Figure 6.7. On this coil, the vortex is collected on the innerside. The fluid moves to the innerside coil due to centrifugal force. Then two flow near-wall perimeter collide each other, which leads to separation in innerside. Meanwhile, on ribs coil, vortex is generated by a combination of secondary flow and flow generated by ribs, so that vortex strength is 16.2 s^{-1} where this value is higher than that of in plain vortex coil. Vortex location tends to be around ribs, especially in the rear ribs.

6.3.4 Rib effect on Heat transfer rate

The effect of composite coil surface on the value of heat transfer in case 1, 2, 3, and 4 can be seen in Figure 6.8. Mostly, the heat transfer rate has peaked during the initial operation. Then, along with the increase in operating time, thermal performance starts to decline before it begins to decrease until the operation stops gradually. The GHE releases heat to the ground causing changes in the temperature of the surrounding ground during operation. The temperature difference between the ground and GHE decreases so that the amount of heat transfer decreases as the ground begins to heat up. This incident caused the heat transfer rate to drop dramatically due to the influence of dominant heat

accumulation. Heat spreads to the surrounding ground; thus, the heat transfer rate continues to decrease at a low rate.

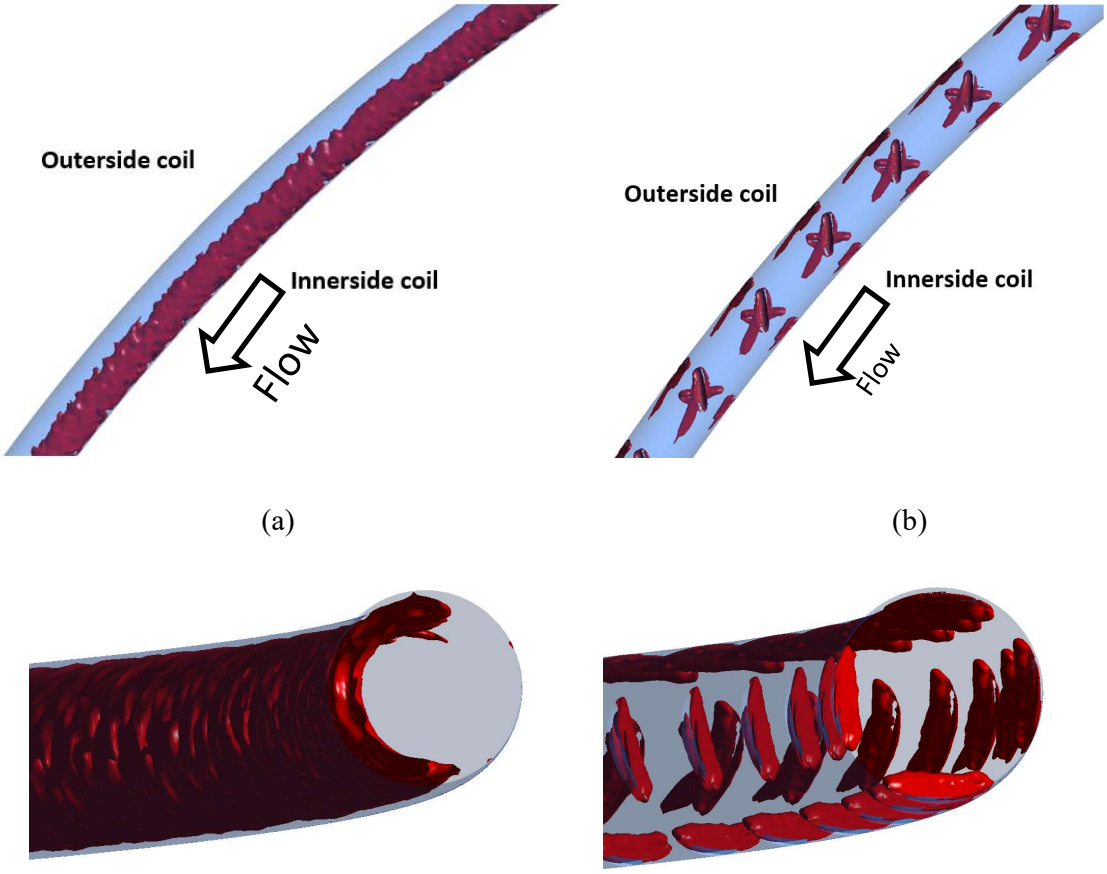

Figure 6.7. Vortex strength generated for Re = 3406 (a) top view of case 1 with λ_{ci} = 3.7s^{-1} ; (b) top view of case 2 with λ_{ci} = 16.2s^{-1} ; (c) cross-sectional view of case 1 with λ_{ci} = 3.7s^{-1}; (d) cross-sectional view of case 2 with λ_{ci} = 16.2s^{-1}

Based on the turbulent analysis, ribs coil has a higher performance than plain coil in the first 149 minutes. In turbulent flow, the heat transfer in the 30th minutes for Plain coil and ribs coil is 70.89 W/m and 71.30 W/m, respectively. Then in the 60th minute, the plain coil and ribs coil obtain heat transfer rates are 62.00 W/m and 62.29 W/m, respectively. In the 149th minute, the plain coil and ribs coil heat transfer rates are 52.32 W/m and 52.34 W/m, respectively. The ribs coil heat transfer rate tends to be lower than the plain coil after the 149th minute until the last minute. On the other side, heat transfer performance on ribs coil larger than plain coil from the beginning until the

end of time in laminar flow. In laminar flow, the heat transfer in the 30th minutes for Plain coil and ribs coil is 67.94 W/m and 69.10 W/m, respectively. Then in the 60th minute, the plain coil and ribs coil heat transfer rates are 59.17 W/m and 60.08 W/m, respectively. In the 149th minute, the plain coil and ribs coil heat transfer rates are 50.02 W/m and 50.63 W/m, respectively.

In turbulent flow, the ribs coil rejects heat in the ground higher than that of the plain coil at the beginning of the GHE operation. This phenomenon causes the heat of the ground around GHE to experience a faster heating process than that of the plain coil. The ground is not able to provide enough thermal recovery, so the ribs coil performance becomes low after 149 minutes. On the other hand, the ribs coil tends to reject heat in the ground is not too large at the beginning of the GHE operation on the laminar flow. This phenomenon causes heat accumulation in the ground to increase more slowly than that of turbulent flow. So the ribs coil performance is still superior to the plain coil in the operation time.

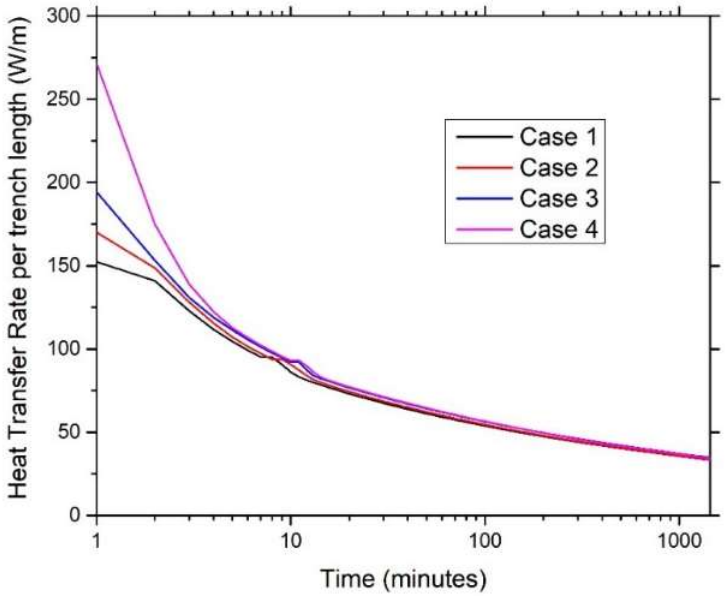

Figure 6.8. Comparison of heat transfer rate performance on plain coil and ribs coil

Based on this phenomenon, it can be stated that the effect of ribs coil on turbulent flow has no significant increase in heat transfer rate compared to plain coil. On the flow structure analysis of the ribs coil, the vortex strength is about four times larger than that of the plain coil. This flow structure should produce better thermal mixing. In figure 6.8, ribs coils do not show significant thermal performance. This phenomenon is caused by limited ground thermal conductivity.

The performance shows that the heat transfer rate is dominated by the effect of heat transfer on the ground side. The use of fin on the ground side, which is proposed by Saeidi et al. (2018), might be a promising option to help increase heat transfer on the ground side to solve the problem in turbulent flow ribs coil. On the other hand, on laminar flow, ribs coil shows higher performance than plain coil. However, continuous operation allows a decrease in performance in a long time. Therefore, intermittent operating methods are an alternative option to obtain ground thermal recovery, as mention in Selamat et al. (2015). The intermittent option is investigated in section 6.3.6.

The average heat transfer rate was observed to evaluate the effect of pipe modification on GHSP system performance. Case 1 and case 2 have an average heat transfer rate of 40.79 W/m and 41.09 W/m, respectively. Whereas the average heat transfer rate for case 3 and case 4 is 42.52 W/m and 42.41 W/m, respectively. Straight plain, used to reference the COP improvement factor calculation, has an average heat transfer rate in case 10 and case 11 is 13.78 W/m and 14.71 W/m. COP improvement factors can be seen in Table 6.4.

Table 6.4. The criterion of COP Improvement Factor defined in Eq 6.17

GHE	$Q_{H\text{-}c}$	$Q_{H\text{-}s} = Q_H$	$\boldsymbol{Q'_H}$	V	$\Delta \boldsymbol{p_c}$	$\Delta \boldsymbol{p_s} = \Delta \boldsymbol{p}$	$\Delta \boldsymbol{p'}$	Eq 6.17
	W/m	W/m	W/m	m^3/s	Pa/m	Pa/m	Pa/m	
Case 1	40.79	13.78[a]	27.01	3.333E-05	219	65[a]	154	1.96
Case 2	41.09	13.78[a]	27.31	3.333E-05	395	65[a]	330	1.98
Case 3	42.52	14.71[b]	27.81	6.666E-05	676	205[b]	471	1.89
Case 4	42.41	14.71[b]	27.70	6.666E-05	1431	205[b]	1226	1.88

[a]average heat transfer rate and pressure drop on straight tube at 2L/min, [b]average heat transfer rate and pressure drop on straight tube at 4 L/min

For the COP improvement factor calculation, the calculation only focuses on case 1 to case 4. In these cases, cases 1 and 3 are plain coil variations at flowrate 2 and 4 L/min, respectively and cases 2 and 4 are DDIR-coil variations in flowrate 2 and 4 L/min, respectively. The calculation of COP improvement factors is evaluated based on the performance of cases 10 and 11 which are plain-straight with a flowrate of 2 and 4 L/min, respectively. All cases for the COP Improvement factor evaluation use composite pipe material. Based on the pressure drop and heat transfer rate of GHE the COP improvement factors described in Table 6.3. In this section, COP improvement

factor is used to evaluate the performance of GHE modifications to the GHSP system. The values obtained from equation (15), as listed in table 6.4 is always positive. DDIR-coil proved to be effective with a COP improvement factor of 1.98 on laminar flow.

6.3.5 The First 60 minutes Operation Analysis

Phenomena at the first 60 minutes operation are necessary to understand behavior of the GHE operation, which is mentioned in part 3.3, as shown in Figure 6.9. In this section, bulk temperature, wall temperature, heat flux, and heat transfer coefficient along coil length are analyzed to understand the first 60 minutes phenomena. In this section, the analysis divided into laminar and turbulent flow.

In order to understand the phenomenon of GHE performance heat transfer performance, thermal performance is investigated in the first 60 minutes of GHE laminar flow operation. Figure 6.10 shows the distribution along the GHE test section at two times, i.e., the first 10 minutes and the first 60 minutes. Figure 6.10 shows a decrease in wall temperature and bulk temperature along the pipe. The temperature of both bulk and wall temperature reaches the lowest value length at x/L = 1. In the first 10 minutes, the bulk temperature and wall temperature showed significant differences along with the increase in pipe length. Temperature difference wall and bulk are $\Delta \boldsymbol{T_{plain}}$ and $\Delta \boldsymbol{T_{ribs}}$ for plain and ribs coil, respectively. Generally, $\Delta \boldsymbol{T_{plain}}$ is always greater than $\Delta \boldsymbol{T_{ribs}}$. For example ,during the first 10 minutes of operation, at x/L = 0.5, $\Delta \boldsymbol{T_{plain}}$ = 0.55 ºC and $\Delta \boldsymbol{T_{ribs}}$ = 0.48 ºC.

Meanwhile, in the first 60 minutes, all temperatures experienced an increase. While the bulk temperatures of the two coils overlap each other. During this period of operation, at x/L = 0.5, ΔT_{plain} = 0.42 ºC and ΔT_{ribs} = 0.38 ºC. This phenomenon shows that ribs coil can make absorb higher heat than plain coil. The temperature difference can drive on the heat flux of plain coil and ribs coil. Because of the temperature difference between the wall and the bulk is minimal, this phenomenon causes a decrease in heat flux.

In Figure 6.11, The scattered graph illustrates information on the heat flux performance on case 1 and case 2 in the first 60 minutes of GHE operations. The performance divided into two categories time operation 10 minutes and 60 minutes operations. Overall, plain coil has greater heat flux than ribs coil. However, all groups showed a gradual decrease in heat transfer along the length of the coil. To be specific, a

larger heat flux of coil happens at the beginning of both coils lengths.The highest heat flux is achieved by plain coil about 1229 W/m^2 and 845 W/m^2 in 10 minutes and 60 minutes, respectively. In the straight pipe in the inlet area, the hydrodynamics boundary layer has been fully developed at cross-section x/L = 0.15 but the thermal boundary layer has not fully developed yet. This thermal character is because the closer to the coil area, there is a significant temperature. The temperature difference is triggered by strong temperature interference at the coil intersection. Then, on the coil side, the value of the heat flux is almost constant from the location x/L = 0.15 to x/L = 0.84. Based on findings on bulk and wall temperature, we can understand why plain coil has higher heat flux than that of ribs coil. The ribs coil absorb heat faster than plain coil hence heat flux of ribs coil slightly drop.

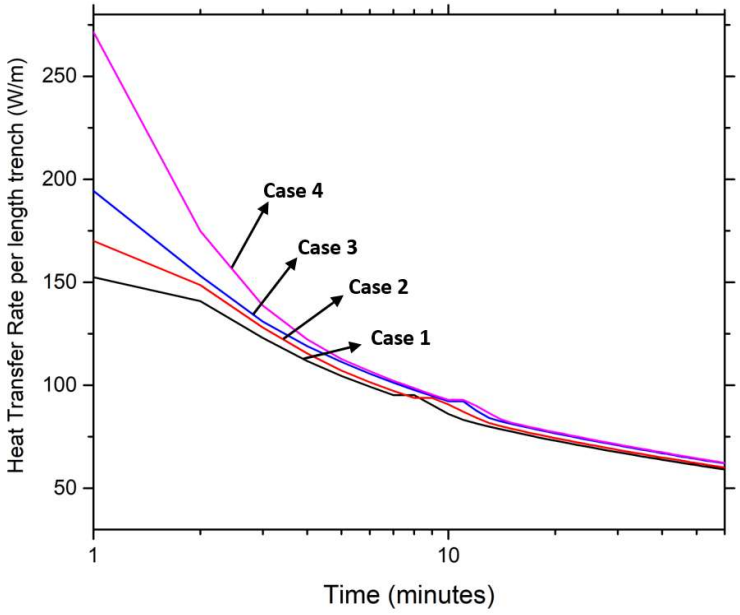

Figure 6.9. Heat transfer rate in the first 60 minutes of GHE operation

In laminar flow, the entrance length of the coil tube is shorter than the straight tube. Furthermore, the phenomenon occurs because the temperature around the coil area does not experience thermal interference from other parts of the GHE. In this section, the average value of the plain coil and rib coil heat flux are 588 W/m^2 and 530 W/m^2 in the first 10 minutes of operation, respectively. Whereas in the first 60 minutes of operation, the average heat flux of plain coil and ribs coil was 386 W/m^2 and 350 W/m^2, respectively. From x/L = 0.84 to the outlet, a sudden decrease in heat flux occurs again. This change occurs because the further away from the coil, the thermal interference of the coil is getting small.

In figure 6.12, the graph compares the heat transfer coefficient performance of ribs coil and plain coil for the laminar regime in 10 minutes and 60 minutes operation. These parameters are calculated based on previous bulk temperature, wall temperature, and heat flux, which are described earlier. The heat transfer coefficient trend has similarities to the heat flux trend. What is likely to happen is the dominance of the heat flux as a parameter to calculate the heat transfer coefficient. At the inlet cross-section, the plain coil has a heat transfer coefficient that is higher than the ribs coil. This phenomenon occurs because the wall temperature of plain coil is closer to the bulk temperature than that of the ribs coil. At x/L = 0.15, the heat transfer coefficient obtains a big discrepancy due to the developing flow region. In the coil area, the average heat transfer coefficient for plain coil and ribs coil is 1022 W/m^2.K and 1133 W/m^2.K for 10 minutes of operation. Meanwhile, the average heat transfer coefficient for plain coil and ribs coil is 892 W/m^2.K and 958 W/m^2.K for 60 minutes of operation, respectively.

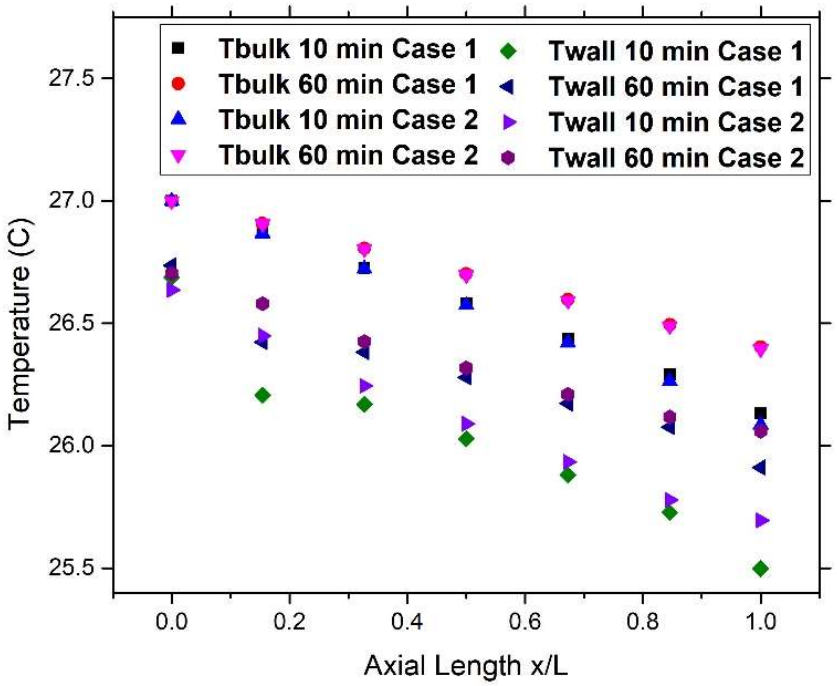

Figure 6.10. Bulk and Wall Temperature of first 60-minute operation GHE in Case 1 and Case 2

GHE performance in the first 60 minutes of turbulent flow operation is important to know the character of heat transfer rate. Figure 6.13 illustrates variations along the GHE test section in the first 10 minutes and 60 minutes of operation. The graph shows the decrease in wall temperature and bulk temperature along with the coil. At x/L = 1, both temperatures experience the lowest values. Bulk temperature and wall temperature show large deviations along with increasing pipe length in the first 10 minutes. The bulk temperature of the ribs coil is lower than that of the plain coil. Similar to laminar regime, Mostly ΔT_{plain} is also higher than ΔT_{ribs} . For example at x/L = 0.5, ΔT_{plain}= 0.40 °C and ΔT_{ribs} = 0.36 °C in first 10 minute operation. Then, in the first 60 minute operation, at the same location, ΔT_{plain}= 0.32 °C and ΔT_{ribs} = 0.29 °C. The ΔT_{plain} and ΔT_{ribs} of laminar flow is more significant than that of turbulent flow. The turbulent flow make cooling process faster than laminar flow in the fluid. The consequence is heated more accumulated in the ground then the cooling is insignificant.

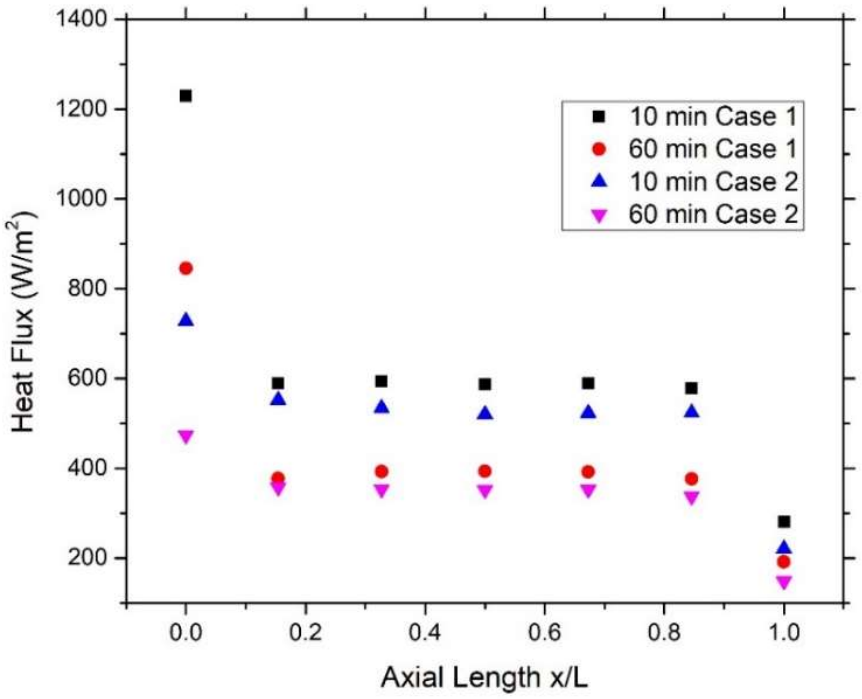

Figure 6.11. Heat Flux of first 60-minute operation GHE in Case 1 and Case 2

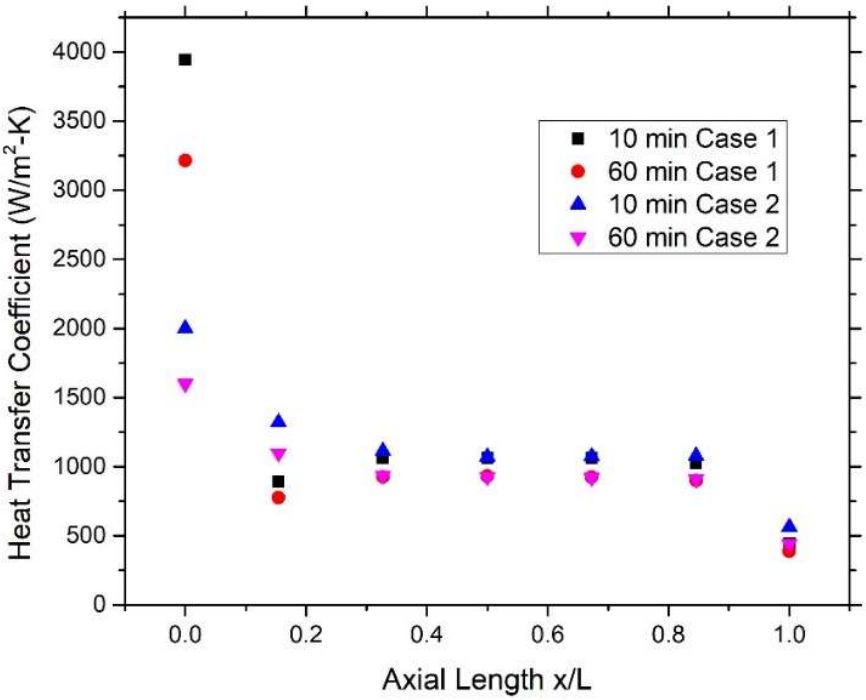

Figure 6.12. Heat Transfer Coefficient of first 60 minute operation GHE in Case 1 and Case 2

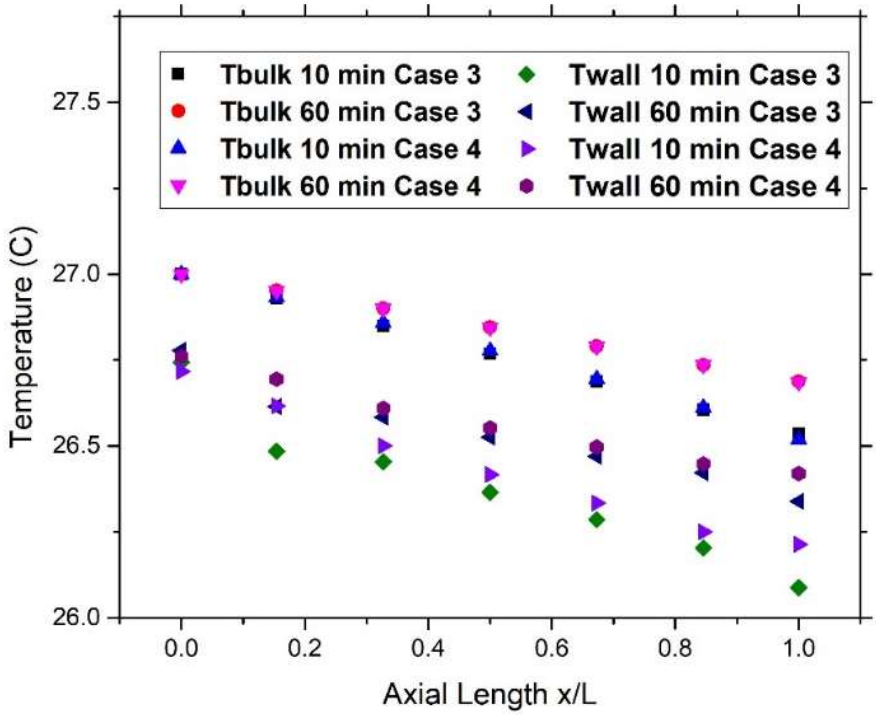

Figure 6.13. Bulk and Wall Temperature of first 60-minute operation GHE in Case 3 and Case 4

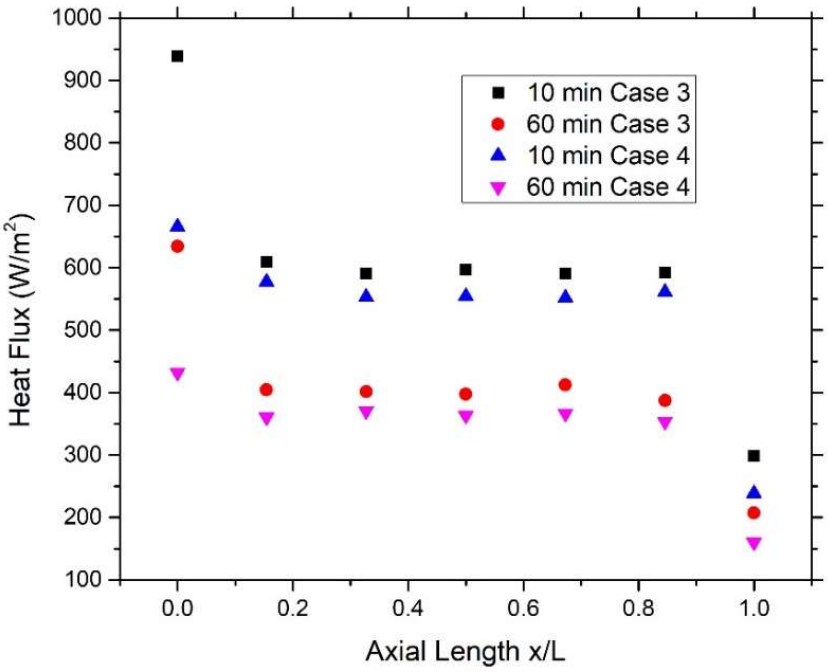

Figure 6.14. Heat Flux of first 60-minute operation GHE in Case 3 and Case 4

Figure 6.14 shows the performance of the heat flux in case 3 and case 4 in the first 60 minutes of operation. In this period, the analysis is only done in the 10th minute and 60th minute of the operation. Generally, the plain coil heat flux is greater than that of the ribs coil at 10 minutes and 60 minutes operation. However, the heat flux of the two coil continues to decrease as it approaches the downstream area. In detailed observations, high heat flux occurs at the GHE inlet side. The highest value obtained was plain coil about 939 W/m^2 and 666 W/m^2 at 10th minute and 60th minute operations, respectively. At the straight pipe entrance, the hydrodynamics boundary layer has been fully developed, but when it reaches cross-section x/L = 0.15 the thermal boundary layer is not fully developed. This event is due to approaching the coil there is a significant change in temperature. The strong temperature interference causes this at the intersection of fluid in and out of the coil. Furthermore, heat flux does not change significantly from x/L = 0.15 to x/L = 0.84. After x/L = 0.84 to the outlet, a sudden drop in heat flux occurs. This phenomenon is because the farther from the coil then the thermal interference from the coil is small. The findings on ΔTplain and ΔTribs support why heat flux of plain coil is higher than ribs coil.

In Figure 6.15, the graph shows a comparison of the performance of the heat transfer coefficient on laminar flow for 10 minutes and 60 minutes of operation. Heat

transfer coefficient is calculated based on the heat flux, wall temperature and bulk temperature previously described. The trend of the heat transfer coefficient graph is similar to the trend of the heat flux. This is caused by the dominance of the influence of the heat flux rather than that of temperatures. In the inlet section, the plain coil has a heat transfer coefficient that is greater than that of ribs coil. This happens because the wall temperature is closer to the bulk temperature than that of ribs coil. At x/L = 0.15 the coefficient has a considerable deviation due to the developing flow region. In the coil area, the average heat transfer coefficient is 1459 W/m^2.K and 1598 W/m^2.K for plain coil and ribs coil, respectively. Then, the average heat transfer rate coefficient on the coil side for 60 minutes operation is 1247 W/m^2.K and 1281 W/m^2.K, for plain coil and ribs coil, respectively.

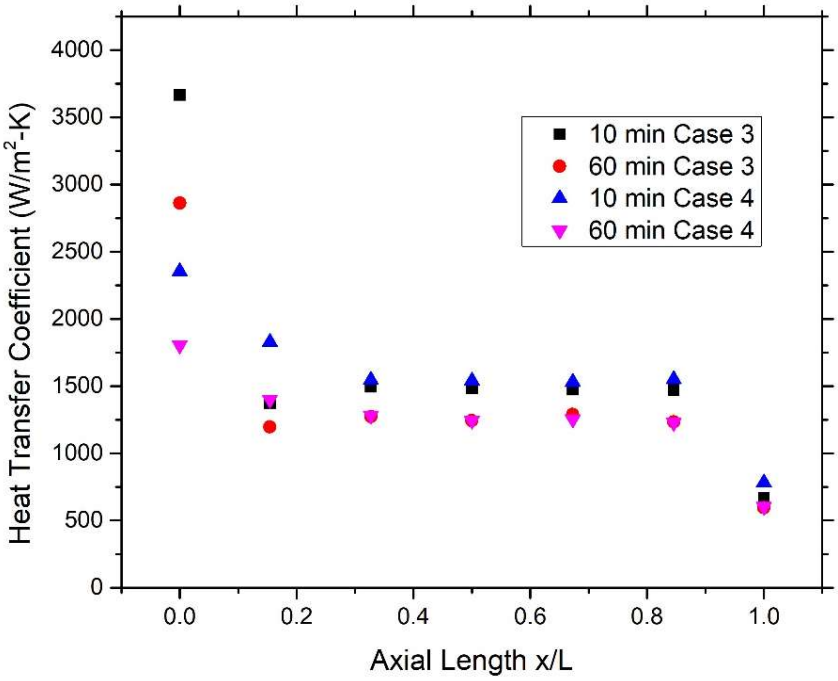

Figure 6.15. Heat Transfer Coefficient of first 60-minute operation GHE in Case 3 and 4

6.3.6 Discontinuous 120 minutes operations

In this section, the investigation is focused on heat transfer in case 2 and 5. In a 120 minute discontinuous operation, GHE is simulated in a cooling mode for 120 minutes and followed by 120 hours of non-operation or an off period where the water flow rate is completely shut down. The heat transfer rate of this intermittent condition is

carried out in the laminar flow regime and compared with the continuous operation, as shown in Figure 6.16. The heat transfer rate value is high at the start of operation and decrease due to the effect of heat accumulation in the ground during operation.

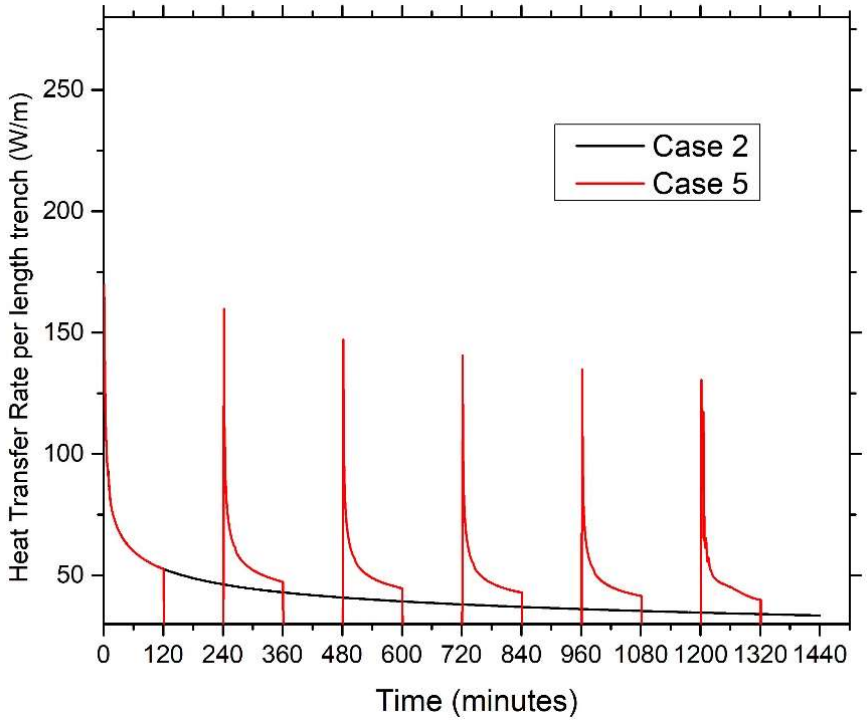

Figure 6.16. Comparison of Heat transfer rate between Case 2 and Case 5

Table 6.5 summarizes the heat transfer rate during continuous and intermittent operations. At the end of the 1320 minute operating time, the intermittent heat transfer rate is 17.3 % higher than that of continuous operation. The off period reduces the impact of heat accumulation in injected heat to ground, thereby increasing the heat transfer rate in the next flow cycle. Therefore, the ground is allowed to obtain thermal recovery during this period.

Table 6.5. Summary of the heat exchange rate in Case 2 and Case 5 in cooling mode

	Heat exchange rate per length trench (W/m)					
Operation time (minutes)	**120**	**360**	**600**	**840**	**1080**	**1320**
Continuous	52.7	43.0	39.3	37.0	35.3	34.1
Discontinuous 120 min	52.7	47.4	44.7	42.9	41.6	40.0

6.3.7 Effect of Plain and Ribs coil on Ground around GHE

Figure 6.17 shows an example of isothermal generated at the 360th and 1440th minute operations of case 2. The heat flow near GHE does not affect far-field and bottom boundaries. Ground temperatures affected by GHE are near from the edge of the pipe.

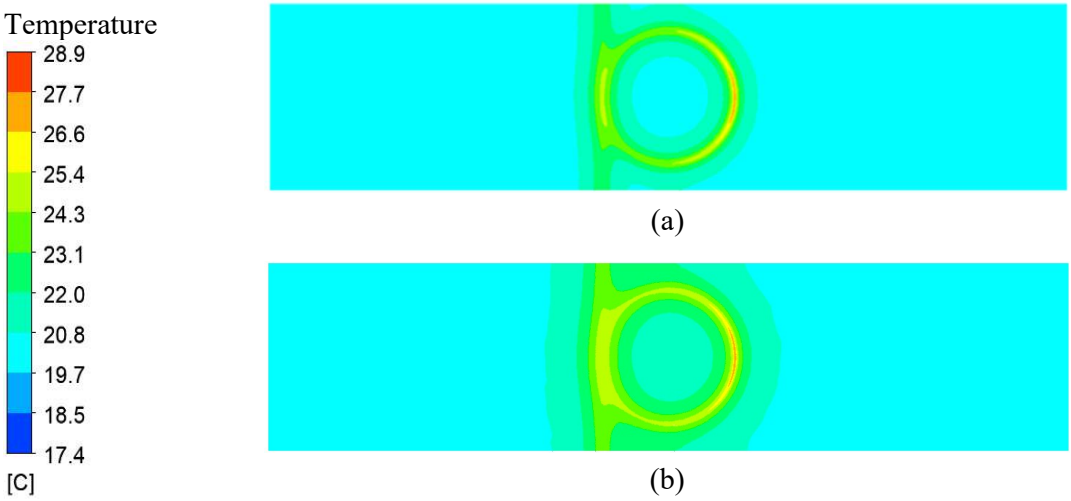

Figure 6.17. Example of Case 2 isotherm generated (ZX plane at y = -1.5 m) (a) 360th minute operation; (b) 1440th minute operation

Figure 18 shows the temperature at a location in various elapsed times. The monitoring point (m) is around 20 mm near the pipe insulator at depth 1.5 m from the ground surface. The initial temperature at this point is 20.6 ºC. In the first 120 minutes of operation, temperature rises dramatically about 2.5 ºC on all coils in both laminar and turbulent. Temperature values between variations are almost similar to each other. Large heat discharges from GHE to the ground affect increment of temperature in this short time range. Then, temperature increases steadily with about 1.7 ºC from 120 minutes until the end of operation, and the temperature difference was seen in each variation in this remaining time of operation. In turbulent flow, the temperature of ribs coil and plain coil coincides with each other and the highest value compared to other variations. This phenomenon confirms that in turbulent flow, both the ribs coil and plain coil heat transfer rates have the highest values compared to other variations. This heat transfer rates coincide with each other. On laminar flow, coil ribs show a slightly about 0.03 ºC higher temperature than that of the plain coil. This finding also proves that the heat transfer rate of the ribs coil is slightly higher than that of the plain coil. However, these findings also prove that ribs coil is only superior at laminar flow. The superiority

of the ribs coil slowly decreases compared to the plain coil if the operation is continued. The ground is unable to carry out heat recovery properly. Therefore, the thermal recovery effect in ground could be analysed for intermittent operations.

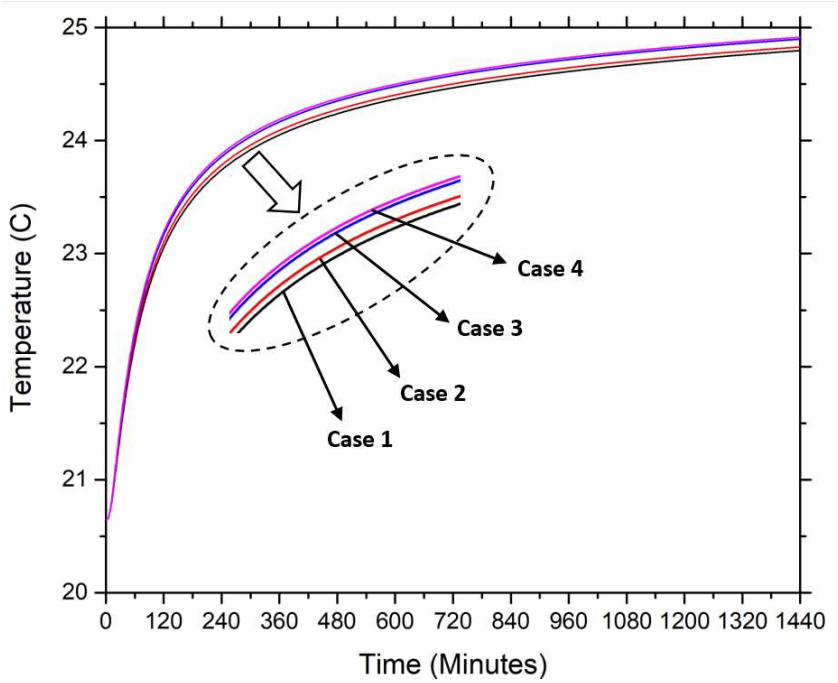

Figure 6.18. Transient Ground Temperature variation on Case 1, 2, 3, and 4 at a monitoring point m depth 1.5 m from ground surface.

Figure 19 shows the comparison between the transient ground temperature at point m on ribs coil under continuous operating conditions and intermittent 120 minutes operations. Intermittent operation graph shows low ground temperature. The accumulated heat during GHE operation could decrease in the off period. This phenomenon shows that the ground has enough time to obtain thermal recovery. The maximum and minimum temperature swing is 1.5 ºC and 0.9 ºC, respectively. Even so, the amplitude of the temperature swing decreases with increasing time. Thus, the use of intermittent methods could be ineffective in long-time operations.

6.3.8 Effect of Different Material on Plain and Ribs coil Performance

The effect of the pipe material on the performance of the heat transfer rate in laminar flow is compared and investigated, as shown in Figure 6.20. In the initial period of operation, the performance of each ribs coil with copper, composite, and HDPE material was 224 W/m, 170 W/m, and 132 W/m, respectively. Soon after, the heat transfer rate drops very quickly. This may be due to the low-temperature gradient in the

copper coil wall, which is the opposite of the temperature gradient in the HDPE coil wall.

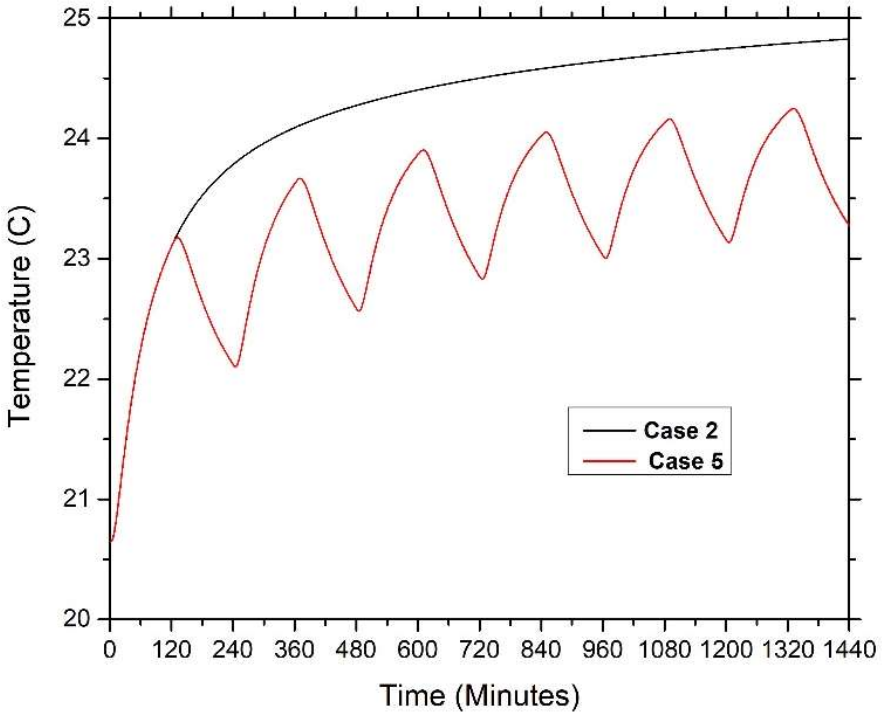

Figure 6.19. Comparison of transient ground temperature in case 2 and 5 at monitoring point m.

After 60 minutes of operation, the heat transfer rate decreases gradually due to the influence of heat accumulation widespread in the ground. In ribs coil, the average heat transfer rate of copper, composite, and HDPE are 86 W/m, 76 W/m, and 69 W/m, respectively. However, ribs and coil on the same type of material do not show significant differences in performance. In the operating time range, the increase in average heat transfer from ribs to plain coil for Copper, Composite, and HDPE material is 0.36 W/m, 0.29W/m, and 0.03 W/m, respectively. The use of materials that have higher heat conductivity has a decent prospect with the addition of a protective layer on the outside of the pipe. This analysis, according to higher conductivity material, shows a higher heat transfer rate. Even so, the performance of the heat transfer rate remains limited by the conductivity of the ground.

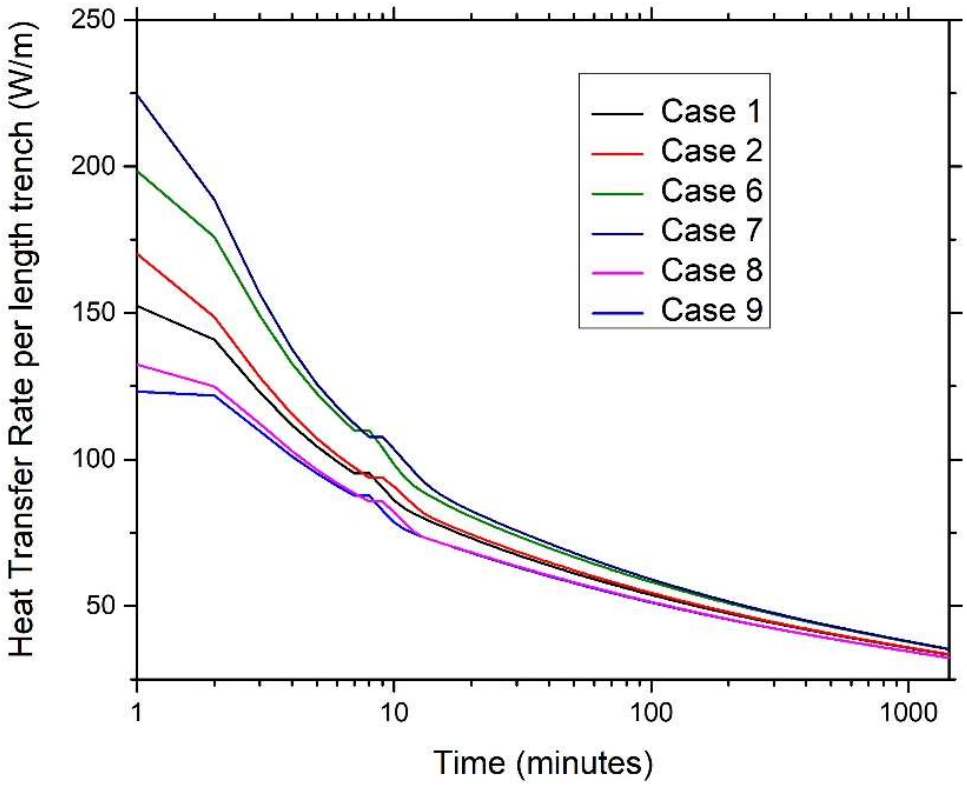

Figure 6.20. The effect of different pipe material on the heat exchange rate in case 1, 2, 6, 7, 8, and 9.

6.3.9 Effect of Different Ground Conductivity on Plain and Ribs coil Performance

Figure 6.21 shows the effect of different ground thermal conductivity sand, clay, and sandy clay on the GHE performance. Based on this figure, the heat transfer rate significantly increases with increasing ground thermal conductivity. In general, DDIR-coil has a trend of heat transfer rate that is greater than Plain-coil at the beginning of operation. On the first operation time, DDIR-coil on sandy clay has a heat transfer of 196 W/m, which is the highest compared to DDIR-coil on clay of 123 W/m and DDIR-coil on sand of 112 W/m. Thermal conductivity of clay and sandy clay is approximately 300 times and 600 times that of sand thermal conductivity, respectively. This conductivity causes the average heat transfer rate to increase by 357 times for sandy clay and 227 times for clay compared to sand on DDIR-coil. On the other hand, it can be seen that the use of DDIR-coil does not show a significant effect compared to plain-coil. This phenomenon prove that the thermal conductivity of the soil is more dominant than convection inside GHE.

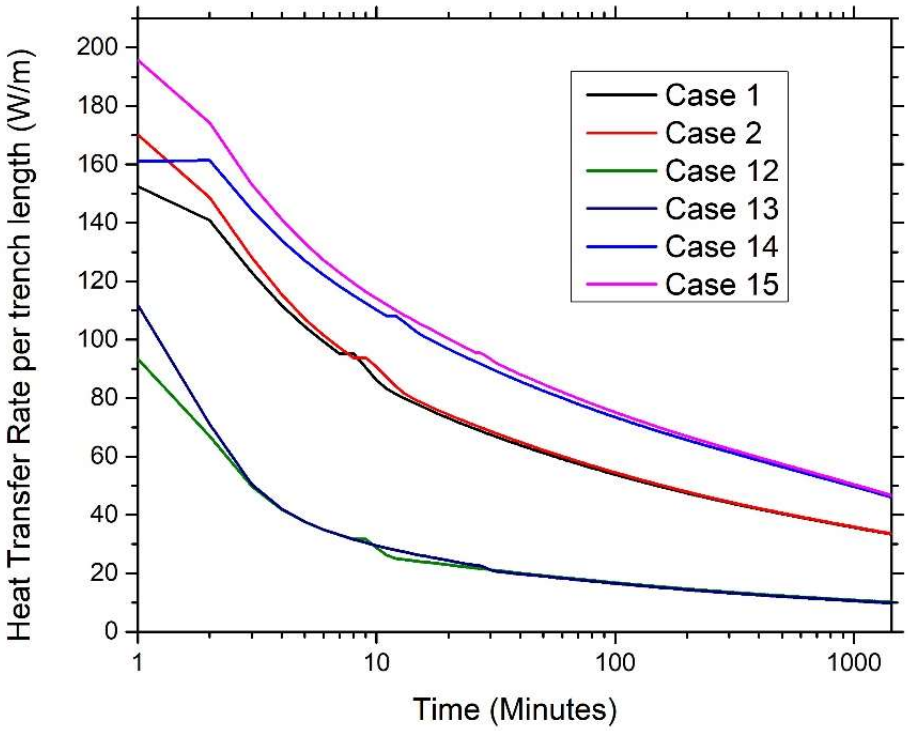

Figure 6.21. The effect of different ground thermal conductivity in case 1, 2, 12, 13, 14, and 15.

6.4 Conclusion

This study presents the results of numerical simulations of heat extraction from 2 types of horizontal slinky coil, namely ribs coil and plain coil in a laminar and turbulent flow. The simulation results show that turbulent ribs coil flow has better thermal performance than plain coil in the first 149 minutes. After this time frame, plain coil performance is superior to the end of operating time. On the other hand, in laminar flow, the ribs coil has a higher thermal performance than plain coil throughout the operating period. To find out this phenomenon, we examine 60 minutes of operation of the two coils at several pipe locations. Based on this study, we found that the laminar flow the average heat transfer coefficient for plain coil and ribs coil is 892 $W/m^2.K$ and 958 $W/m^2.K$ for 60 minutes of operation, respectively. Whereas in turbulent flow, the average heat transfer coefficient is 1459 $W/m^2.K$ and 1598 $W/m^2.K$ for plain coil and ribs coil, respectively. COP Improvement factors of plain coil and DDIR-coil in laminar flow are 1.96 and 1.98, respectively. However, COP Improvement Factor on plain coil and DDIR-coil in turbulent flow are 1.89 and 1.88, respectively. In addition to continuous operation, the 120-minute intermittent operation is also performed on laminar flow. Ribs coil operated in intermittent conditions has a thermal performance of

17.3% higher than that of continuous operation. Besides, intermittent operations can make the ground obtain better thermal recovery than continuous operations. The maximum and minimum temperature swing is 1.5 ^{o}C and 0.9 ^{o}C, respectively. The difference in material types results in significant thermal performance. In ribs coil, copper produces heat transfer rates higher 10 and 17 W/m than that of composite and HDPE, respectively, in the first 60 minutes of operation. However, the average heat transfer rate during 1440 minutes of operation; all three materials have almost the same performance. In addition, ribs and plain coil have thermal performance that coincides with each other on the same type of pipe material. Sand, Sandy clay and clay are examined to see the influence of its thermal conductivity on the GHE performance. It is found that ground conductivity is more powerful than convection DDIR-coil regarding heat transfer rate of GHE.

6.5 References

Ali, M. H., Kariya, K., & Miyara, A. (2017). Performance analysis of slinky horizontal ground heat exchangers for a ground source heat pump system. *Resources*, *6*(4), 1–18. https://doi.org/10.3390/resources6040056

Alkaff, S. A., Sim, S. C., & Ervina Efzan, M. N. (2016). A review of underground building towards thermal energy efficiency and sustainable development. *Renewable and Sustainable Energy Reviews*, *60*, 692–713. https://doi.org/10.1016/j.rser.2015.12.085

ANSYSAcademicResearch. (2017). *Help System-Fluent Theory Guide, ANSYS*.

Ariwibowo, T. H., Kariya, K., & Miyara, A. (2020). Thermal and Flow Characteristics of Discrete Double Inclined Ribs at Low Curvature Coil for GSHP Application. *EPI International Journal of Engineering*. (accepted)

Ariwibowo, T H, Kuriyama, G., Kariya, K., & Miyara, A. (2019a). Numerical Analysis of Thermo-Hydraulic Performance of Double Discrete Inclined Ribs on Curvature Coil in Laminar Flow for Ground Source Heat Pump System Application. *15th Asia Pasific Conference on Built Environment*, 7. Kaohsiung: ASHRAE REgion XIII.

Ariwibowo, Teguh Hady, Miyara, A., & Kariya, K. (2019b). Consideration of Double Discrete Inclined Ribs in Low Curvature Coil for GSHP System. *International Journal of Sustainable and Green Energy*, *8*(3), 56–64.

https://doi.org/10.11648/j.ijrse.20190803.12

Badescu, V. (2007). Economic aspects of using ground thermal energy for passive house heating. *Renewable Energy*, *32*(6), 895–903. https://doi.org/10.1016/j.renene.2006.04.006

Bharadwaj, P., Khondge, A. D., & Date, A. W. (2009). Heat transfer and pressure drop in a spirally grooved tube with twisted tape insert. *International Journal of Heat and Mass Transfer*, *52*(7–8), 1938–1944. https://doi.org/10.1016/j.ijheatmasstransfer.2008.08.038

Cavazza, L. (1981). *Fisica del terreno agrario*. UTET.

Chong, C. S. A., Gan, G., Verhoef, A., Garcia, R. G., & Vidale, P. L. (2013). Simulation of thermal performance of horizontal slinky-loop heat exchangers for ground source heat pumps. *Applied Energy*, *104*, 603–610. https://doi.org/10.1016/j.apenergy.2012.11.069

D. Kirkham, W. L. P. (1972). *Advanced Soil Physics*. New York: J. Wiley-Interscience.

D.Dayton. (2011). *TWISTED CONDUIT FOR GEOTHERMAL HEATING AND COOLING SYSTEMS*. USA: United States Patent.

Esen, H., Inalli, M., & Esen, M. (2006). Technoeconomic appraisal of a ground source heat pump system for a heating season in eastern Turkey. *Energy Conversion and Management*, *47*(9–10), 1281–1297. https://doi.org/10.1016/j.enconman.2005.06.024

Esen, H., Inalli, M., & Esen, M. (2007). Numerical and experimental analysis of a horizontal ground-coupled heat pump system. *Building and Environment*, *42*(3), 1126–1134. https://doi.org/10.1016/j.buildenv.2005.11.027

Esen, H., Inalli, M., Esen, M., & Pihtili, K. (2007). Energy and exergy analysis of a ground-coupled heat pump system with two horizontal ground heat exchangers. *Building and Environment*, *42*(10), 3606–3615. https://doi.org/10.1016/j.buildenv.2006.10.014

F. Trieb, C. Schillings, M. O'sullivan, T. Pregger, C. H..K. (2009). Global potential of concentrating solar power. *Proceedings of the 15th SolarPACES Conference*, 15–18. Berlin.

Fay, J. A., & Golomb Cambridge, MA (United States)], D. S. [Massachusetts I. of T. (2002). *Energy and the environment*. Retrieved from https://www.osti.gov/servlets/purl/20727641

Florides, G., & Kalogirou, S. (2007). Ground heat exchangers-A review of systems,

models and applications. *Renewable Energy*, *32*(15), 2461–2478. https://doi.org/10.1016/j.renene.2006.12.014

G.J. Herbert, S. Iniyan, E. Sreevalsan, S. R. (2007). A review of wind energy technologies. *Renew. Sustain. Energy Rev*, *11*, 1117–1145.

Genchi, Y., Kikegawa, Y., & Inaba, A. (2002). CO2 payback-time assessment of a regional-scale heating and cooling system using a ground source heat-pump in a high energy-consumption area in Tokyo. *Applied Energy*, *71*(3), 147–160. https://doi.org/10.1016/S0306-2619(02)00010-7

Guney, M. S. (2005). *European energy policy and renewable energies and application possibility in Turkey*. Danube Krems University in Austria.

Han, H., He, Y. L., Li, Y. S., Wang, Y., & Wu, M. (2013). A numerical study on compact enhanced fin-and-tube heat exchangers with oval and circular tube configurations. *International Journal of Heat and Mass Transfer*, *65*, 686–695. https://doi.org/10.1016/j.ijheatmasstransfer.2013.06.049

Holm´en, V. (2012). Methods for Vortex Identification. https://doi.org/10.1016/s0166-218x(03)00180-x

Inalli, M., & Esen, H. (2004). Experimental thermal performance evaluation of a horizontal ground-source heat pump system. *Applied Thermal Engineering*, *24*(14–15), 2219–2232. https://doi.org/10.1016/j.applthermaleng.2004.01.005

Islam, M. A., & Miyara, A. (2007). Liquid film and droplet flow behaviour and heat transfer characteristics of herringbone microfin tubes. *International Journal of Refrigeration*, *30*(8), 1408–1416. https://doi.org/10.1016/j.ijrefrig.2007.03.009

Islamoglu, Y., & Parmaksizoglu, C. (2003). The effect of channel height on the enhanced heat transfer characteristics in a corrugated heat exchanger channel. *Applied Thermal Engineering*, *23*(8), 979–987. https://doi.org/10.1016/S1359-4311(03)00029-2

Ito, H. (1959). Friction factor for turbulent flow in curved tube. *Journal Basic Engineering*, *81*, 123–134.

JSME Data Book: Heat Transfer (5th ed.). (2009). Sapporo: the Japan Society of Mechanical Engineers.

Kuriyama, G., Ariwibowo, T. H., Kariya, K., & Miyara, A. (2019). Heat Transfer and Presser Drop Characteristics of Curved Tube with Discrete Ribs for Ground Source Heat Exchanger. *The 2019 Annual Conference of the Japan Society of Refrigerating and Air Conditioning Engineers*, 9–14. Tokyo: JSRAE.

Li, X. wei, Meng, J. an, & Guo, Z. yuan. (2009). Turbulent flow and heat transfer in discrete double inclined ribs tube. *International Journal of Heat and Mass Transfer*, *52*(3–4), 962–970. https://doi.org/10.1016/j.ijheatmasstransfer.2008.07.027

Li, X. wei, Yan, H., Meng, J. an, & Li, Z. xin. (2007). Visualization of longitudinal vortex flow in an enhanced heat transfer tube. *Experimental Thermal and Fluid Science*, *31*(6), 601–608. https://doi.org/10.1016/j.expthermflusci.2006.06.007

Masao, F., Yu, S., & Goro, Y. (1988). Heat transfer and pressure drop of perforated surface heat exchanger with passage enlargement and contraction. *International Journal of Heat and Mass Transfer*, *31*(1), 135–142. https://doi.org/10.1016/0017-9310(88)90230-X

Mashalah Khamehchiyan, & Yushiro Iwao. (1994). Geotecnical Properties of Ariake Clay in Saga Plain-Japan. *Journal of Geotechnical Engineering*, (505), 11–18.

Masuji Sakaya, Narashino; Tsuneaki Motai, Yachiyo; Masataka Mochizuki, N. K. M. (1980). *CORRUGATED HEAT PIPE*. USA.

Meng, J. A., Liang, X. G., & Li, Z. X. (2005). Field synergy optimization and enhanced heat transfer by multi-longitudinal vortexes flow in tube. *International Journal of Heat and Mass Transfer*, *48*(16), 3331–3337. https://doi.org/10.1016/j.ijheatmasstransfer.2005.02.035

Metz, P. D. (1983). Ground-Coupled Heat Pump System Experimental Results. In *ASHRAE Transactions* (Vol. 89). Upton.

Piechowski, M. (1998). Heat and mass transfer model of a ground heat exchanger: validation and sensitivity analysis. *International Journal of Energy Research*, *22*, 965–979.

Piechowski, M. (1999). Heat and mass transfer model of a ground heat exchanger: theoretical development. *International Journal of Energy Research*, *23*, 571–588.

Pollack, H.N., Hurter, S.J. and Johnson, J. R. (1993). Heat flow from the earth's interior: Analysis of the global data set. *Reviews of Geophysics*, *31*(3), 267–280.

Saboori, B., Sulaiman, J., & Mohd, S. (2012). Economic growth and CO 2 emissions in Malaysia: A cointegration analysis of the Environmental Kuznets Curve. *Energy Policy*, *51*, 184–191. https://doi.org/10.1016/j.enpol.2012.08.065

Saeidi, R., Noorollahi, Y., & Esfahanian, V. (2018). Numerical simulation of a novel spiral type ground heat exchanger for enhancing heat transfer performance of geothermal heat pump. *Energy Conversion and Management*, *168*(May), 296–307.

https://doi.org/10.1016/j.enconman.2018.05.015

Santamouris, M., Mihalakakou, G., Argiriou, A., & Asimakopoulos, D. N. (1995). On the performance of buildings coupled with earth to air heat exchangers. *Solar Energy*, *54*(6), 375–380. https://doi.org/10.1016/0038-092X(95)00016.K

Selamat, S., Miyara, A., & Kariya, K. (2015). Analysis of short time period of operation of horizontal ground heat exchangers. *Resources*, *4*(3), 507–523. https://doi.org/10.3390/resources4030507

Takenori HINO, Sinat KOSLANANT, Katsutada ONITSUKA, T. N. (2007). *Changes in Properties of Holocene Series during Storage in Thin Wall Tube Samplers By* (Vol. 36). Saga.

Teguh Hady Ariwibowo, Akio Miyara, K. K. (2019). Thermal and hydraulic performance simulation of curved tube with discrete ribs heat exchanger for ground source heat pump system. *Proceedings of 53rd Air Conditioning and Refrigeration Union Conference*, 17–20.

Webb, R. L. (1981). Performance evaluation criteria for use of enhanced heat transfer surfaces in heat exchanger design. *International Journal of Heat and Mass Transfer*, *24*(4), 715–726. https://doi.org/10.1016/0017-9310(81)90015-6

Wu, Y., Gan, G., Verhoef, A., Vidale, P. L., & Gonzalez, R. G. (2010). Experimental measurement and numerical simulation of horizontal-coupled slinky ground source heat exchangers. *Applied Thermal Engineering*, *30*(16), 2574–2583. https://doi.org/10.1016/j.applthermaleng.2010.07.008

Yusof, A. B. (2011). *Analysis of renewable energy potential in Malaysia*. Faculty of Engineering, University of Malaya.

Zheng, N., Liu, W., Liu, Z., Liu, P., & Shan, F. (2015). A numerical study on heat transfer enhancement and the flow structure in a heat exchanger tube with discrete double inclined ribs. *Applied Thermal Engineering*, *90*, 232–241. https://doi.org/10.1016/j.applthermaleng.2015.07.009

CHAPTER

7

CONCLUSION AND RECOMMENDATIONS

7.1 CONCLUSION

This thesis presents a numerical investigation of the heating mode of horizontal slinky GHE on two different surfaces: plain coil and ribs coil. This numerical investigation highlights the comparison of thermal and fluid flow performance on the two coils. Investigation of heat transfer and pressure drop on the waterside is observed in detail in several ribs configurations in ideal and steady-state conditions. Real-scale application is also observed by comparing it to the performance of the two coils. The numerical model is validated with several experiments, so the simulation is reliable. Besides, the intermittent operation is compared to continuous operation. The impact of the intermittent operation on GHE performance and temperature on the ground around GHE is also observed. Numerical simulations are carried out using commercial ANSYS FLUENT software to determine phenomena inside and outside GHE.

Literature review on the analysis of the experimental and numerical performance of several types of GHE (Chapter 2): The results of the study are summarized as follows: Low geothermal energy (< 32 ^{o}C) is distributed in many places in the world. At below 5 m depth, the temperature fluctuation is relatively small, between 17 ^{o}C and 18 ^{o}C. Its use does not require sophisticated technology, so it is suitable as a heat source and heat sink for heating and cooling buildings. Several types of GHE have been developed, including pipe configuration, pipe surface modification, to overcome field constraints in the GHE application. Hence, utilization of GHE is a cheap and potential way to use green energy.

Based on the thermo-hydraulic analysis of turbulent flow on simulation of ribs height's effect (Chapter 3), Heat transfer and pressure drop depend on ribs height. Flow has already fully developed after at location of cross-section 90^o for all of the coils. The plain coil has a sinusoidal wall heat flux distribution. Adding axial length to the pipe makes the heat flux lower. The high and low heat flux distribution on the circumferential pipe is fluctuating. The location in Plain Coil of low and high heat flux is 10^o and 180^o, respectively. Then, the location is moved in ribs coil of 1 mm ribs height of low and high heat flux is 280^o and 350^o respectively. Strong flow generated by ribs is the reason behind this phenomenon. The good thermal mixing makes water temperature of ribs coil is hotter than that of in plain coil in turbulent regime. Higher ribs cause more significant distortion in the secondary flow than the plain coil. The character of heat transfer and pressure drop can be analyzed for correlation by looking at absolute vorticity flux. The higher ribs height increases the COP improvement factor, but increasing flowrate decreases COP Improvement factors.

Numerical studies on horizontal GHE of the same size as Chapter 3 were carried out again in laminar flow (Chapter 4), showing that the use of ribs in laminar flow was not too significant for heat transfer and pressure drop at a flow rate of 1 L/min. An increase in flow rate results in an almost linear increase in heat transfer rate and exponential pressure drop. The highest pressure drop occurred at 799 Pa/m at 1 mm ribs, which is relatively a value of about 95% higher than that of plain coil at a flow rate of 5L/min whereas the highest heat transfer rate is 873 W/m by ribs 1 mm, which is about 26% greater than that of plain at a flow rate of 5 L/min. A strange pattern occurs in COP Improvement factors. COP Improvement factors achieve the most exceptional value at a flow rate of 2 L/min in the given flowrate range. This phenomenon occurs because the COP improvement factors are based on a straight tube as the basis for the calculation. In straight tubes, there are suddenly change both heat transfer and pressure drop in the transition regime. In the range of the transition regime, the flow in the coil has produced secondary flow. So that there is a drastic increase in heat transfer, which leads to the COP Improvement factors is at a peak at 2 L/min.

From the numerical study of heat transfer and pressure drop the influence of the angle of the ribs, pitch ribs and curvature coil on the slinky-coil (chapter 5), it was found that the DDIR-coil increased heat transfer rate from 7.7 to 29.11% greater than the plain coil while the pressure drop increased from 12.7 to 89.5% higher than plain-coil. Whereas COP Improvement factors have values that vary between 0.25 and 5.29.

In terms of flow structure, multiple longitudinal vortices are not seen in downstream DDIR-coil. However, flow surrounding ribs, the longitudinal vortex is clearly visible and has almost the same as the strength of the vortex in straight ribs. The combination of secondary flow coil and flow generated by ribs merge hence strengthen fluid thermal mixing. This finding is the reason why the trajectory of water particles in the ribs coil tends to be longer than the plain coil and produces a strong turbulence flow between the fluid in the pipe wall and in the core flow, which results in increased heat transfer. The increase in the COP Improvement factor increases with the reduction in the axial distance between ribs. Ribs with an angle of 20^{o} have high COP Improvement factors. Whereas the 2.66 /m curvature coil results in a higher COP Improvement factor.

If the previous chapter (chapter 3, 4 and 5) concern the performance of the ribs coil on some geometrical modifications to the ideal and steady-state conditions, then in chapter 6, we applied the previous findings to the real-scale and transient states. In this chapter, we also observe the structure of water flow in the ribs coil. As a preliminary investigation, we divided the ribs' performance on laminar and turbulent flow. In both flow, ribs have superior thermal performance. However, in turbulent flow, the superior performance of ribs coil only lasts for the first 149 minutes of operation after that the performance of ribs coil is smaller than that of plain coil. On the other hand, thermal ribs coil performance is superior to plain coil during operating time. An analysis of the first 60 minutes of the operation is carried out to see in more detail the phenomena in the laminar and turbulent flow. Analysis of the initial 60 minutes of operation is critical because the thermal performance decline is very drastic occurred in this period. Several parameters were investigated at several coil locations. In laminar flow, the average Heat transfer coefficient on a plain coil is 892 W/m^2-K and in ribs coil is 958 W/m^2-K. In turbulent flow, the average heat transfer coefficient is 1459 W/m^2-K, and the plain coil is 1598 W/m^2-K. COP Improvement factors of plain coil and DDIR-coil in laminar flow are 1.96 and 1.98, respectively. However, COP Improvement Factor on plain coil and DDIR-coil in turbulent flow are 1.89 and 1.88, respectively. The increase in heat transfer coefficient of ribs coil in turbulent flow to turbulent flow shows that the coil absorbs heat faster at the time of operation so that the temperature of the soil around the turbulent flow coil heat faster. Next, the ribs coil in the laminar flow is investigated by comparing the continuous and 120-minute intermittent operating modes. At the end of the operation, the intermittent mode produces 17.3% higher performance than continuous operation. Also found, an intermittent mode can provide time for the soil to

make a thermal recovery. The amplitude of swing temperature is 1.5 ^{o}C, and the lowest is 0.9 ^{o}C. Ribs coil is also tested with different types of pipe material, namely copper, composite, and HDPE. In general, copper coil ribs can produce the most excellent thermal performance compared to composite and HDPE in the initial 60 minutes of operation. However, on the remaining operation time, copper coil has almost the same performance as other materials. It was also found that the use of different types of material in plain coil and ribs coil produces similar thermal performance. Considering the flow structure in the ribs coil and the plain coil, it is clear that the thermal mixing in the ribs coil is much higher than that of the plain coil. However, this increase in performance is limited by the thermal conductivity of ground. DDIR-coil and plain coil were tested on three types of soil, namely sand, sandy clay and clay with different thermal conductivity. Sandy clay, which has the highest thermal conductivity than any other soil, has the highest heat transfer rate. However, the DDIR-coil performance does not show any significant difference from plain-coil. These findings indicate that the flow phenomenon in the coil does not make a significant contribution compared to soil conductivity. Therefore, GHE performance mostly depends on the phenomenon in the ground side rather than that of waterside.

In conclusion, this thesis study provides useful information about the effect of the use of double discrete inclined ribs on GHE slinky-coil under ideal and steady-state conditions as well as real and transient conditions. Besides, this study provides an investigation into the dominance of the influence of thermal ground on GHE performance.

7.2 Recommendation for future work

Based on this research, performance improvement can be made through the following recommendations:

i. The simulation results presented in chapter 3 need to review the increase in the number turns of coils and various diameters of the coil to observe the effect of the strength of the vortex generated by the curvature coil and pitch coil.

ii. The simulation results presented in chapter 4, investigation of proper location of ribs should be investigated to see the which part of flow contribute to strengthening and destructing of vortex

iii. The simulation results in chapter 5 show simulations on heating mode. The simulation should also be done in cooling mode. Furthermore, various modification of ribs geometry is also necessary. The temperature wall should change with time to produce a thermal performance that is identical to the real conditions on the ground.

iv. The simulation results in chapter 6 show simulations on cooling mode. Simulations need to be done in heating mode as well as alternate heating and cooling. The use of ribs coil needs to be done carefully so that the soil does not quickly saturate. The dominance of the influence of the thermal conductivity of the soil is far greater than the influence of the structure of water flow in GHE. So, it is necessary to increase heat transfer on the ground using either grouting material that has high thermal conductivity. Besides, to help spread the thermal evenly, it is necessary to use fin on the ground side.